2016

Virtual Inertia Emulation to Improve Dynamic Frequency Stability of Low Inertia Microgrids

Dipesh Shrestha
South Dakota State University

VIRTUAL INERTIA EMULATION TO IMPROVE DYNAMIC FREQUENCY STABILITY OF LOW INERTIA MICROGRIDS

BY

DIPESH SHRESTHA

A thesis submitted in partial fulfillment of the requirements for the

Master of Science

Major in Electrical Engineering

South Dakota State University

2016

VIRTUAL INERTIA EMULATION TO IMPROVE DYNAMIC FREQUENCY STABILITY OF LOW INERTIA MICROGRIDS

This thesis is approved as a creditable and independent investigation by a candidate for the Master of Science in Electrical Engineering degree and is acceptable for meeting the thesis requirements for this degree. Acceptance of this thesis does not imply that the conclusions reached by the candidates are necessarily the conclusions of the major department.

Reinaldo Tonkoski, PhD
Major/Thesis Advisor Date

Steven Hietpas, PhD
Head, Electrical Engineering and Computer Science Date

Dean, Graduate School Date

ACKNOWLEDGEMENTS

I would like to express my deep gratitude to my supervisor Dr. Reinaldo Tonkoski for his guidance, support, and encouragement. He was very generous on providing his invaluable advice both in research and my career. Every discussion on research with him was very encouraging and fruitful, which always broadened my knowledge. I would also like to thank Dr. Zhen Ni and Dr. Timothy M. Hansen for agreeing to serve as my thesis committee members. I appreciate their invaluable suggestions while reviewing this thesis.

I am also thankful to South Dakota State University, Department of Electrical Engineering and Computer Science for providing me necessary resources for conducting this research. I would like to express my gratitude to all the staff and faculty members of this department for their help and encouragement.

I would like to thank my father Gyanu Shrestha, my mother Bindra Devi Shrestha, my sister Binu Shrestha and my brother-in-law Surya Adhikari for their unconditional love and support. I could not have done it without them.

Thank you to my friends Ashim Gurung and Sadhana Shrestha for encouraging and motivating me throughout this work.

Special thanks to Ujjwol Tamrakar for helping me in completing this work, Mr. Jason Sternhagen for helping me during the experimental work and Mr. Albert Dunford for solving my problems in PSIM.

Finally, I would like to express my sincere acknowledgment to all my friends and family at South Dakota State University for their company and support, which made my life at Brookings so pleasant.

CONTENTS

ABBREVIATIONS

AC	Alternating current
ADC	Analog to digital converter
ADP	Adaptive dynamic programming
AGC	Automatic generation controller
BJTs	Bipolar junction transistors
CC-VSI	Current controlled voltage source inverter
DC	Direct current
DFIG	Doubly fed induction generator
dq	Direct quadrature
DSP	Digital signal processor
ESS	Energy storage system
GSGFd	Grid supporting grid feeding
GTOs	Gate turn off thyristors
HPF	High pass filter
IC	Integrated circuit
IEEE	Institute of electrical and electronics engineers
ISO	International organization of standardization
kHz	kiloHertz
LC	Inductor capacitor
LCL	Inductor capacitor inductor

LPF	Low pass filter
MLP	Multi layer perceptron
MOSFET	Metal oxide semiconductor field effect transistors
MPPT	Maximum power point tracking
PCC	Point of common coupling
PD	Proportional derivative
PLL	Phase locked loop
PV	Photovoltaic
PWM	Pulse width modulation
rms	Root mean square
ROCOF	Rate of change of frequency
SCI	Serial communication interface
SDSU	South Dakota State University
SG	Synchronous generator
SOC	State of charge
SPWM	Sinusoidal pulse width modulation
SVM	Space vector modulation
TI	Texas Instruments
VI	Virtual inertia
VIC	Virtual inertia controller
VOC	Virtual oscillator control
VSG	Virtual synchronous generator

VSM	Virtual synchronous machine
VSYNC	Virtual synchronous generator

LIST OF FIGURES

LIST OF TABLES

ABSTRACT

VIRTUAL INERTIA EMULATION TO IMPROVE DYNAMIC FREQUENCY STABILITY OF LOW INERTIA MICROGRIDS

DIPESH SHRESTHA

2016

Due to low inertia and the intermittent nature of photovoltaic systems, dynamic frequency stability issues arise in microgrids with large photovoltaic systems. This limits the maximum amount of photovoltaic systems that can be penetrated in the microgrid. In order to increase the penetration of photovoltaic systems, the dynamic frequency controller, that is faster than the primary frequency controller (governor control) needs to be added in the microgrid system. For dynamic frequency control, inertial response can be provided from the energy storage system (such as battery, ultra-capacitor, photovoltaic system, etc.), which is termed as virtual inertia. A virtual inertia can be defined as the combination of an energy storage system, a power electronics converter and a proper control algorithm that improves the dynamic frequency stability of the microgrid. A virtual inertia supplies or absorbs the active power to and from the energy storage system to improve the dynamic frequency stability. This thesis presents the design and implementation of a hardware prototype of 1 kW virtual inertia in a microgrid with a real diesel generator and a load. For a step change in load, the virtual inertia improved the frequency response of the system from 57.39 Hz to 58.03 Hz. This improvement in frequency response proves the concept of existing proportional derivative based virtual inertia experimentally. With the addition of virtual inertia, the frequency of the system

returns to the nominal frequency slower. Once the primary controller (governor control) of the system takes the action to regulate the frequency, virtual inertia no longer needs to add inertia to the system. So the dynamics of the VI needs to be improved so that the frequency returns to nominal frequency faster. This thesis also proposes an online learning controller based virtual inertia using adaptive dynamic programming that learns online and improves the dynamics of the controller of existing VI. The output of this controller supplements the output of the existing proportional derivative controller of virtual inertia. The supplementary controller is trained to increase the dynamics of the outer controller and to bring the system frequency to nominal frequency faster. Due to faster dynamics, the net energy delivered by the VI can be reduced significantly and improve the total possible discharge cycles from the battery. For performance evaluation, the proposed controller was implemented in a microgrid with a photovoltaic system, a diesel generator and a variable load. With the proposed controller, the frequency of the system returned to nominal frequency faster. The net energy delivered by the proposed controller in a photovoltaic diesel generator microgrid was 46.14% of the net energy delivered by the existing virtual inertia. Due to the decrement in the total energy delivered, the total number of possible battery discharge cycles with ADP based VI was 2.17 times of the total number of possible battery discharge cycles from VI.

CHAPTER 1 INTRODUCTION

1.1 Background

In 2013, around 1.2 billion people ($1/6^{th}$ of humanity) in the world did not have access to electricity [1]. 80% of those live in the rural area, where the extension of the electrical grid is economically and technically infeasible. Remote microgrids can be an economical and technical solution to provide electricity in such rural areas. According to Navigant research [2], the global remote microgrids installation will increase from 349 MW in 2011 to over 1.1 GW in 2017. Diesel generators are the first choice of energy source in microgrids. However, due to the global concern about the clean energy and global adoption of distributed renewable energy systems, installation of photovoltaic (PV) systems is increasing. In 2014, with the installation of 38.7 GW of PV systems worldwide, the global total reached 177 GW [3]. PV systems can reduce cost of fossil fuel consumption in remote microgrids and reduce green house gas emmissions. However, PV systems alone cannot be a feasible option for remote microgrids due to their intermittent nature and unavailability at night. To solve this, a battery backup system can be a solution to supply energy during the night time. However, in order to have a larger number of days of autonomy, the battery sizing would be very large which would increase the cost of the microgrids. Diesel generators can be installed in such microgrids to supply the base load or act as the backup power source. Therefore, PV-diesel generator microgrids with battery backup can be an effective solution in remote microgrids.

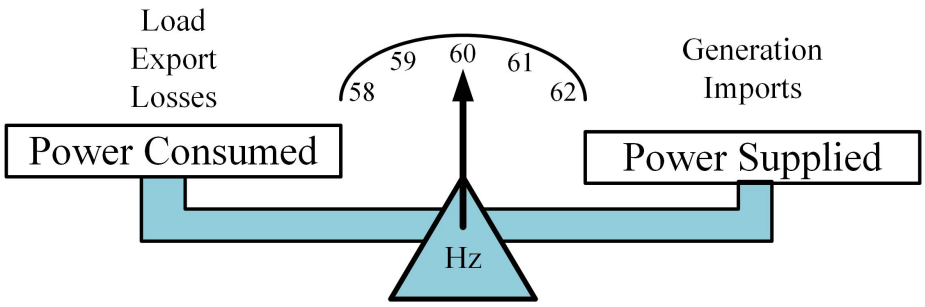

Figure 1.1. Physics of power balance in power system for constant frequency[4].

According to the physics of power balance shown in Figure 1.1, in order to maintain the frequency, there should always be the balance between the active power consumed and active power supplied by the source. Sudden change in the output power from the PV systems or in the load affect such balance. This effect in balance cause frequency deviation from nominal values. In a bulk power system, dominated by synchronous generators (SG), the rotating masses (turbine and flywheel) of the SG absorbs or releases the kinetic energy during imbalance of power generated and consumed. So rotating masses of SG act like energy storage and maintain the dynamic frequency stability of the system. Such a property of rotating masses to oppose the sudden change in frequency is known as moment of inertia (simply termed as “inertia”). Rate of change of frequency (ROCOF) is inversely proportional to inertia of the system. PV systems do not have the rotating masses like SG, which result in inertialess PV systems or relatively low inertia in PV-diesel generator microgrids. The outcome in high ROCOF is due to sudden change in load or in output power from PV systems. The primary frequency controls (governors) may not be fast enough to maintain the dynamic frequency stability. As a result, frequency relays may trip. The tripping of relays connected to the generators may cascade and lead to system instability. This limits the maximum amount of PV penetration in microgrids.

According to Gurung et al. [5], without energy storage systems (ESS), 45% of the total capacity of a PV-hydro microgrid system with system inertia of 5 s can be supplied by PV systems while keeping the frequency of the system within normal operating range of ±2% of nominal frequency. According to ISO 8528-5 [6] standard limits, the recommended frequency operation range for SG is ±2.5% of rated frequency (i.e. ±1.5 Hz for 60 Hz system) and recommended ROCOF is ±0.6 Hz/s. Manufacturers recommend to disconnect the generator if the frequency drops below 57 Hz or rises above 61.8 Hz [4]. However, these recommended values may differ according to manufacturers.

In order to improve the dynamic frequency stability, and to increase the penetration of renewable energy sources, dynamic frequency control (that operates in milliseconds) faster than the primary frequency control (that operates in seconds) of SG needs to be added. In other words, inertia can be set into the system through an energy storage system (ESS), such as a battery, an ultracapacitor, etc. Inertia added externally in such a way is termed as "virtual inertia (VI)." A VI is defined as the combination of an ESS, a power electronics converter and proper control algorithm that improves the dynamic frequency stability of the system.

1.2 Previous work

Rahmann et al. [7] operated the PV system below its maximum power point tracking (MPPT) to have some energy reserve, that can be used during transients for frequency support. During the increment in load in the system, PV system increased its power by operating near MPPT. Similarly, during the decrement in load in the system, PV system decreased its power by operating it below its current point of operation. The

frequency response of the system was improved but the efficiency of PV system was poor because it was operated below the MPPT.

Wang et al. [8] enhanced the inertial response of a PV system by using battery ESS. PV module was connected with a unidirectional DC-to-DC converter, and battery ESS was connected to a bidirectional DC-to-DC converter for the purpose of frequency control. Both of these systems were connected to the same DC bus and connected to the grid from a grid tied inverter. The grid tied inverter was controlled to mimic a SG to provide frequency support to the grid. The overall efficiency of the system was maintained since the PV system was always operating in MPPT.

Visscher et al. [9] called the concept of virtual kinetic energy storage in an inverter called virtual synchronous generator (VSYNC) by adding an extra power reference for inverter based upon the ROCOF and difference in frequency from nominal frequency of the system. The reference power generated based upon the ROCOF of the system is called inertia part. Similarly, the reference power generated based upon the difference in frequency of the system from nominal frequency is called droop or damping part. The inertia part controls the ROCOF of the system and damping or droop part brings the system frequency to normal frequency.

Zhong et al. [10] proposed to operate the inverter by mimicking the dynamic behavior of a SG called ”synchroverters.” Due to the dynamic behavior exhibited by the inverter, it damped the oscillations caused by change in load or generation in the system. A miniature hardware prototype was developed that mimicked the behavior of a SG.

Torres et al.[11] introduced the concept of the self-tuning virtual synchronous machine (VSM) in which the damping and inertia coefficients are tuned online by solving

an optimization problem. The main concept behind online tuning of those coefficients is based upon the fact that once the primary control of the system (governor) responds to the change in frequency, inertia emulation from VSM can be decreased. As a result, the net energy consumed and maximum power delivered from the inverter was reduced compared to constant parameter VSM.

Miura et al. [12] used the swing equation of a SG to calculate the mechanical phase angle ω_m and inverter output voltage, and called virtual synchronous generator (VSG). The so calculated reference mechanical phase angle ω_m and inverter output voltage from swing equation damped the oscillation in the frequency of the system.

Johnson et al. [13] introduced the concept of virtual oscillator control (VOC) for synchronization and regulating a number of islanded power electronics converters. VOC is time domain controller and emulates the dynamics of nonlinear oscillators. A system with VOC synchronizes their output AC voltage, share the load and maintain the voltage and frequency of the system within standard limits. VOC is faster than the conventional droop based control for controlling the voltage and frequency of the system. A hardware prototype of inverter with VOC was developed to verify the concept experimentally.

Abraham et. al. [14] reduced the variability of a PV system by adding battery ESS with it. The instantaneous PV power is sent to a high pass filter (HPF), and the output of the HPF filter is the reference power for the battery ESS. Thus, the battery ESS provides the high frequency part of transient power and smoothens the output power from PV system with battery ESS.

Tamrakar et al. [15] improved the dynamic frequency stability of a PV-hydro microgrid by adding virtual inertia from a ESS. The control algorithm for inertia

emulation is based upon the difference in frequency from the nominal value and the ROCOF of the system. The dynamic frequency response of the system was improved for the change in load and the change in output power from a PV system.

Guo et al. [16] improved the dynamic frequency stability of a doubly fed induction generator (DFIG). by tuning the optimal values of proportional gain (K_p) (droop part) and derivative gain (K_d) (inertia part) by solving the Bellman optimization equation [17]. It is called the virtual inertia controller (VIC) . The reference power generated from proportional derivative controller was added to the reference power generated by the MPPT controller. The optimally tuned gains improved the frequency response of the system. But the DFIG were not operated at MPPT, which decreases the efficiency of the system.

Paquette et al. [18] provided the detailed examination of the poor transient power sharing between the inverter and the SG, when the inverter is working in grid-supporting-grid-feeding (GSGFd) mode. Inverters have faster dynamic capacity with compared to SG. But inverters have limited or no overload capacity compared to SG. So when the inverter in GSGFd mode is connected to SG, the inverters tend to deliver more transient power than SG. Due to this, more transient current is drawn from ESS, which can reduce the effective life of the battery and the inverter. So the authors suggested to operate the microgrids with more frequency deviations (but within standard limits) to increase the life of the battery.

Generally, a proportional derivative (PD) controller is used in the outer control loop of a VI to calculate the VI reference power. But the literature lacks the experimental proof of concept of the PD based VI in a microgrid with a real generator and a load. In this

thesis, implementation of a hardware prototype of VI is provided along with its performance in a mircogrid with a real generator and a load. Moreover, due to the added inertia from VI, the frequency of the system returns back to the nominal frequency slower. But once the primary control system (governor) takes the action for frequency regulation, VI inertia no longer needs to regulate frequency [11]. Due to slower response time, the net energy exchanged by VI becomes larger. Every battery has a rated charge life (Ah) and it is said to have reached its effective lifetime, when the sum of effective battery Ah reaches its rated Ah [19]. As a result, the battery used for VI can reach its lifetime soon. In order to increase battery lifetime, it is proposed to make the VI adaptive that learns online and brings the system frequency to nominal frequency faster. In this thesis, an online controller using adaptive dynamic programming (ADP) is used to supplement the existing PD controller to improve the dynamics of existing VI and to improve lifetime of the battery. VI with supplementary ADP controller is termed as "ADP based VI" throughout this thesis.

1.3 Motivation

Firstly, dynamic frequency stability of low inertia microgrid needs to be improved by adding VI in the system to increase the penetration level of the PV system. Concept of VI needs to be verified experimentally in a microgrid with a real diesel generator and a load. Secondly, lifetime of the battery used for the VI should be improved by reducing its energy usage. For this, the dynamics of the VI needs to be improved by using online learning controllers that brings the system's frequency to nominal frequency faster. Due to faster dynamics, the net energy that needs to be delivered by VI may decrease and

improve the lifetime of the battery.

1.4 Objective

The first objective of this thesis is to experimentally verify the proof of concept of VI in a microgrid with a real generator and a load. The second objective is to improve the dynamics of VI by using an online learning controller that reduces the energy consumption from battery and improve its effective lifetime.

The specific tasks of this thesis were to:

1. Design a hardware prototype of VI and integrate in a microgrid with a real diesel generator and a load to improve the dynamic frequency stability.

2. Improve the dynamics of VI, by using an online controller, which brings the system frequency to nominal frequency faster.

3. Analyze the effect of proposed controller in the energy usage from the battery and in its effective lifetime.

The tasks performed will determine the improvement in the dynamic frequency stability of PV-diesel generator microgrid system using VI. Moreover, the study will determine the improvement in dynamic response of VI and reduction in net energy consumed by using adaptive VI. The study will also determine the improvement in the effective lifetime of the battery using the proposed controller.

1.5 Contributions

The major contributions of this research are as follows:

1. Developed a hardware prototype of VI and improved the dynamic frequency stability of a microgrid with a real diesel generator and a load.

2. Improved the dynamics of VI using an online controller, which brings the frequency of the system to nominal frequency faster.

3. Reduced the net energy exchanged and improved the effective lifetime of the battery from the proposed controller.

1.6 Thesis outline

This thesis has been organized as follows: Chapter 2 describes the concept of conventional VI and ADP based VI. Chapter 3 introduces the procedures to design and develop a hardware prototype of a VI and design of ADP based VI. It also describes the system benchmark used for simulation and experimental setup. Chapter 4 presents the simulation and experimental results and analysis. Finally, Chapter 5 presents the conclusions, limitations, and possible future work.

CHAPTER 2 THEORY

Chapter 2 introduces the PV-diesel generator hybrid microgrid with ESS. Dynamic frequency stability of the PV-diesel generator hybrid microgrid is also discussed. The concept of VI to improve the dynamic frequency stability of the PV-diesel generator microgrid system is presented. The concept of online control using adaptive dynamic programming controller is provided to make the VI adaptive and learn online to improve dynamics of VI. Modeling and control of three phase inverters using the rotatory dq frame controller is also included.

2.1 Photovoltaic diesel generator hybrid microgrid systems

PV-diesel generator hybrid microgrid systems consists of the diesel generator and the PV systems. ESS are also added to this microgrid to improve the reliability of the system by improving the dynamic stability and efficiency of the system. ESS provides flexibility for the utilization of the available resources in the system, which can improve the efficiency of the overall system. PV systems give power to the system during the day, which can be supplied to the load or may be stored in ESS if there is surplus of power. The diesel generator can be operated when there is deficit in power generation from PV systems or according to schedule [19].

2.1.1 Photovoltaic systems

Figure 2.1 shows the main components of a grid connected PV system. The PV module converts the light energy (irradiance) into electrical energy. Generally, the PV system consist of a generation-side-converter cascaded to a grid-side-converter. The

generation-side-converter is a DC-to-DC converter (boost converter) that steps up the DC voltage generated by PV modules to suitable DC voltage. This converter is controlled in such a way that the PV system operates in MPPT. The generation-side-converter is coupled with grid-side-converter by a coupling capacitor. Generally, a grid-side-converter is DC-to-AC converter (an inverter) that converts the input DC voltage to AC voltage following the IEEE 1547 standard limits[20]. A grid-side-converter must have anti islanding feature, according to IEEE 1547 standard. In an islanding feature, if there is any voltage or frequency disturbance in the the grid then the grid connected inverters must stop injecting power within 2 s. Moreover, when the grid side converter is connected to the grid, it must monitor the voltage and frequency of the system for 5 minutes before injecting power to it [21].

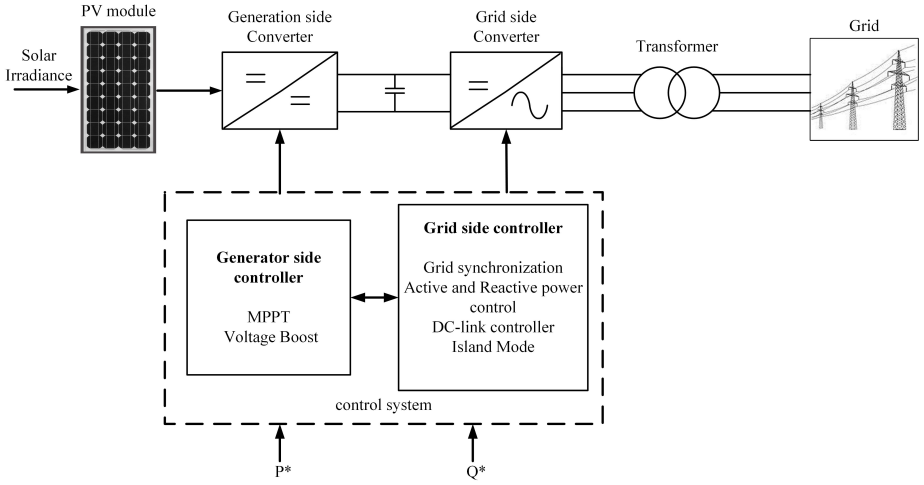

Figure 2.1. Main components of a grid connected PV system.

PV modules are made by the combination of multiple numbers of PV cells. A PV cell is a specialized semiconductor diode that converts the light into DC power. A current-voltage (IV) curve shows the different possible combinations of DC current and DC voltage from a PV cell for a particular irradiance. For an ideal case, the current from

the PV module is given by [21].

$$I = I_L - I_o[exp\frac{qV}{nkT} - 1] \tag{2.1}$$

where I_L is light generated current, I_o is saturation current, q is elementary charge i.e. 1.6×10^{-19} C, K is Boltzmann's constant i.e. 1.38×10^{-23} J/k and T is cell temperature in Kelvin.

Figure 2.2 shows the IV curve of a typical PV module at a different irradiance level. The maximum voltage for the PV module is almost the same for different irradiance. However, with increment in irradiance the maximum current from the PV module increases and vice versa.

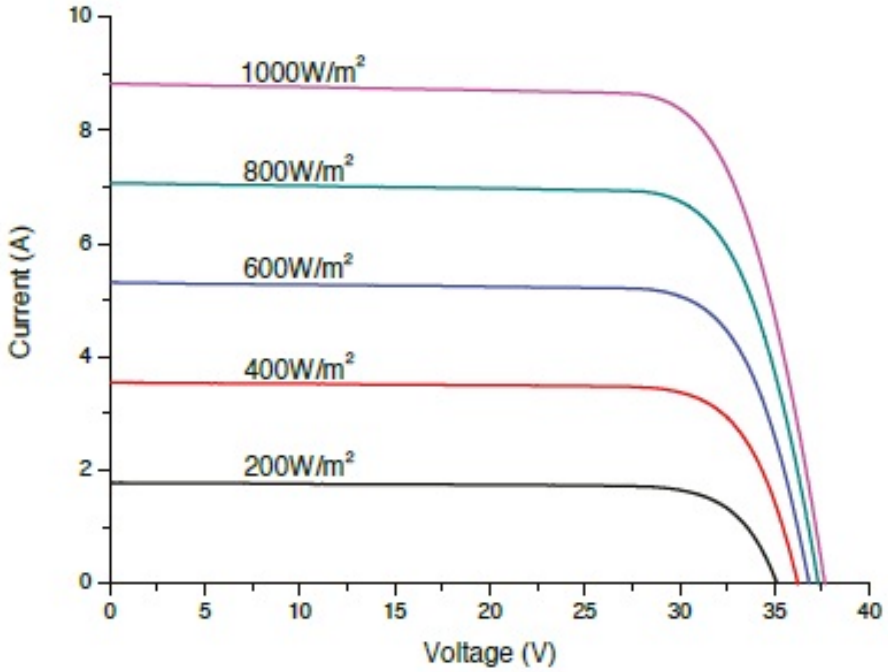

Figure 2.2. IV curve of a PV module at different irradiance level [22].

Figure 2.3 shows the IV characteristics of a typical PV cell at normal conditions.

The power delivered by a solar cell is the product of current and voltage $(I \times V)$. The point-by-point product of voltage and current at each point gives the output power from the PV cell. When the PV cell is open circuited, i.e. no load is connected to it, the current from the PV cell becomes zero and the voltage of the cell becomes maximum, becoming an open circuit voltage (V_{OC}). Similarly, when the output terminals of the cell has short circuited, the current from the cell reaches the maximum value known as the short circuit current (I_{SC}). But at neither of these points, the output power from the cell is maximum. There is only one point when the output power from the cell is maximum where the voltage and current are V_{mp} and I_{mp} respectively. This point is called "maximum power point (MPP)." A generation-side-converter of the PV system is controlled in such a way that the PV module is operated at MPP.

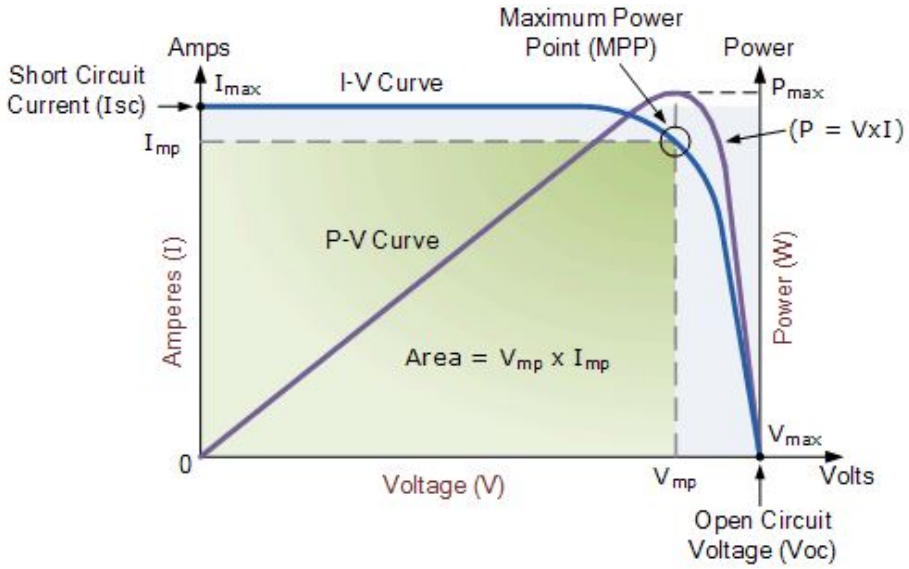

Figure 2.3. Power curve of PV module [23].

2.1.2 Diesel generator systems

A diesel generator is a device that has a combination of diesel engines and electric generators. As a result, diesel generator generates electricity and uses diesel as the fuel. Figure 2.4 shows the main components of a diesel generator. The engine is the main source that harnesses mechanical power to the generator, coupling with a generator through a shaft which transfers the mechanical power to it from the engine. Alternator is the main part of the generator that produces electricity from the mechanical power provided from the engine. A fuel system stores and provides diesel fuel to the engine. Governor controls the amount of fuel injection into the engine based upon the frequency of the system. A voltage regulator converts AC voltage to DC current and feeds it to secondary windings in stator to regulate the voltage across its terminal. A cooling system removes heat generated in the engine with proper cooling and ventilation. Battery chargers keep the generator battery charged, which is used for the start function of generator. The control panel provides user interface to monitor the generator's condition while operation and provides control schemes like electric start or shut down.

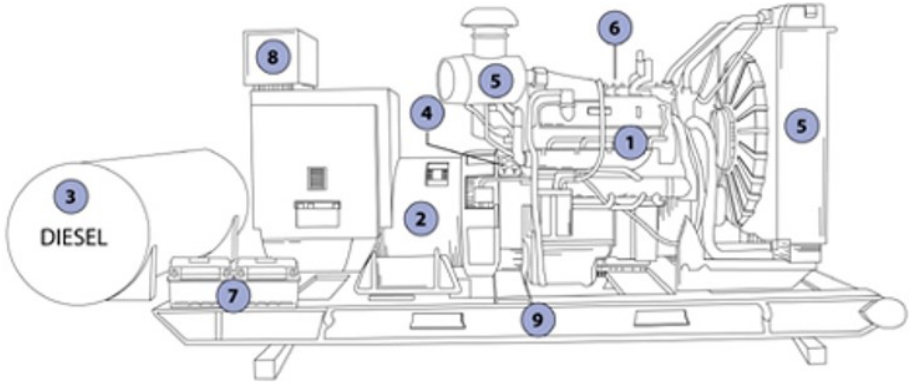

Figure 2.4. Main components of a diesel generator [24].

Figure 2.5 shows the diagram of the diesel generator with governor and excitation system. The three phase synchronous generator is the main electromechanical part that converts kinetic energy from turbine into electrical energy. Rotor and stator are the main components of a synchronous generator. The rotor of the synchronous generator is the rotating part that contains a winding called as “field winding” that generates the magnetic field required to generate voltage. DC current flowing in it generates the magnetic field. The stator of synchronous generator is the stationary part that contains a winding called as “armature winding”. According to Faraday’s law, the rotating magnetic field (rotor winding) moving relative to stationary winding (field winding) induces AC voltage across terminals of stator. The AC voltage generated across the stator’s terminal is transformed into required voltage level using transformer and distributed to the load. The governor system senses the frequency of the system and compares it with the reference frequency. Based upon this error in frequency, the governor controls the fuel valve opening to control the fuel supply. Thus the frequency of AC voltage is controlled by the governor system. Similarly, the excitation system senses the AC voltage and compares it with reference voltage. Based upon this error in voltage, the automatic voltage regulator generates the required current for field winding. Thus, the magnitude of AC voltage is regulated by excitation system.

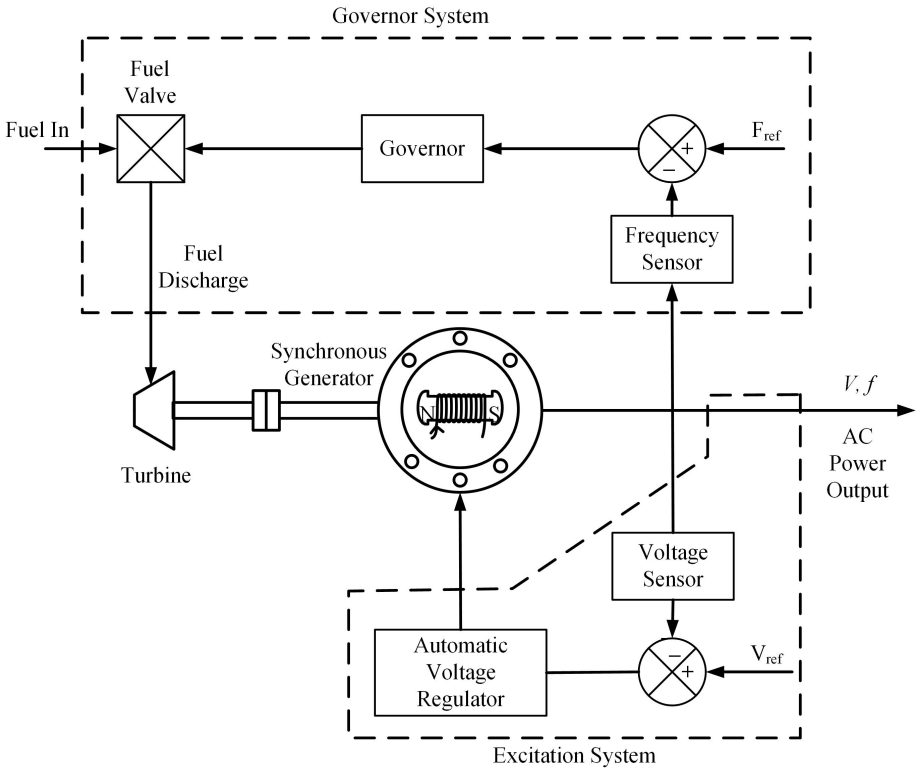

Figure 2.5. Detailed diagram of the diesel generator with governor and excitation system.

1) Governor system for frequency control

The frequency of a system is dependent on active power balance between generation and consumption. Whenever there is imbalance between generation and consumption, the frequency of the system changes from the nominal value. There should be a closed loop system, which balances the generation and the consumption to maintain the frequency at nominal value. Such a system to regulate the frequency of the system is known as “the governor system.” Depending upon the requirements, there are two types of governors in diesel generators:

(a) Isochronous/ Constant speed governor

Figure 2.6 shows the schematic of an isochronous governor. An isochronous

governor tries to bring the system frequency to nominal frequency. It has an integrator controller resulting in constant speed. This kind of governor is suitable, especially for remote microgrids, where a single generator supplies all the load or when only one generator reacts to the change in load to regulate the frequency. Without any communication channel, this kind of governor is not suitable in a multi-generator system because small changes in frequency would lead governors to fight with each other.

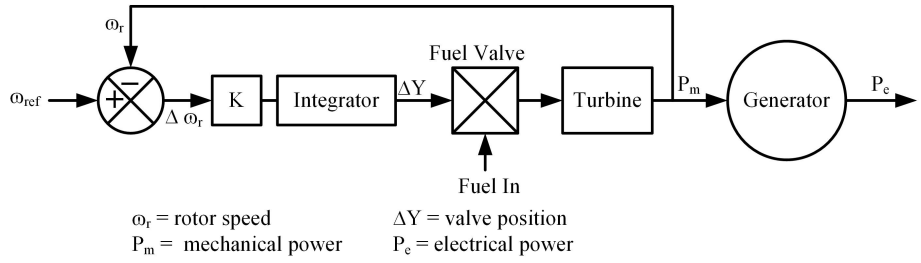

Figure 2.6. Schematic of an isochronous governor.

Figure 2.7 shows the time response of an isochronous governor during an increment in load in the system. The increment in electrical load P_e causes the frequency to fall. The isochronous governor senses this error in frequency and increases the mechanical power P_m by increasing the opening of the fuel valve until there is balance between the mechanical power and electrical power. The frequency is brought back to nominal frequency in the end.

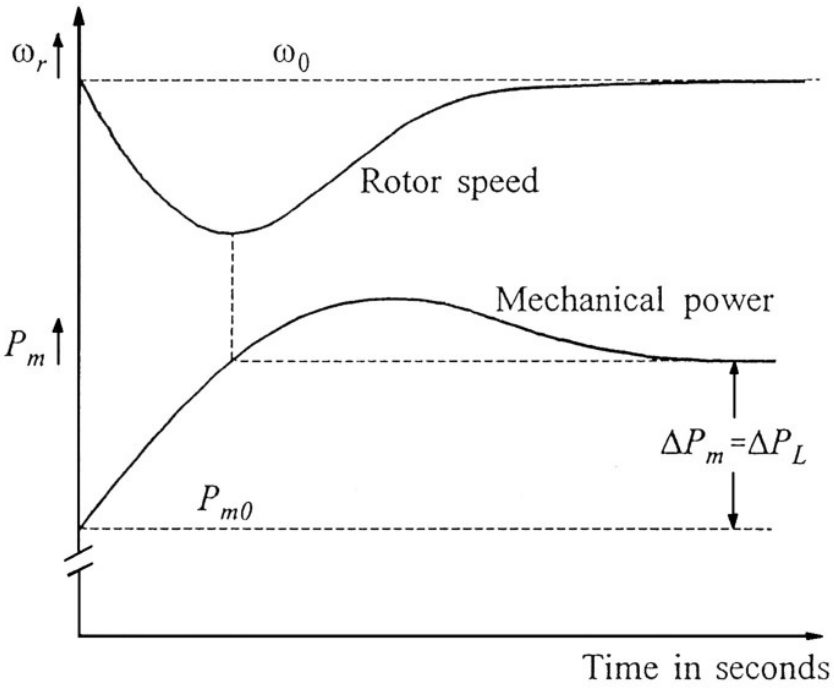

Figure 2.7. Rotor speed and mechanical power response with isochronous generator [25].

(b) Governor with droop characteristics

Figure 2.8 shows the schematic of a droop governor. A droop governor provides the speed regulation or droop to provide the power sharing among parallel generators. It has a proportional controller with a gain of $1/R$ in feedback of the original controller, resulting in droop in speed.

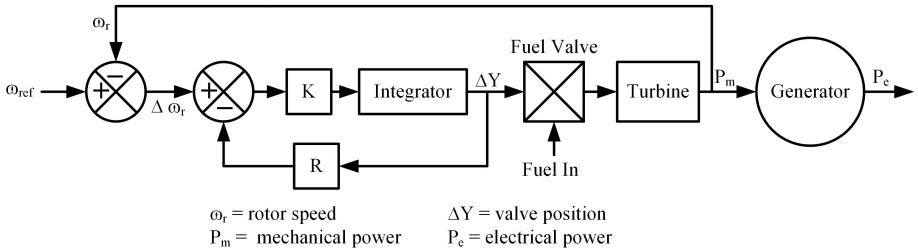

Figure 2.8. Schematic of a droop governor

Figure 2.9 shows the time response of a droop governor during an increment in

load in the system. The increment in electrical load P_e causes the frequency to fall. The droop governor senses this error in frequency and increases the mechanical power P_m by increasing the opening of the fuel valve. Due to the droop, there is a final frequency deviation of $\Delta\omega_{ss}$.

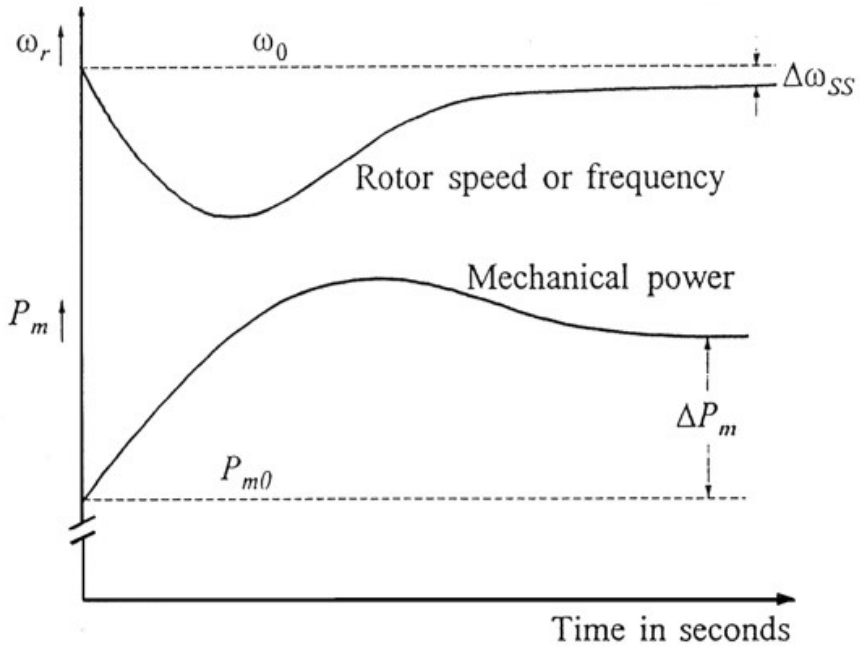

Figure 2.9. Rotor speed and mechanical power response with droop generator [25].

2) Excitation system for voltage control

Figure 2.10 shows the detailed schematic of an excitation system in a diesel generator. Whenever there is change in the load or change in reactive power demand in the system, the voltage of the system changes. The excitation system always maintains constant AC voltage across the stator terminals, senses the voltage of the system and compares it with the reference voltage. The error in voltage is sent to the controller, which controls the amount of Dc current flowing through the rotor windings (field windings). Controlling DC current through rotor windings manipulates the magnetic

field that crosses the stator winding. Thus, the AC voltage induced across the stator windings is controlled by the excitation system.

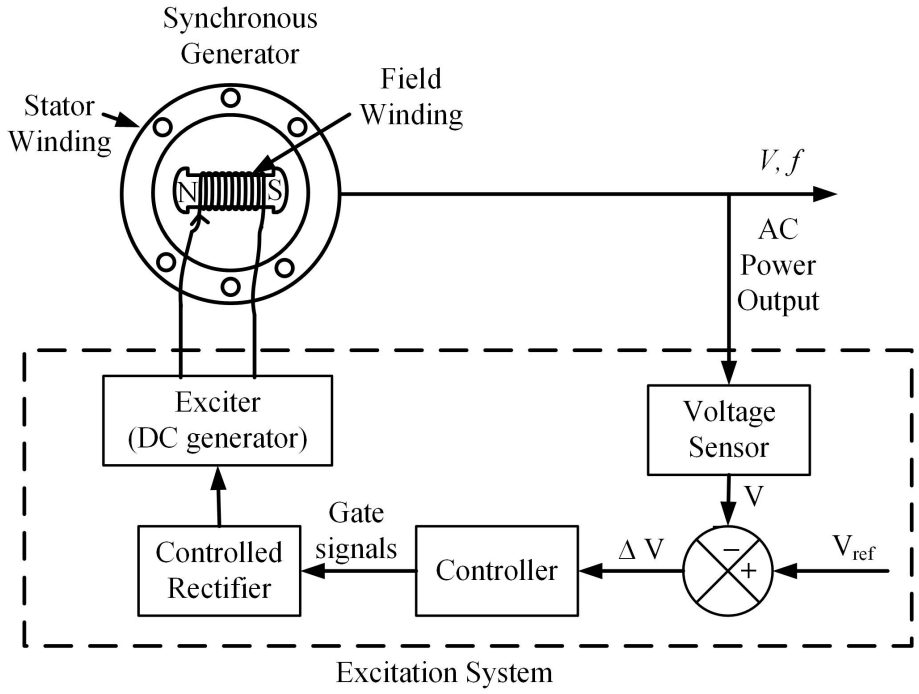

Figure 2.10. Detailed schematic of an excitation system.

2.1.3 Applications of grid scale energy storage system

Grid scale ESS can be used to support generation, transmission, and distribution [26]. Moreover, small scale ESS installed by the consumers in the form of PV system with battery backup or in the form of electric vehicle, can be applied for backup power supply during energy outage, peak saving, etc. According to [27], there are eight main applications of ESS, which are explained below.

1. Peak saving

   ESS can be used to deliver energy to the load during the peak load in the grid or can be charged during the peak generation from renewable energy sources. On the other,

ESS can be applied for energy time shift by delivering energy during high electricity price in the grid or charge them during low electricity price. Moreover, ESS can reduce stress of the grid by providing energy during the congestion in the transmission line or the distribution line. On the other hand, ESS give the option of energy deferral during the upgrade of transmission line or distribution line.

2. Frequency regulation

   Frequency regulation in the grid can be achieved by using ESS to balance the generation and the load at a long time-frame. Frequency regulation can be provided by a balancing authority, following the NERC standards for balancing authority performance control.

3. Islanded microgrids

   In order to make the islanded microgrid reliable and economical, ESS can be used in addition to other renewable energy sources. ESS in microgrid can be used for energy supply during deficit in energy, black start, support voltage and frequency, etc.

4. Volt/var suppport

   The fluctuations in the voltage can be reduced by supplying the reactive power from ESS, when the voltage is low and by absorbing the reactive from ESS, when the voltage is high. The volt/var support is one of the important feature of a smart inverter that can support high penetration of renewable energy to the grid.

5. Power quality

   The voltage sag or interruption in voltage due to fault in the system lead to power

quality issues in the system. ESS may inject the real power for a short time interval to mitigate this problem and improve the power quality.

6. Frequency control

   Frequency control is the another name for frequency response. The frequency of the system falls when there is sudden loss of generation or increase in the load. The deficit in the power at that instant can be delivered from ESS and maintain the frequency. ESS can participate in a primary frequency control and a secondary frequency control. The primary frequency lasts for few seconds and the secondary frequency control lasts for few minutes.

7. PV smoothing

   Fluctuations in the output power from the intermittent PV systems causes voltage excursions for a small time. ESS can smoothen the output power from PV systems for a short time interval and mitigate the voltage excursion issues.

8. PV firming

   As an application of ESS, PV firming supplements the power output from PV systems to provide steady state power to the load for a certain time-frame. ESS deliver power to the load, when the output from PV is insufficient to meet the demand or absorb the power from PV systems, when the output power from them exceed the demand.

2.1.4 Lifetime of battery

There are different technologies for ESS such as the lead acid batteries, the lithium ion batteries, the super capacitors, etc. Among them, the lead acid batteries are the most

commonly used batteries. Every lead acid battery has a rated charge life (Ah). The lead acid batteries are supposed to have completed its lifetime, when the total effective Ah usage of the battery reaches its rated value. The effective Ah depends on the depth and the rate of discharge [28]. The approximate effective Ah that can be delivered by a lead acid battery, with the total size of Q Ah is approximately $390 \times Q$ [29].

2.1.5 Stability of PV-diesel generator microgrids

The stability of a power system is defined as the ability of the system to return back to its steady state when subjected to a disturbance. Mainly, power system stability is categorized into a steady state, as well as a transient and a dynamic stability.

1) Steady state stability

   Steady state stability studies the ability of the system to return to a steady state after gradual and small changes in the power system.

2) Transient stability

   Transient stability of the power system refers to the ability of the power system to remain in synchronism following a major disturbance, such as the tripping of a big generator or a big load due to fault or any other factors.

3) Dynamic stability

   Dynamic stability of the power system refers to the ability of the power system to remain in synchronism following continuous small disturbances, such as random fluctuations in generations or loads. It is also called “small-signal stability.” This thesis discusses about the dynamic stability issues in the PV-diesel generator microgrid system and mitigates this issue.

From a linearized model of power system frequency dynamics, the ROCOF, $\frac{d\Delta f}{dt}$ of the system can be calculated as follows [25]:

$$\frac{d\Delta f}{dt} = \frac{f_0}{2HS_b}\left(\Delta P_m - \Delta P_{load}\right) \tag{2.2}$$

where $\frac{d\Delta f}{dt}$ is the ROCOF of the system, f_0 is the nominal frequency, H is inertia constant, S_b is the rated apparent power, P_m is the input mechanical power and P_{load} is the electrical load in the system. From (2.2), it is obvious that the difference in the input mechanical power and the electrical load due to change in load or the generation brings frequency deviation from nominal frequency along with ROCOF. ROCOF is inversely proportional to the inertia constant of the system, H. Higher the inertia constant, lower is the ROCOF of the system and vice versa. The inertia constant of a power system is defined as the ratio of stored energy at a rated speed of rotor to the apparent power rating of the system. It is calculated as follows:

$$H = \frac{Stored\ energy\ at\ rated\ speed\ of\ rotor}{Apparent\ power\ rating} = \frac{1}{2}\frac{J\omega^2}{S_b} \tag{2.3}$$

where H is inertia constant, J is moment of inertia, ω is speed of the rotor and S_b is the rated apparent power of the system. Due to the increment of low inertia PV systems in the PV-diesel generator microgrids, the inertia constant of the microgrids decreases leading to dynamic frequency stability issues.

In order to balance the generation and load for frequency control, there are various control actions taken over a continuum of time. Figure 2.11 shows the frequency control

actions taken over a continuum of time in a power system. The control actions taken for frequency stability are explained as follows [30]:

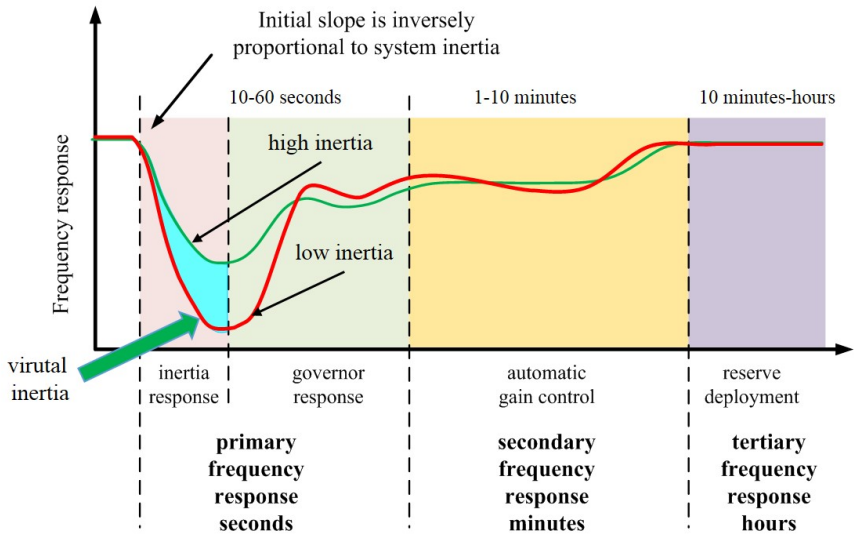

Figure 2.11. Frequency control over a continuum of time.

1) Primary frequency response

Primary frequency response takes place within the first few seconds (10-60 s) following a change in system frequency due to disturbance. Governors of the generator and motor loads take part in primary frequency response. The governors adjust the valve opening to control the flow of diesel to balance the load and generation. Moreover, the motors that are connected in the system run on low speed when the frequency of the system falls. Motors while operating in low speed draw less energy from the system. Primary frequency response is very important for islanded microgrids. The initial slope of frequency (i.e. ROCOF) is inversely proportional to the inertia of the system. For a system with higher inertia (higher spinning reserve), the ROCOF is lower and minimum frequency is higher for same disturbance in comparison to the system with lower inertia (lower spinning reserve). Green curve and

red curve in Figure 2.11 are the frequency responses with higher and lower system inertia, respectively. Due to this, the frequency relays may trip and lead to dynamic frequency stability problems in the low inertia PV-diesel generator microgrid. In such microgrids, inertia needs to be added externally to improve the dynamic frequency stability of the system.

2) Secondary frequency response

Secondary frequency response in the power system takes place within minutes (1-10 minutes) of the disturbance in the system. This control is provided by both the spinning and non-spinning reserve in the power system. Automatic generation controller (AGC) is one of the main common means of providing secondary frequency response in the power system.

3) Tertiary frequency response

Tertiary frequency responses are the actions taken to get the resources in place to handle the present or future disturbances in the power system. Deployment or restoration of the reserves are the actions taken for tertiary frequency response.

2.2 Modeling and control of voltage source inverter

The linear mathematical equation, of the physical voltage source inverter is derived in the modeling of three phase source inverters. For simplicity, non linear terms in the modeling are neglected. The derived mathematical model of the inverter is used to design the controller with required specifications.

2.2.1 Voltage source inverter

A voltage source inverter is a power electronics converter which converts the DC input voltage to a symmetrical AC output voltage of desired magnitude and frequency. The DC input voltage is fixed and uncontrollable, but the AC output voltage is controllable. The inverter output voltage can be changed by varying the inverter gain. Inverter gain is defined as the ratio of peak of output AC voltage to input DC voltage. Pulse width modulation (PWM) is used to accomplish the control of inverter's voltage and frequency. PWM technique determines the *on* and off state of each switch in the inverter. A low pass filter (LC or LCL) is connected in the output of the inverter to obtain sinusoidal AC output voltage. In an ideal case, the inverter output voltage is sinusoidal.

Inverters are mainly classified into two types: a) single phase inverter and b) three phase inverter. Inverters use electrical switches such as bipolar junction transistors (BJTs), metal oxide semiconductor field effect transistors (MOSFETs), gate turn off thyristors (GTOs), and so on.

There are different types of PWM techniques such as sinusoidal pulse width modulation (SPWM), space vector modulation (SVM), hysteresis, and so on. SPWM is one of the popular PWM techniques. Figure 2.12 shows the working principle of SPWM. A modulating signal (i.e. sinusoidal signal) with required output frequency, f_1, and voltage, V_{mod}, is compared with the carrier signal (i.e. triangular waveform) with peak of $V_{carrier}$ and frequency of f_{sw}. The frequency of carrier signal determines the switching frequency of the inverter. The ratio of peak of modulating signal (V_{mod}) to the peak of carrier signal ($V_{carrier}$) is called an amplitude modulation ratio (m_a) of SPWM and is given

by

$$m_a = \frac{|V_{mod}|}{|V_{carrier}|} \tag{2.4}$$

where $|V_{mod}|$ is the magnitude of the modulating signal, and $|V_{carrier}|$ is the magnitude of carrier signal.

The magnitude of carrier signal is fixed, and magnitude of modulating signal is changed to control the output voltage of the inverter. Similarly, the ratio of frequency of modulating signal to the frequency of carrier signal is called the frequency modulation ratio (m_f) and is given by

$$m_f = \frac{f_1}{f_{sw}} \tag{2.5}$$

where f_1 is the frequency of modulating signal and f_{sw} is the frequency of the carrier signal.

Figure 2.13 shows the circuit diagram of a PWM single phase inverter. It has one leg with two switches S_{A+} and S_{A-}. Switches S_{A+} and S_{A-} are controlled by the output of comparison of modulating signal with the carrier signal. Both the switches S_{A+} and S_{A-} are never turned *on* together because turning them *on* together short circuits the input DC source. So the switching patterns for them are given as complementary to each other with some dead time for the factor of safety. The switch turns *on* and off sequence is obtained as follows:

$if\ V_{mod} > V_{carrier}:\ S_{A+}\ is\ ON\ and\ S_{A-}\ is\ OFF:\ V_{A0} = \frac{1}{2}V_{dc}$

$if\ V_{mod} < V_{carrier}:\ S_{A+}\ is\ OFF\ and\ S_{A-}\ is\ ON:\ V_{A0} = -\frac{1}{2}V_{dc}$

Figure 2.12(b) shows the output voltage V_{a0} of the inverter for m_a= 0.8 and m_f =15.

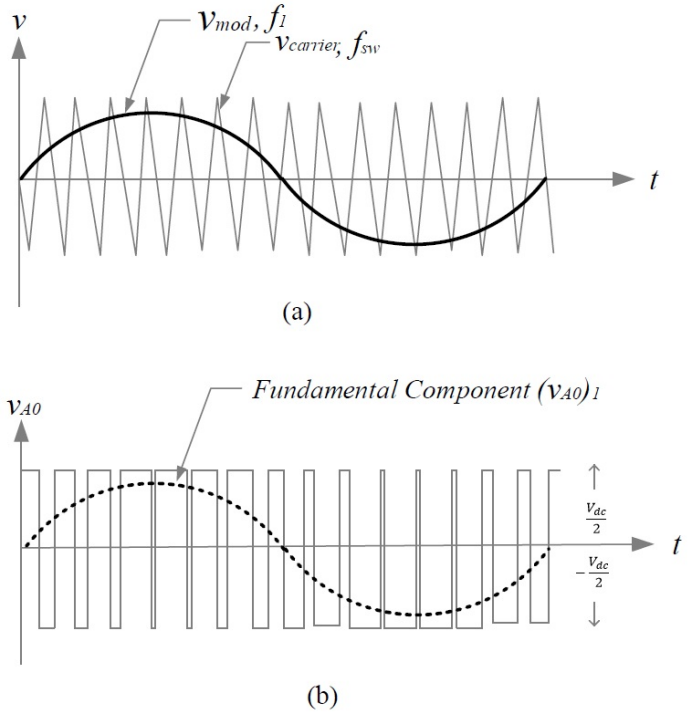

Figure 2.12. a) single phase sinusoidal PWM b) output voltage of single phase inverter and its fundamental component [31].

The output voltage of the fundamental component $(V_{A0})_1$ can be calculated as follows:

$$(V_{A0})_1 = m_a \frac{V_{dc}}{2} \tag{2.6}$$

where V_{DC} is the DC voltage of the input DC source.

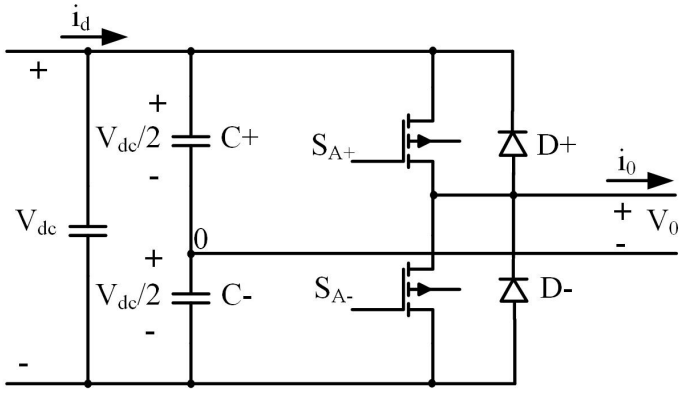

Figure 2.13. Circuit diagram of single phase PWM inverter [31].

Figure 2.14 shows the relationship between the input DC voltage and output AC voltage for single phase SPWM inverter. The relationship between input DC voltage and output AC voltage is linear for amplitude modulation up to 1.0. When the amplitude modulation crosses 1.0, it reaches over modulation zone until the amplitude modulation is 3.24. When the amplitude modulation crosses 3.24, it reaches a square wave region where the output AC voltage becomes square wave. In order to get sinusoidal output voltage, the inverter must be operated in linear zone with the amplitude modulation between 0 and 1.

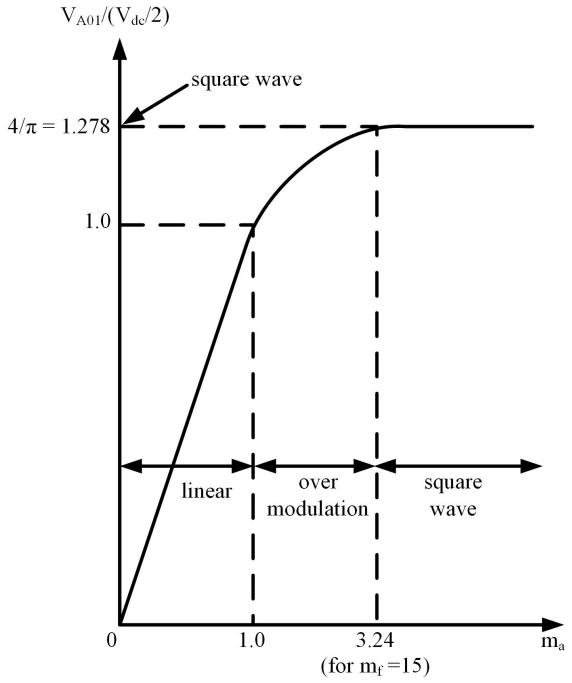

Figure 2.14. Single phase inverter ac voltage control by varying m_a [31].

Figure 2.15 shows the circuit diagram of a three phase PWM inverter. It consists of three legs, one for each phase. Each inverter leg is similar to the one leg inverter in figure 2.13.

In order to obtain balanced three phase output voltage in three phase PWM inverter, three sinusoidal voltage of same magnitude but 120° out of phase are compared with same

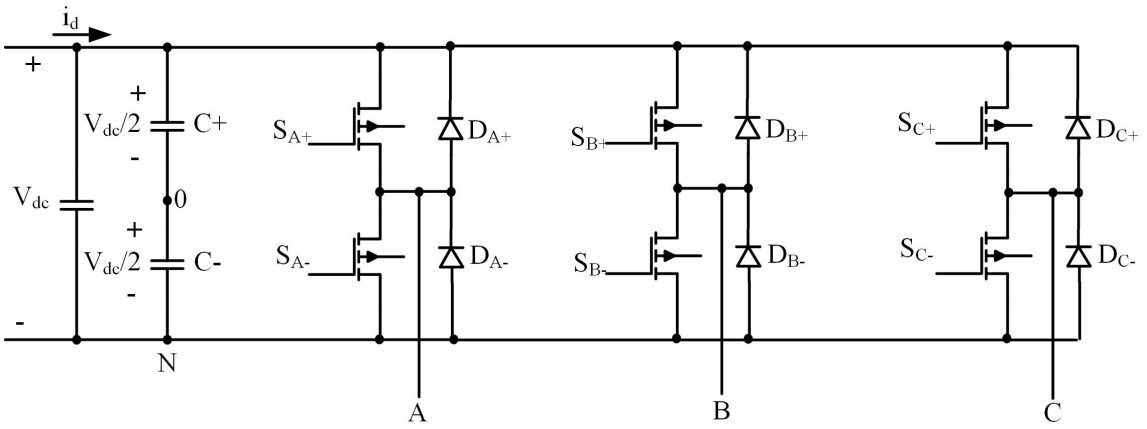

Figure 2.15. Circuit diagram of three phase PWM inverter [31].

triangular waveform as shown in Figure 2.16. The frequency modulation (m_f) of this PWM is 15. Output voltage of each leg (such as V_{AN}) is dependent on the input DC voltage V_{dc} and amplitude modulation (m_a). The inverter leg A and leg B voltage (V_{AN} and V_{BN}) with respect to DC voltage ground is shown in Figure 2.16 b) and c) respectively. Figure 2.16 c) shows the inverter output line voltage (V_{AB}) and the fundamental component of it. The line-to-line rms voltage at the fundamental frequency of inverter output voltage can be written as

$$V_{LL1}(line-to-line,\ rms) = \frac{\sqrt{3}}{\sqrt{2}}(V_{AN})_1 = 0.612 m_a V_d \tag{2.7}$$

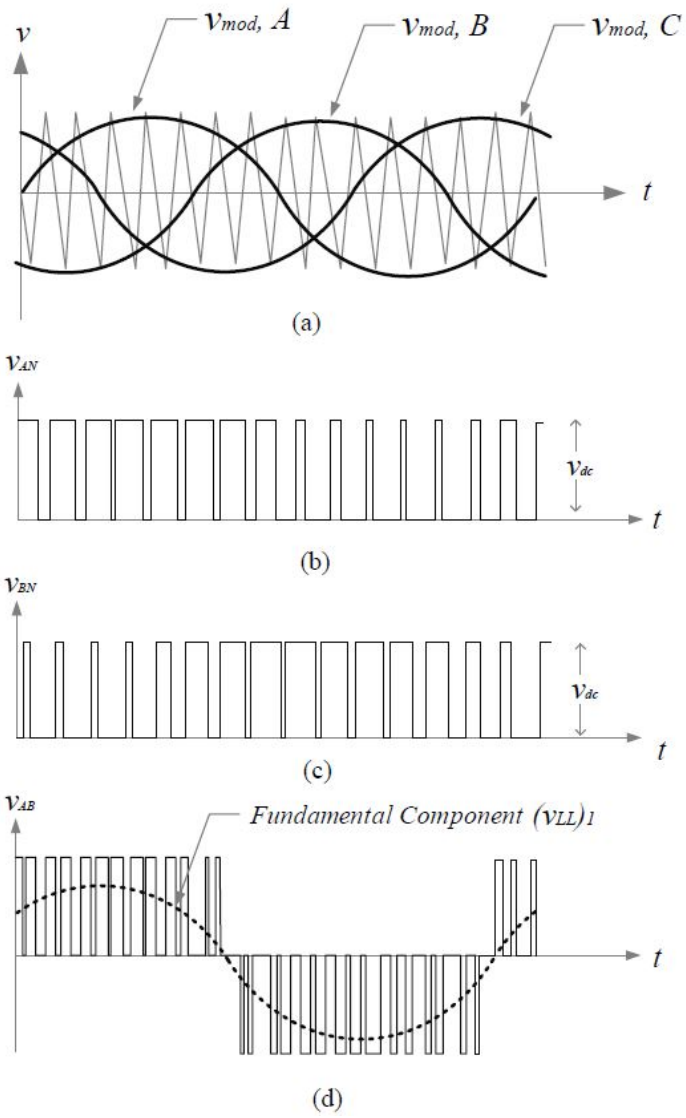

Figure 2.16. Three phase sinusoidal PWM waveforms [31].

Figure 2.17 shows the relationship between the input DC voltage and output AC voltage for three phase SPWM inverter. The relationship between input DC voltage and output AC voltage is linear for amplitude modulation upto 1.0. When the amplitude modulation crosses 1.0, it reaches over modulation zone until the amplitude modulation is 3.24. When the amplitude modulation crosses 3.24, it reaches square wave region where the output AC voltage becomes a square wave. In order to get sinusoidal output voltage,

the inverter must be operated in the linear zone with the amplitude modulation between 0 and 1.

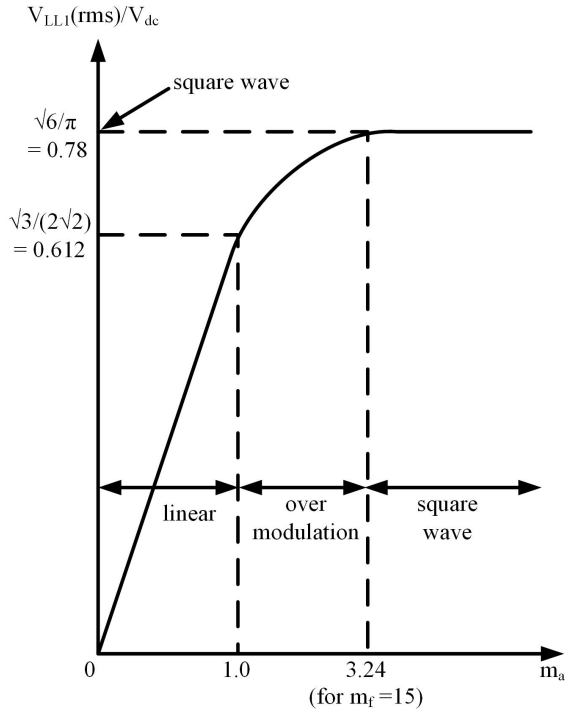

Figure 2.17. Three phase inverter AC voltage control by varying m_a [31].

2.2.2 Three phase transformation theory

The three phase power system or machines are defined by the voltage and current equations. The coefficients of those equations are time varying which makes the mathematical modeling of such systems complex. For simplicity's sake, mathematical transformations are used to solve equations involving time varying quantities by referring all variables into a common frame of reference. Among the various transformations available, the well known are:

1) Stationary frame (Clarke's) transformation,

2) Rotating frame (Park's) transformation.

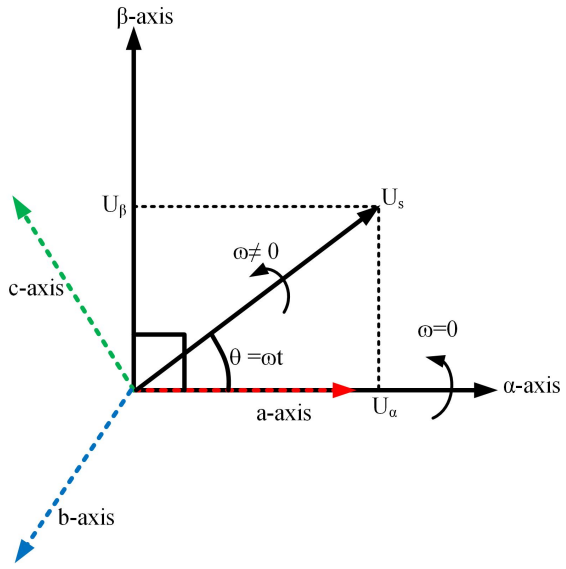

Figure 2.18. Representation of stationary (Clarke's) transformation.

Clarke's transformation converts the three phase coordinates (abc) into two phase time-varying orthogonal coordinates ($\alpha\beta$) as shown in Figure 2.18. The α component is always is in synch with phase A of abc coordinate, and β component is orthogonal to α component. The vector U_s can be represented as:

$$\vec{U}_s = |\vec{U}_s|\angle\theta = U_\alpha + jU_\beta = \frac{2}{3}\left(u_a + u_b e^{j\frac{2\pi}{3}} + u_c e^{-j\frac{2\pi}{3}}\right) \tag{2.8}$$

where

$$|\vec{U}_s| = \sqrt{u_\alpha^2 + u_\beta^2} \tag{2.9}$$

$$\theta = \omega t = tan^{-1}\left(\frac{U_\beta}{U_\alpha}\right) \tag{2.10}$$

$$e^{\pm\frac{2\pi}{3}} = cos\left(\frac{2\pi}{3}\right) \pm jsin\left(\frac{2\pi}{3}\right) \tag{2.11}$$

The zero sequence component, u_0, is given by:

$$u_0 = \frac{1}{3}(u_a + u_b + u_c) \tag{2.12}$$

From (2.8), (2.11) and (2.12), the Clarke's transformation matrix can be derived:

$$\begin{bmatrix} u_\alpha \\ u_\beta \\ u_0 \end{bmatrix} = \frac{2}{3} \begin{bmatrix} 1 & cos\left(\frac{2\pi}{3}\right) & cos\left(-\frac{2\pi}{3}\right) \\ 0 & sin\left(\frac{2\pi}{3}\right) & sin\left(-\frac{2\pi}{3}\right) \\ \frac{1}{2} & \frac{1}{2} & \frac{1}{2} \end{bmatrix} \begin{bmatrix} u_a \\ u_b \\ u_c \end{bmatrix} \tag{2.13}$$

$$or, \left[F_{\alpha\beta 0}\right] = [C]\left[F_{abc}\right] \tag{2.14}$$

where $[C]$ is the Clarke's transformation matrix. The variables from $\alpha\beta$ coordinate can be transformed into abc coordinate using the inverse of Clarke's transformation matrix as:

$$[F_{abc}] = [C]^{-1}\left[F_{\alpha\beta 0}\right] \tag{2.15}$$

The real and reactive power consumed by a load or supplied by a source can be easily calculated as:

$$activepower(p) = u_\alpha i_\alpha + u_\beta i_\beta = \bar{p} + \tilde{p} \tag{2.16}$$

$$reactivepower(q) = u_\alpha i_\beta - u_\beta i_\alpha = \bar{q} + \tilde{q} \tag{2.17}$$

The Park's transformation converts the quantities from three phase (abc) coordinate into rotating frame dq coordinate frame, which is time invariant in nature, as shown in

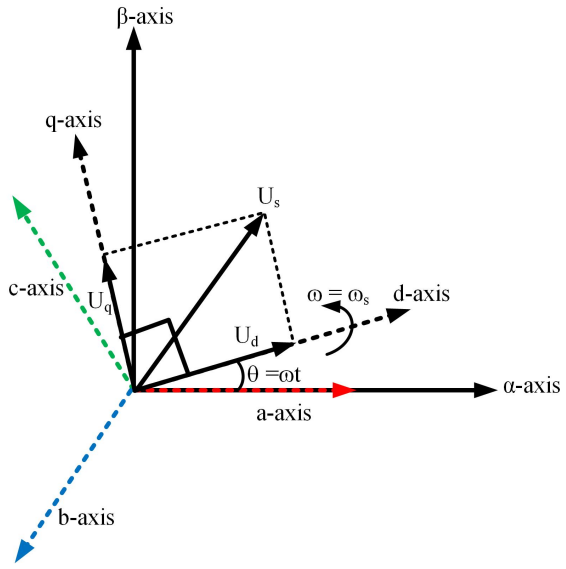

Figure 2.19. Representation of rotating /Park's transformation.

Figure 2.19. Park's transformation is an extension of Clarke's transformation in which the the orthogonal quantities obtained from Clarke's transformation are applied with rotating quantity to transform into rotating frame quantities, as shown in Figure 2.20.

Clarke's transformation + Rotation = Park's transformation

Figure 2.20. Relation between Clarke's transformation and Park's transformation.

It first transforms quantities in abc coordinate frame into a two-axis orthogonal stationary reference frame quantities $(\alpha\beta)$ which is transformed into dq frame using a rotational quantity. The dq quantities from Park's transformation can be calculated as follows

$$\vec{U}_s = U_d + jU_q = \left(U_\alpha + jU_\beta\right).e^{-j\omega t} = \frac{2}{3}\left(u_a + u_b e^{j\frac{2\pi}{3}} + u_c e^{-j\frac{2\pi}{3}}\right).e^{-j\omega t} \qquad (2.18)$$

From (2.8), (2.11) and (2.18), the following relation can be derived as

$$\begin{bmatrix} u_d \\ u_d \\ u_0 \end{bmatrix} = \frac{2}{3} \begin{bmatrix} cos(\omega t) & cos\left(\omega t - \frac{2\pi}{3}\right) & cos\left(\omega t + \frac{2\pi}{3}\right) \\ -sin(\omega t) & -sin\left(\omega t - \frac{2\pi}{3}\right) & -sin\left(\omega t + \frac{2\pi}{3}\right) \\ \frac{1}{2} & \frac{1}{2} & \frac{1}{2} \end{bmatrix} \begin{bmatrix} u_a \\ u_b \\ u_c \end{bmatrix} \tag{2.19}$$

$$or, \left[F_{dq0}\right] = [P]\,[F_{abc}] \tag{2.20}$$

where $[P]$ is the Park's transformation matrix. The angular time (θ=ωt) can be obtained from (2.10). The variables from dq coordinates can be transformed into abc coordinates using the inverse of Parks's transformation matrix as

$$[F_{abc}] = [P]^{-1}\left[F_{dq0}\right] \tag{2.21}$$

The real and reactive power consumed by a load or supplied by a source can be easily calculated as

$$activepower(p) = \frac{3}{2}\left(u_d i_d + u_q i_q\right) \tag{2.22}$$

$$reactivepower(q) = \frac{3}{2}\left(u_d i_q - u_q i_d\right) \tag{2.23}$$

where i_d and i_q are d and q axis components of current, respectively. If the synchronous rotating frame in Figure 2.19 is in phase with the $\vec{U}_s$, then the d-axis component becomes equal to the magnitude of voltage (i.e. u_d=u_{peak}), and the q-axis component becomes zero.

(2.22) and (2.23) can be modified as

$$activepower(p) = \frac{3}{2}(u_d i_d) \tag{2.24}$$

$$reactivepower(q) = \frac{3}{2}(u_d i_q) \tag{2.25}$$

From (2.24) and (2.25), it is obvious that the active power and reactive power in the system can be independently manipulated by controlling i_d and i_q currents respectively.

2.2.3 Dq modeling of three phase voltage source inverter

Figure 2.21 shows a three phase grid connected VSI with LC filter and a load. LC filter attenuates the unwanted noise from the inverter that appears due to the switching of the inverter switches. VSI can be operated either in current control mode or in voltage control mode. In this report, modeling and control of CC-VSI is presented because CC-VSI is used in VI.

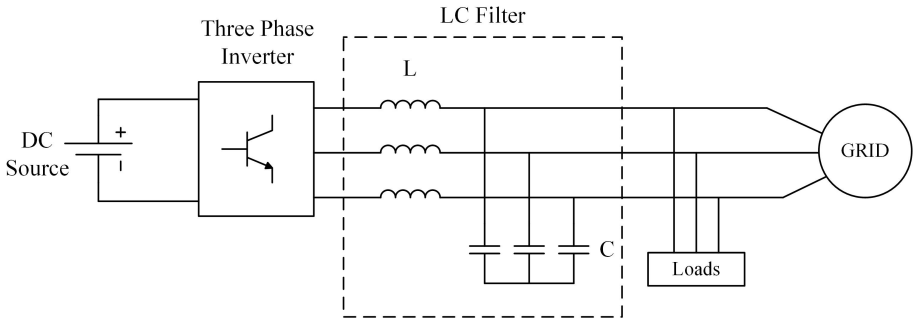

Figure 2.21. Grid connected three phase PWM inverter with load.

In order to get the mathematical model of the CC-VSI, the per phase equivalent model of three phase CC-VSI in s-domain is derived as in Figure 2.22. The inverter is considered as an ac voltage source inverter. R and L are the resistance and inductance of

the inductor respectively. C is the capacitance of the capacitor. i_L is the inductor current and $v_{inverter}$ is the voltage across the CC-VSI.

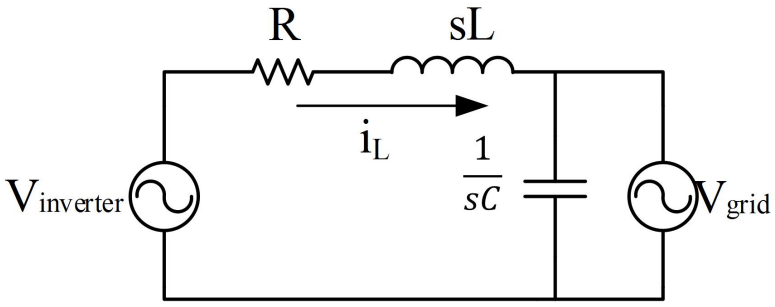

Figure 2.22. Per phase model of three phase current controlled voltage source inverter.

For a perfectly sinusoidal grid with only the fundamental component (i.e. 60 Hz component), the capacitor of a LC filter is assumed to be the short circuit so the per phase model in Figure 2.22 is modified as in Figure 2.23.

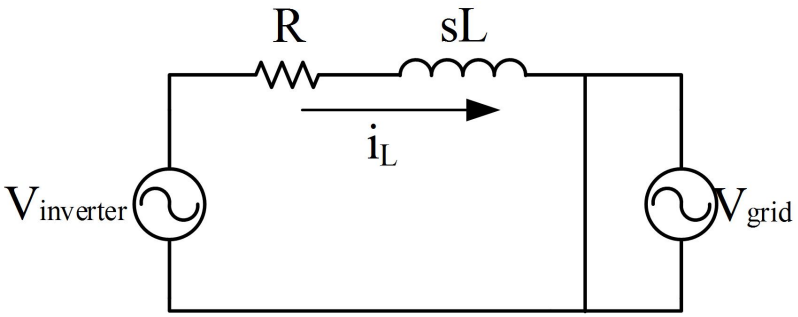

Figure 2.23. Per phase equivalent model of three phase current controlled voltage source inverter of Figure 1.27.

Since the short circuit is in parallel to the grid, the grid is also supposed to be short circuit in equivalent per phase model as shown in Figure 2.24. The grid voltages are added as feed forward signals in the controller design of CC-VSI. This is the final equivalent per phase model of the CC-VSI.

Applying KVL, in the circuit of Figure 2.24, the transfer function of the plant is

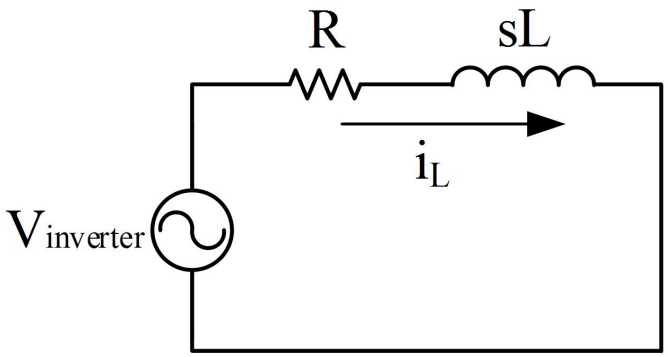

Figure 2.24. Per phase equivalent model of three phase current controlled voltage source inverter of Figure 1.28.

obtained as

$$G(s) = \frac{i_L}{v_{inverter}} = \frac{\frac{1}{L}}{s + \frac{R}{L}} \tag{2.26}$$

In order to control the current in CC-VSI, the three phase variables inverter's current, inverter's voltage and grid's voltage are transformed from abc coordinates to dq coordinates using Park's transformation. When transforming from abc coordinates to dq coordinates, the inductor currents in dq frame (i.e. $i_{L,dq}$) introduce cross coupling terms in inverter voltage (i.e. $\omega L I_{L,dq}$) as shown in Figure 2.25.

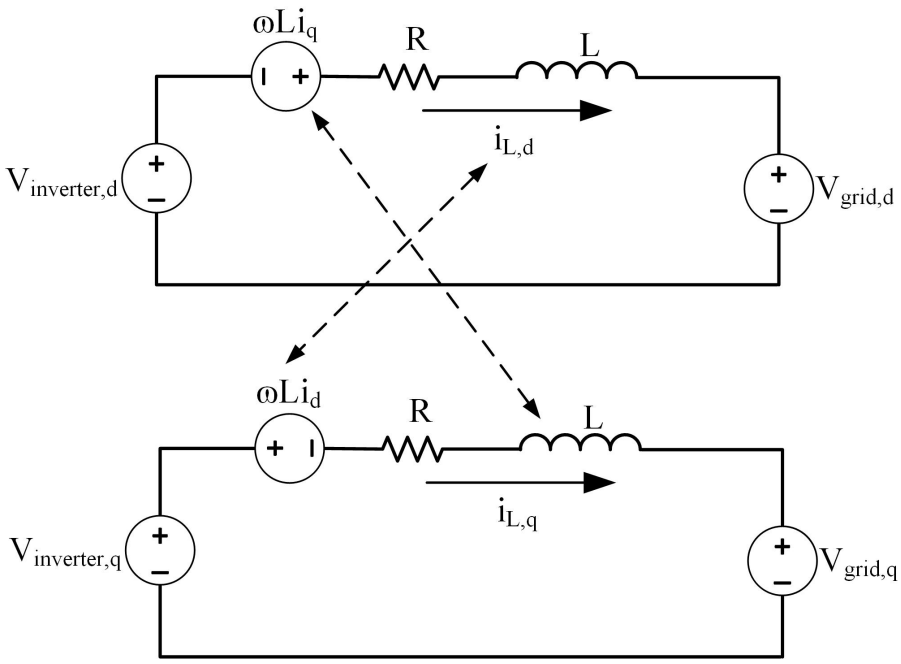

Figure 2.25. Dq equivalent model of three phase CC-VSI.

For simplicity's sake, these cross-coupling terms introduced in inverter voltage, are neglected in current controller design and added later as feed forward terms in controller. The simplified dq equivalent of three phase CC-VSI after neglecting the cross coupling terms is shown in Figure 2.26. So the transfer function of the plant (i.e. CC-VSI) of (2.26) is calculated in dq domain as below.

$$G(s) = \frac{i_{L,dq}}{v_{inverter,dq}} = \frac{\frac{1}{L}}{s + \frac{R}{L}} \tag{2.27}$$

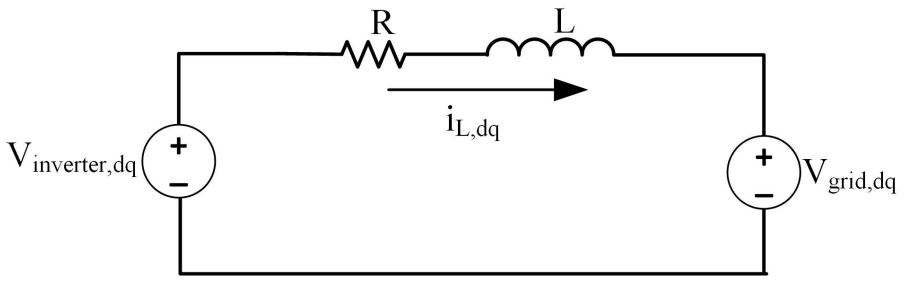

Figure 2.26. Simplified dq equivalent model of three phase CC-VSI.

2.2.4 Dq control of three phase current controlled voltage source inverter

Figure 2.27 shows the schematic diagram of a current controller for a grid connected three phase inverter. The current from the inverter is controlled by controlling the modulating signals for the gate signals of the inverter. The reference current i_L^* is compared with the actual inductor current (i_L) of the inverter. The difference in error is fed to the current controller which takes the necessary action required to generate the necessary gate signal to minimize the error between them.

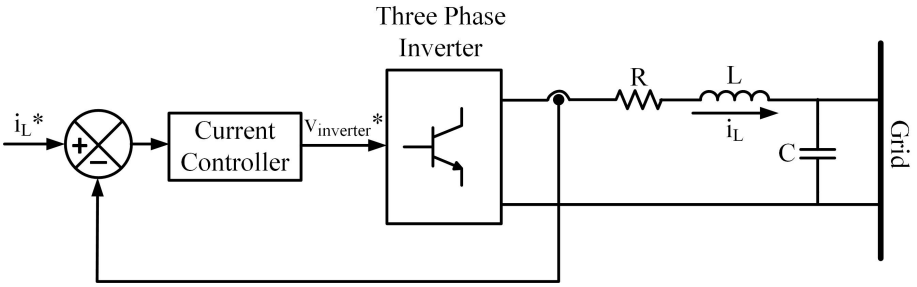

Figure 2.27. Schematic diagram of current controller for a three phase inverter.

Generally, PI controller is used for controller. In this report, PI controller is used for the current controller. The grid voltage and cross-coupling terms that were neglected earlier while modeling the plant are added as the feed forward terms as shown in Figure 2.28.

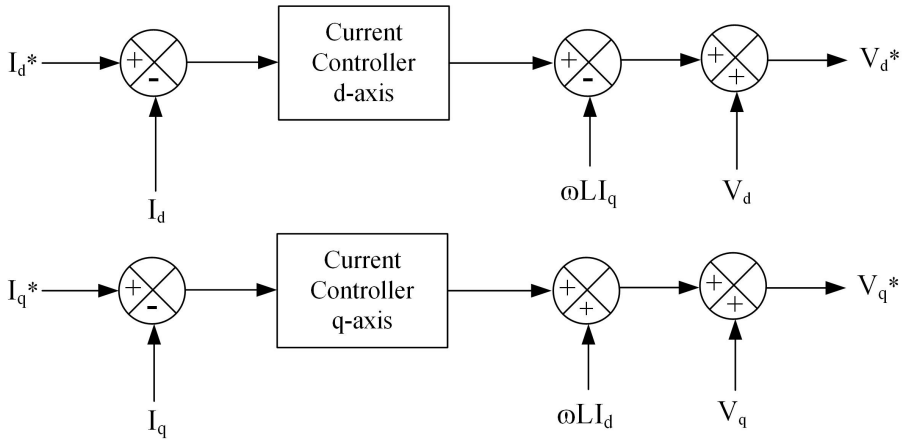

Figure 2.28. Topology of current controller in dq frame with cross coupling terms and grid voltage added as feed forward terms.

2.3 Virtual Inertia

A virtual inertia can be defined as the combination of an ESS, power electronics converter and proper control algorithm that injects or absorbs active power to and from the system to maintain the dynamic frequency stability of the system. Figure 2.29 shows the main components of a VI. It consists of an ESS (such as battery, super capacitor, PV, etc.), current controlled voltage source inverter (CC-VSI) and control loops. There are two control loops, i.e. inner current controller and outer VI reference power calculation loop. The current controller drives the flow of current from the inverter. The outer VI reference power calculation loop generates the reference power for VI. Phase locked loop (PLL) generates the frequency and ROCOF of the system. PLL also generates the phase angle information of the grid voltage to synchronize the inverter current with grid voltage.

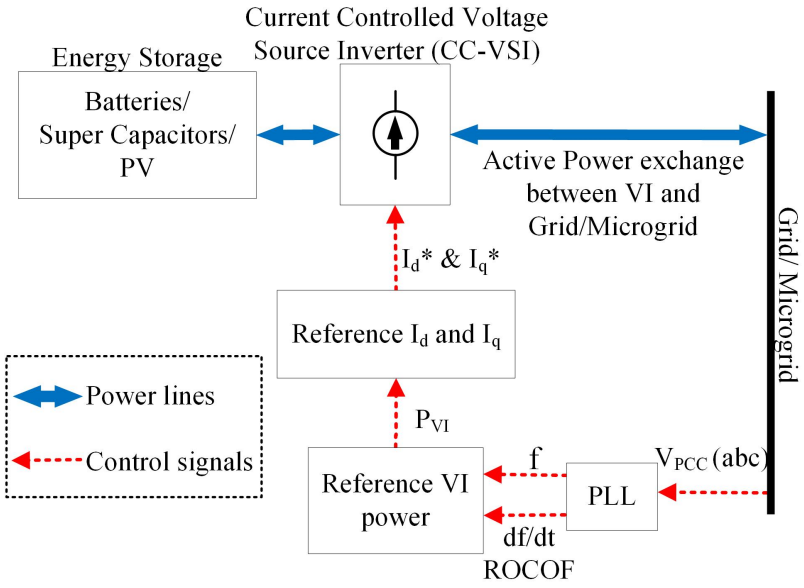

Figure 2.29. Main components of a virtual inertia.

2.3.1 Working principle of virtual inertia

The reference active power to be absorbed or supplied based upon requirement is given by (4.4).

$$P_{VI} = -K_I \frac{df}{dt} + K_D(f^* - f) + K_{SOC}(SOC^* - SOC) \tag{2.28}$$

where K_I is the virtual inertia coefficient, K_D is the virtual damping coefficient or virtual droop coefficient, f^* is the reference frequency, $\frac{df}{dt}$ is ROCOF of the system, and SOC^* is the reference SOC of the ESS at steady state values.

When there is a load increment or decrement in the system, the ROCOF is negative or positive, respectively. During a load increment (i.e. negative ROCOF), the VI needs to inject power to support inertia and control the ROCOF. During a load decrement (i.e. positive ROCOF), the VI needs to consume power to support inertia and control the ROCOF. So there is a negative coefficient in K_I to have a positive power reference during

load increment and a negative power reference during load decrement. K_I is responsible for emulating virtual inertia in the system. K_D is responsible for damping the frequency oscillation and bringing the frequency of the system to reference value (i.e. 60 Hz). The virtual inertia coefficient, K_I, and virtual damping coefficient, K_D, can be calculated as [32]

$$K_I = \frac{P_{VI-nominal}}{\left(\frac{d\Delta f}{dt}\right)_{max}} \tag{2.29}$$

$$K_d = \frac{P_{VI-nominal}}{(\Delta f)_{max}} \tag{2.30}$$

where P_{VI-nom} is the nominal power rating of the VI, Δf is the maximum change in frequency, $\frac{df}{dt}$ is the maximum ROCOF. The maximum inertia that can be emulated by a VI is calculated as as follows [12]

$$H_{emulated} = \frac{K_I f_0}{2P_g} \tag{2.31}$$

where, P_g is the total capacity of the system, K_I is the virtual inertia coefficient and f_0 is the rated frequency of the system.

Generally, a frequency error tolerance band is taken into account to prevent the power inverter from turning ON and OFF for small frequency oscillations. A selection of the value of frequency dead band for tolerance band depends on the condition of the grid. For low inertia microgrids, where the system frequency fluctuates for small perturbation, the dead zone value can be taken higher compared to high inertia microgrids. K_{SOC} is responsible for maintaining the SOC of the ESS. Generally, the reference SOC for energy storage is kept at 0.5 or 0.6, so that the energy storage is always ready to inject or absorb

energy during frequency changes. Moreover, the control of SOC is made slower than the inertia and damping control so that the charging of the ESS does not affect the inertia emulation during the transients.

A general configuration of the working principle of VI is shown in 2.30. The reference power for the VI is calculated from (4.4) based on frequency deviation and ROCOF. This is the outer control loop of the VI. For simplicity, the SOC control portion is not considered in this paper. Power flow from the ESS is controlled by powering the gate signals in the inverter. This is the inner current control loop as shown in Figure 2.30. PLL generated the frequency, ROCOF and the phase angle of the grid voltage. For the inner current control loop, current signals are converted into rotational dq frame because PI controllers cannot track sinusoidal waveforms without any steady state error. Conversion into dq frame helps to control active power and reactive power flow independently. The reference currents for CC-VSI based on the reference power from (4.4) are calculated using (2.32) and (2.33).

$$I_{d\_reference} = \frac{2}{3}\left(\frac{V_d \times P_{VI} - V_q \times Q}{V_d^2 + V_q^2}\right) \tag{2.32}$$

$$I_{q\_reference} = \frac{2}{3}\left(\frac{V_d \times Q - V_q \times P_{VI}}{V_d^2 + V_q^2}\right) \tag{2.33}$$

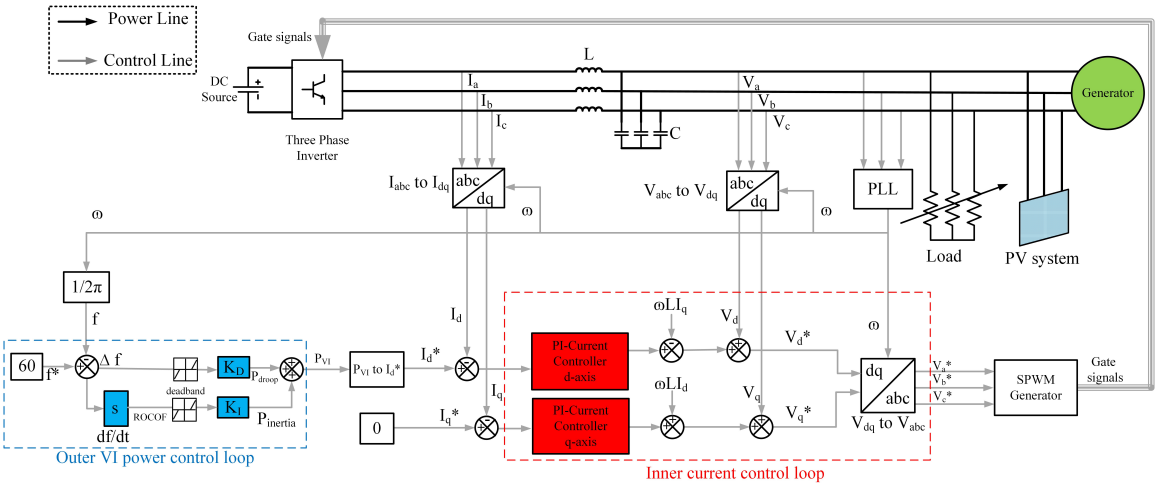

Figure 2.30. Working principle of virtual inertia.

Since the objective of the VI is to control the frequency, only the active power (P_{VI}) is controlled from the inverter and the reactive power (Q) is set to zero in (4.5) and (4.6). Reference I_q current is set to zero and only the reference I_d current is controlled from CC-VSI.

2.3.2 Adaptive dynamic programming based virtual inertia

Figure 2.31 shows the working principle of a ADP based VI. The working principle of VI is the same as is shown in Figure 2.30. ADP controller is added as a supplementary controller in the existing outer control loop of VI. With the addition of VI to the system, the frequency of the system returned to the nominal frequency more slowly. The ADP controller makes the outer control loop of VI adaptive-it learns online and generates the reference power for VI, which is added to the outer control loop of the existing VI.

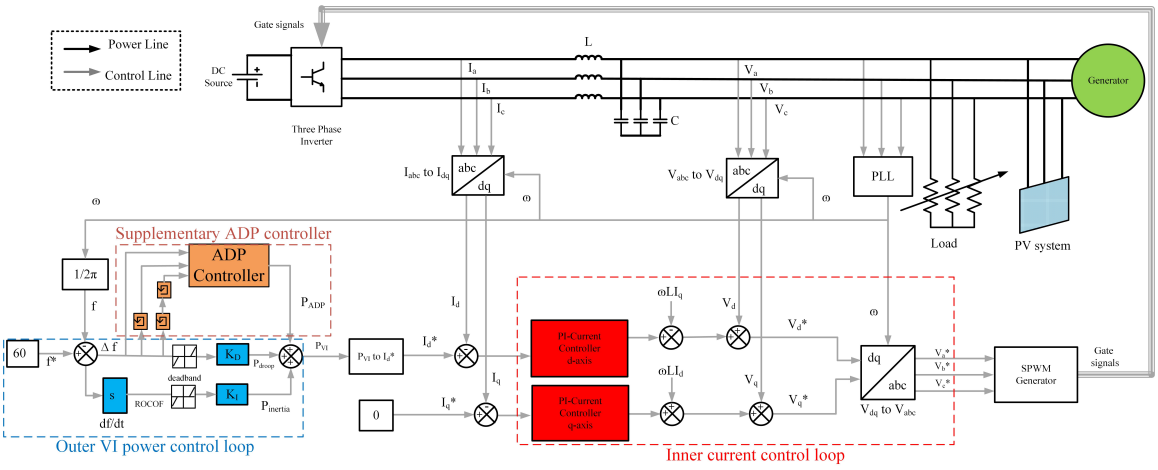

Figure 2.31. Working principle of ADP based VI [33].

Adaptive dynamic programming is an approximate optimal control scheme. A function approximation structure is used to approximate the solution of the Hamilton-Jacobi-Bellman (HJB) equation [17]. The offline iteration algorithm or online update algorithm is used to find the optimal approximate solution. Stability of dynamic systems can be improved by using ADP, which not only improves the stability of dynamic systems but also gives the optimal solution in control system. According to the Bellman principle of optimality, whatever is the initial state or decision, the remaining decisions must constitute an optimal policy with regard to the state resulting from the first decision [34]. This principle is applicable in different systems, such as continuous systems, discrete systems, linear systems, non linear systems, deterministic systems, stochastic systems, etc. ADP controllers can be trained offline and used in the system or made adaptive using online adaptive algorithms. The ADP controllers can be used as the main controllers in the system or as supplementary controllers that supplement the action of existing linear controllers (i.e. PID controllers).

The ADP controller is generally a neural network structure with two different

structures: the action network and the critic network. Neural networks are made up of many artificial neurons. Each input into the neuron has its own weight associated with it as shown in Figure 2.32.

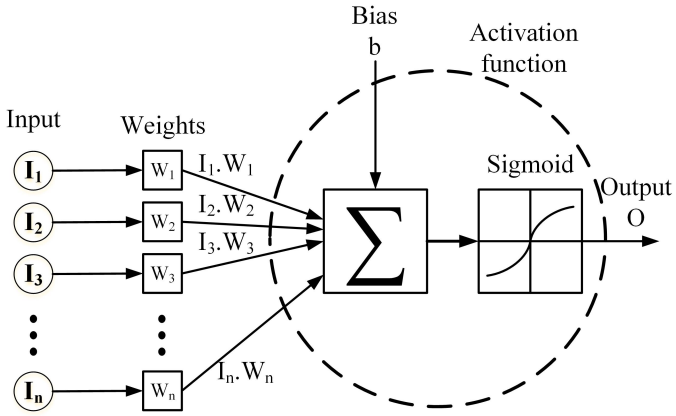

Figure 2.32. Single processing unit of a perceptron [35].

A weight is simply a floating point number and it is adjusted to train the network. A neuron can have any number of inputs from one to n, where n is the total number of inputs. The inputs may be represented therefore as $I_1, I_2, I_3, \ldots, I_n$. The corresponding weights for the inputs as $W_1, W_2, W_3, \ldots, W_n$. The output of any neural network is given by sum of product of all the input by the respective weights as given by (2.34).

$$Output(O) = I_1 \times W_1 + I_2 \times W_2 + I_3 \times W_3 + \ldots + I_n \times W_n \tag{2.34}$$

The discontinuous threshold of perceptron makes it undifferentiable and unsuitable for gradient descent. Hence, a function called as the “sigmoid function” is used to smoothen the results and make it differentiable. Since the sigmoid function maps a very large input domain to a small range of outputs, it is called a “squashing function” too. There are different types of sigmoid functions. The sigmoid function used in this thesis is

an exponential sigmoid given by 2.35.

$$\sigma(y) = \frac{1 - e^{-y}}{1 + e^{-y}} \tag{2.35}$$

The input from (2.34) is continuously fed to sigmoid and the resultant is continuous and differentiable. Figure 2.32 shows the basic diagram of a single perceptron. If multiple of such perceptron are used to form many layers, then such a network is called multilayer perceptron (MLP) . In MLP, the input is connected to different hidden nodes with different weights, and hidden nodes are connected again to different output nodes via different weights. There can be many layers of these kinds of nodes in MLP.

The idea behind the design of the critic network is to adapt weights of the critic network such that the optimal cost function $J^*(X(t))$ satisfied the Bellman principle of optimality given by [17].

$$J^*(X(t)) =_{u(t)}^{min} \{J^*(X(t+1)) + r(X(t)) - U_c\} \tag{2.36}$$

The reinforcement signal can be given externally in the form of binary values as "0" or "1" simply corresponding to "success" or "failure," respectively. In this report, the reinforcement signal for the critic network is calculated by

$$r(t) = -c\left(a_1 X_1^2 + a_1 X_2^2 + a_3 X_3^2\right) \tag{2.37}$$

where X_1, X_2, and X_3 are error between reference signal and actual signal of current time step, one time step before, and two time step before, respectively and c, a_1, a_2 and a_3 are

coefficients of X_1, X_2, and X_3 respectively.

There are two main networks in ADP controller i.e. critic network and action network which as described as follows:

A) The critic network

The critic network adapts the ADP controller online and reinforces action network based upon its performance and response from the system. The output of the critic network, $J(t)$, approximates discounted total reward-to-go. Total reward-to-go is calculated by

$$R(t) = r(t+1) + \alpha r(t+2) + ... \tag{2.38}$$

where $R(t)$ is total reward-to-go at time t, α is a discount factor which is taken as 0.95 and $r(t+1)$ is the external reinforcement signal at $t+1$ time.

The critic network evaluates the performance of the action network and gives $J(t)$ as an approximation of $R(t)$ in (2.36). The prediction error for critic element is calculated by (2.39)

$$e_c(t) = \alpha J(t) = [J(t-1) - r(t)] \tag{2.39}$$

The objective function for the critic network is the square error from (2.39) and calculated by (2.40)

$$E_c(t) = \frac{1}{2} e_c^2(t) \tag{2.40}$$

The weights of the critic network are updated using gradient-based adaptation as given in [36].

B) The action network

Based on memory of association between state, control output of the action network reinforces the system operations. In systems where ADP controllers are used as supplementary controller, the output from action supplements the output from the existing controller (PID controllers) and tries to minimize the error between the reference signal and actual signal in the system.

The error between the desired objective function U_c and approximate J function is indirectly back propagated to adapt the weights of the action network. The error for the action network weight update is given by (2.41)

$$e_a(t) = J(t) - U_c(t) \tag{2.41}$$

The objective function for the action network is the square error of (2.41), and is calculated by (2.42).

$$E_a(t) = \frac{1}{2} e_a^2(t) \tag{2.42}$$

The weights of action network are also updated using gradient-based adaptation, as given in [36].

CHAPTER 3 PROCEDURES

Chapter 3 provides detailed procedures followed to achieve the objectives of this study. The procedures are mainly divided into two sections. The first section describes about the experimental implementation of current controlled voltage source inverter and existing VI. The second section describes the use of ADP in the outer loop of VI to make it adaptive and learn online. For experimental implementation of current controlled voltage source inverter and existing VI, all the controllers are implemented in PSIM software. In order to implement the ADP based VI, MATLAB/Simulink was used.

3.1 Design of three phase current controlled voltage source inverter

Three phase CC-VSI with LC filter was used in implementation of VI in the microgrid. Current controller of CC-VSI was used to control the current flowing between ESS and the microgrid, which ultimately controls the power flowing between the ESS and the microgrid system.

3.1.1 Design of LC filter

LC filter was designed with inverter switching frequency of 10 kHz (=62831.85 rad/s), cut off frequency of 1 kHz (=6283.185 rad/s) i.e. one decade below the switching frequency and damping ratio (ζ) of 0.707 [37]. The resistance of inductor (R), inductance (L) and capacitance (C) of LC were taken as 0.1Ω, 10 mH and 3.3 μF respectively [37].

3.1.2 Design of current controller transfer function

For current controller design, the transfer function of the plant (i.e. inverter with LC filter) was derived as

$$G(s) = \frac{i_L}{v_{inverter}} = \frac{\frac{1}{L}}{s + \frac{R}{L}} \tag{3.1}$$

where R, L and C are the resistance of inductor, inductance and capacitance of LC filter respectively. Replacing the values of R, L and C in (3.1) gave the transfer function of the plant as [37]

$$G(s) = \frac{i_L}{v_{inverter}} = \frac{100}{s + 10} \tag{3.2}$$

For current controller design, a modified PI (type 2) controller was used. The generic transfer function of the modified PI type 2 controller is

$$H_{PI2}(s) = K_{PI} \frac{1 + s\tau}{s\tau} \frac{1}{1 + sT_p} \tag{3.3}$$

where K_{PI} is the proportional gain, τ is the time constant of the controller and T_p is the time constant of the additional pole at high frequency used to attenuate higher frequency noises. These constants are labeled in the theoretical frequency response of a modified PI (type 2) controller as shown in Figure 3.1.

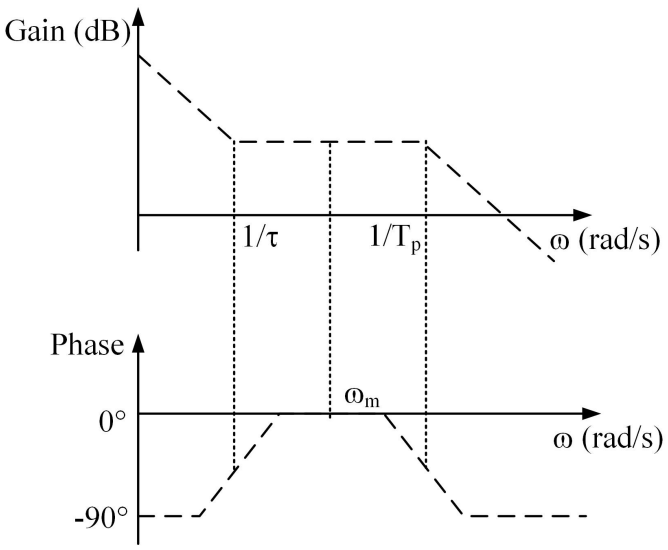

Figure 3.1. Asymptotic frequency response of a modified PI (type 2) controller.

The modified PI (type 2) controller in continuous time domain (i.e. in s-domain) was designed with a crossover frequency (bandwidth) of 1 kHz (=6283.185 rad/s) and phase margin of 45° [37]. The modified PI (type 2) controller designed with these specifications for the plant in (3.2) was derived in continuous time domain (s-domain) as [37]

$$H(s) = \frac{62.93s + 1.642 \times 10^5}{6.609 \times 10^{-5}s^2 + s} \tag{3.4}$$

3.1.3 Transformation of s-domain current controller to z-domain

The current controller derived in (3.4) from [37] was designed in continuous time domain (s-domain). Continuous time domain controllers can be implemented only in analog circuits in hardware. It can not be implemented in digital circuits, such as microcontrollers, because digital circuits operate in discrete time domain only. In the digital control implementation, the plant is preceded by a hold circuit (zero order hold) of the ADC channels microcontroller [38]. So the plant transfer function in the s-domain

preceded by the hold circuit also needs to be converted to the z-domain. Figure 3.2 shows the analog and digital closed loop control system of the CC-VSI.

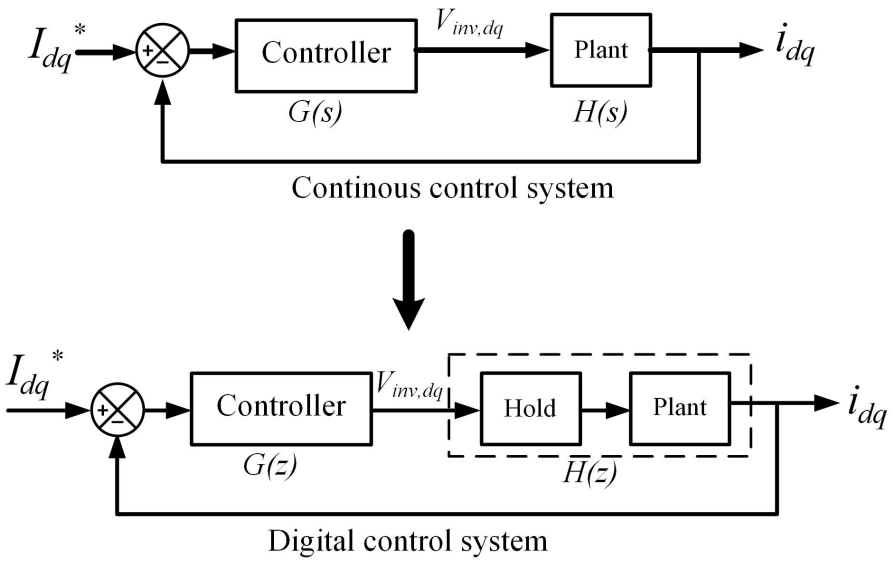

Figure 3.2. Analog and digital control system.

The s-domain transfer function of the plant and the current controller in (3.2) and (3.4) were transformed from continuous time domain (s domain) to discrete time domain (z-domain) using bilinear (Tustin) conversion method. It maps every point of the s-plane to the z-domain in $j\omega$ axis with $Re[s] = 0$, within the unit circle, $|z| = 1$. It preserves the stability and maps every point of the s-domain frequency response to corresponding z-domain frequency response [38]. When a Laplace transform is applied on discrete time signal with each corresponding element delayed by unit impulse, the result in z-domain

can be obtained by substitution of

$$z = e^{sT} \tag{3.5}$$

$$= \frac{e^{s\frac{T}{2}}}{e^{-s\frac{T}{2}}} \tag{3.6}$$

$$\approx \frac{1+sT/2}{1-sT/2} \tag{3.7}$$

where T is the sampling period. Similarly, the above bilinear approximation can be solved for s by approximating $s = (1/T)ln(z)$ as

$$s = \frac{1}{T}ln(z) = \frac{2}{T}\frac{z-1}{z+1} \tag{3.8}$$

Using bilinear approximation, the s-domain transfer can be converted into z-domain transfer function as

$$s \leftarrow \frac{2}{T}\frac{z-1}{z+1} \tag{3.9}$$

$$H_d(z) = H_a(s)\Big|_{s=\frac{2}{T}\frac{z-1}{z+1}} \tag{3.10}$$

$$= H_a\left(\frac{2}{T}\frac{z-1}{z+1}\right) \tag{3.11}$$

where $H_d(z)$ is the z-domain transfer function of s-domain transfer function $H_a(s)$.

The switching frequency for switching the inverter switches was taken as 10 kHz. As a rule of thumb, the sampling frequency for the feedback signals in a closed system should be ten times the bandwidth of the controller [38]. That's why, the sampling frequency for the measurement of the inverter current and the grid voltage was chosen as

10 kHz. Transforming the s-domain transfer function of current controller of (3.4) into z-domain transfer function with sampling frequency of 10 kHz (i.e. T = 100 μs) using equation 3.11 gives

$$H(z) = \frac{30.64 + 7.702z^{-1} - 23.56z^{-2}}{1 - 1.11385z^{-1} + 0.1385z^{-2}} \tag{3.12}$$

Similarly, transforming the s-domain transfer function of the plant of (3.2) into z-domain transfer function with sampling frequency of 10 kHz (i.e. T = 100 μs) using (3.11) gives

$$G(z) = \frac{0.004997 + 0.004997z^{-1}}{1 - 0.999z^{-1}} \tag{3.13}$$

Figure 3.3 shows the summary of the conversion of the transfer functions of the plant and the controller from s-domain to z-domain.

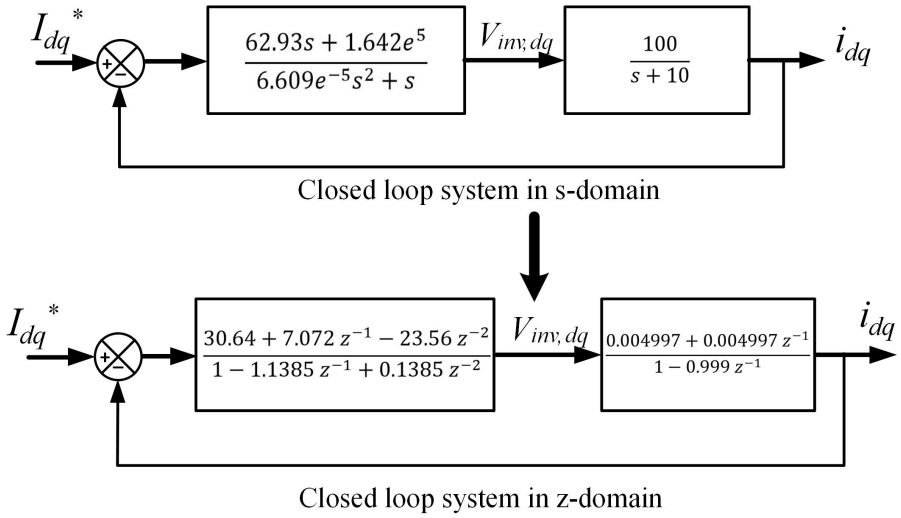

Figure 3.3. Transfer function of the plant and controller from s-domain to z-domain.

3.2 Implementation of current controller in PSIM simulation software

The z-domain current controller designed in Section 3.1.3 was implemented in hardware using PSIM as the interface software. Digital signal processor (DSP) from Texas

Instruments (TI) i.e. TMS320f28035 (i.e. TI2803) was used to load the current controller. The C code of the controller was generated automatically using PSIM which was later loaded into the RAM of the DSP by using Code Composer Studio software. Figure 3.4 the current controller, which was implemented in PSIM.

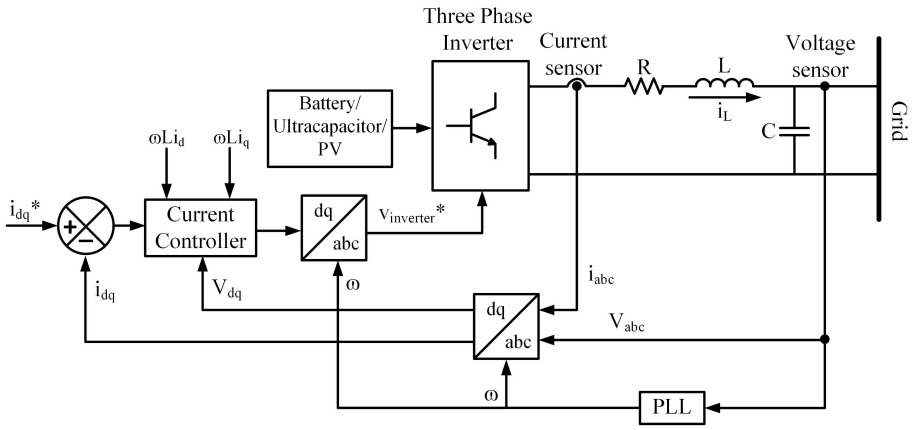

Figure 3.4. Block diagram of current controller implemented in PSIM.

The current of phase a and c from the current sensor circuit were fed to the analog to digital converter (ADC) pins of B4 and B6 respectively. The grid voltage of phase a and c from the voltage sensor circuit were fed to the ADC pins of A4 and A6 respectively. The current feedback from the inductor current and voltage feedback from the grid were transformed into dq frame using Park's transformation. The actual I_d current from the inverter was compared with the reference I_d current. The error was fed to the z-domain PI controller. The PI controller generated the required modulating signals for the inverter in dq frame, which was again transformed into abc frame using inverse Park's transformation. Thus, the inverter current was controlled.

Figure 3.5 shows the schematic diagram of the three phase inverter implemented in PSIM. The AC signals can not be given to microcontroller because the negative voltage

damages the microcontroller. So the current sensor and voltage sensor circuit were used to offset the actual inverter current and voltage by 1.6 V. The offset signals (i.e. pulsating dc signals) were then fed to the microcontroller. The offset and the gain of the circuits were removed later.

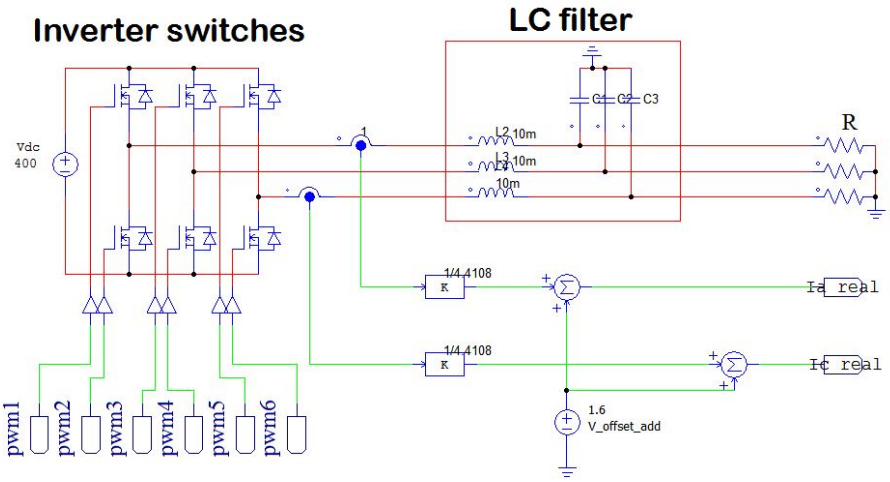

Figure 3.5. Schematic diagram of three phase inverter implemented in PSIM.

Figure 3.6 shows the schematic diagram of the current controller implemented in PSIM. The reference I_d current was given using serial communication interface (SCI) input block of PSIM. SCI enables to change those references in real time. A maximum limit of 4.5 was set to limit the power from the inverter in real system because the inverter and the protection system in hardware was designed with the limit of 1 kW. The z-domain PI controller designed earlier was implemented. The cross coupling terms and the grid voltage in dq frame were added as feedback signals. The output from the controller was transformed into abc domain using inverse Park's transformation. This output signal was then divided by the dc voltage magnitude to get the modulating signal for three phase PWM generator. The switching frequency of the carrier signals (triangular

waveforms, with minimum and maximum values of -1 and 1 respectively) in the PWM generator was set as 10 kHz. A limiter of minimum and maximum of +1 and -1 respectively was used to ensure that the inverter always operates in linear region.

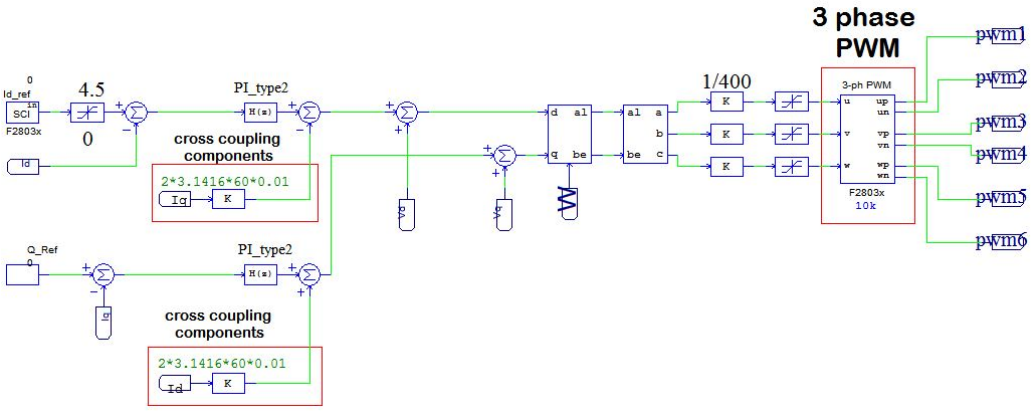

Figure 3.6. Schematic diagram of current controller in PSIM.

Figure 3.7 shows the schematic diagram of the PLL block implemented in PSIM. Considering a balanced system, grid voltage of phase a and c were transformed into the $\alpha\beta$ component using Clarke's transformation. The arc tangent of the ratio of β component to α component, as in (3.14), gave the phase angle (ω) information in pu which was converted to radian. The so calculated phase angle (ω) was used in Park's transformation which synchronized the inverter with the grid voltage.

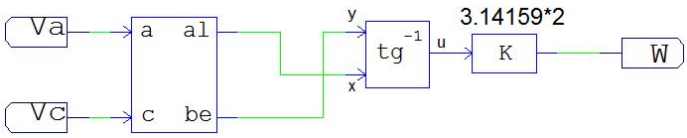

Figure 3.7. Schematic diagram of PLL implemented in PSIM.

$$\omega = tan^{-1}\left(\frac{V_\beta}{V_\alpha}\right) \tag{3.14}$$

Since only active power is to be controlled in VI, the reference I_q current was set to zero. In order to test the current controller, the reference I_d was changed from 2 A to 3 A at 0.5 s for both the simulation and in hardware in PSIM.

3.3 Design of virtual inertia

The current controller developed in section 3.2 was used to control the power from the inverter to emulate VI in a microgrid system as shown in Figure 3.8.

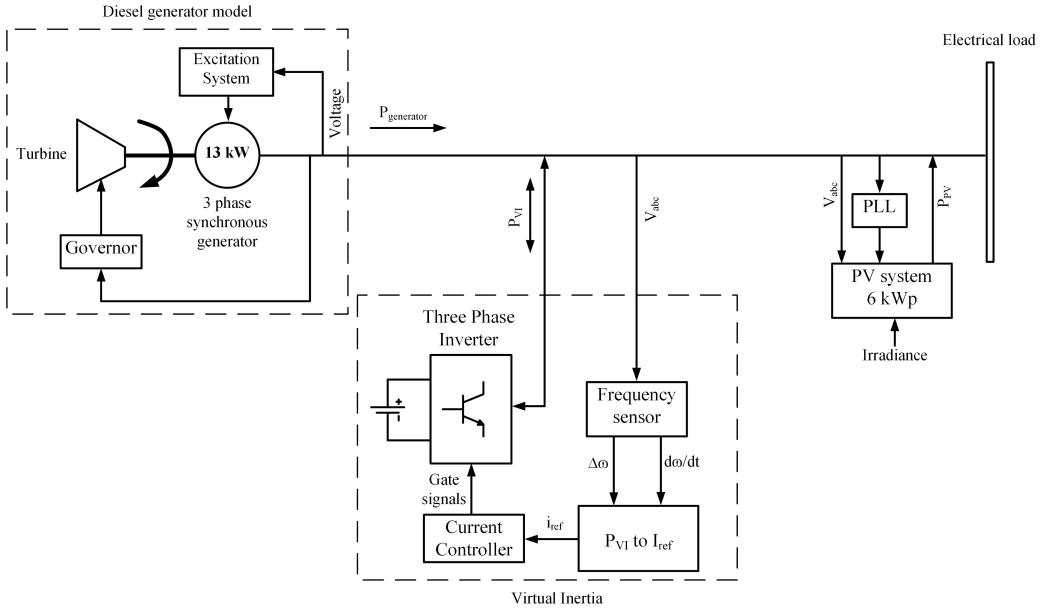

Figure 3.8. Schematic diagram of experimental setup of a microgrid system with VI.

The maximum ROCOF $\left(\frac{d\Delta f}{dt}\right)_{max}$ in the system was assumed to be ± 2 Hz/s and the maximum frequency deviation from nominal frequency $(\Delta f)_{max}$ was assumed to be ± 2.5 Hz in the experiment. The inertia coefficient and damping coefficient for VI are calculated as

$$K_I = \frac{P_{VI}}{\left(\frac{d\Delta f}{dt}\right)_{max}} = \frac{1000W}{2Hz/s} = 500\,Ws/Hz \tag{3.15}$$

$$K_D = \frac{P_{VI}}{(\Delta f)_{max}} = \frac{1000W}{2.5Hz} = 400\,W/Hz \tag{3.16}$$

where P_{VI} is the maximum power rating of VI, $\left(\frac{d\Delta f}{dt}\right)_{max}$ is the maximum possible ROCOF of the system and $(\Delta f)_{max}$ is the maximum possible change in frequency from nominal value.

So the values of inertia coefficient, K_I and damping coefficient, K_D were taken as 500 Ws/Hz and 400 W/Hz, respectively in the experiment. But for simulation purpose in MATLAB/Simulink for ADP based VI, the inertia coefficient and damping coefficient were taken as 500 Ws/Hz and 2000 W/Hz, respectively, considering the power rating of inverter was 2500W. If the inertia coefficient is too low, then the VI may not provide enough inertial response and if it is high, then the reference inertial power may be fluctuating even for a small change in system. High fluctuations may lead to instability. So there should be a compromise between inertia response and stability for choosing the inertia coefficient. That's why, the inertia constant was taken as 500 Ws/Hz, regardless or more power rating of the inverter.

3.3.1 Implementation of virtual inertia in PSIM

The frequency of the system was measured with a frequency sensor circuit using LM2907 (frequency to voltage converter integrated circuit (IC)) [39]. The output of the frequency sensor was fed to the ADC pin (B7) of the microcontroller, which was multiplied by the gain of the circuit to retrieve the frequency of the system. There frequency oscillation of about ± 0.3 Hz in the system. It might be due to the effect of noise in the frequency measurement circuit or due to high frequency component in the generator's voltage. In order to avoid the effect of frequency oscillation on unnecessary triggering of inverter of VI, the deadband frequency of ± 0.3 Hz was taken in the system.

The deadband in the frequency was implemented in a simplified C block of PSIM as shown in Figure 3.9.

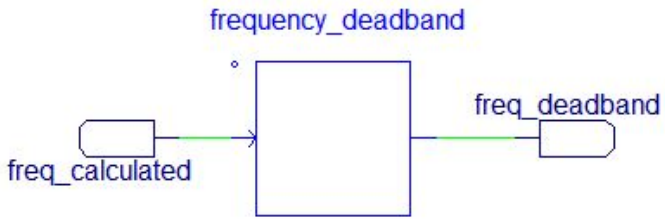

Figure 3.9. Simplified C block in PSIM for deadband implementation of frequency.

C code in IQ math format was written in the simplified C block as shown in Figure 3.10.

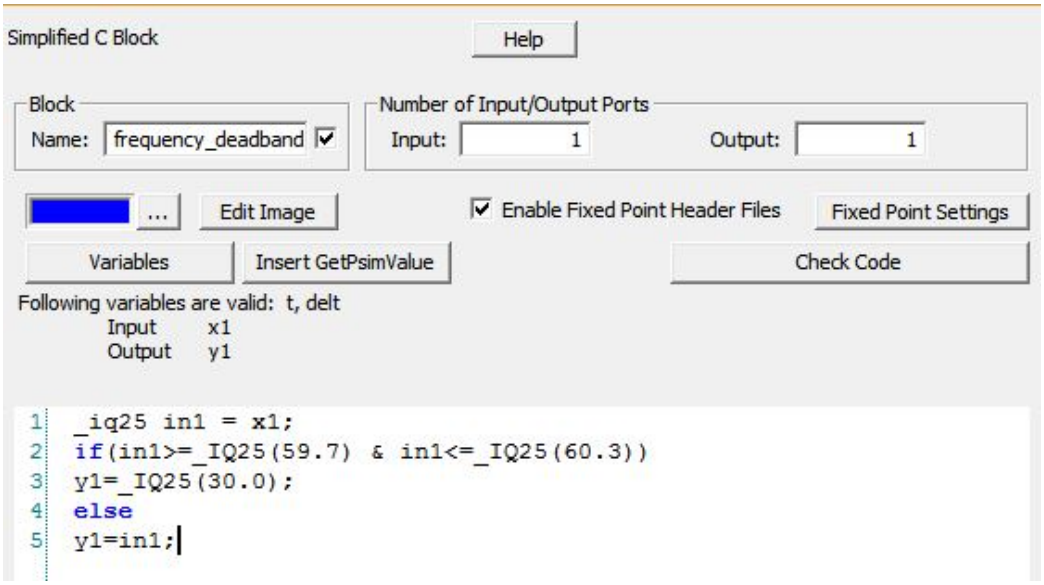

Figure 3.10. C code for deadband implementation of frequency.

Similarly, the ROCOF of the system was calculated by taking the derivative of the frequency of the system with respect to time as shown in Figure 3.11.

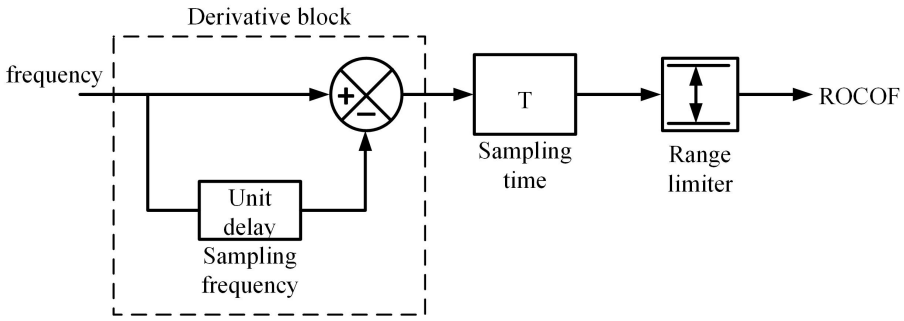

Figure 3.11. Calculation of ROCOF of the system.

The digital derivative block of PSIM had a bug, so the derivative of the frequency was taken by dividing the difference in frequency at a certain time interval to the time interval of sampling as shown in Figure 3.11. The derivative of the frequency of the system is calculated using (3.17)

$$ROCOF(n) = \frac{f(n) - f(n-1)}{T} \tag{3.17}$$

where $ROCOF(n)$ is the rate of change of frequency at the current time step, $f(n)$ is the input frequency at the current time step, $f(n-1)$ is the input frequency at one time step delay and T is the sampling time.

The ROCOF of the system was calculated using (3.17) in PSIM, as shown in Figure 3.12. A digital low pass filter (LPF) with the cut off frequency of 15 Hz, was used to filter low frequency noise in the system. The bandwidth for ROCOF calculation was 30 Hz, so the frequency signal was delayed with unit delay time of 33.33 ms. A range limiter of ± 10 Hz/s was taken to limit the maximum and minimum ROCOF values during measurement.

Similar to the deadband in frequency measurement, the deadband was implemented for ROCOF measurement, too, to avoid triggering of the inverter of VI due to noises using

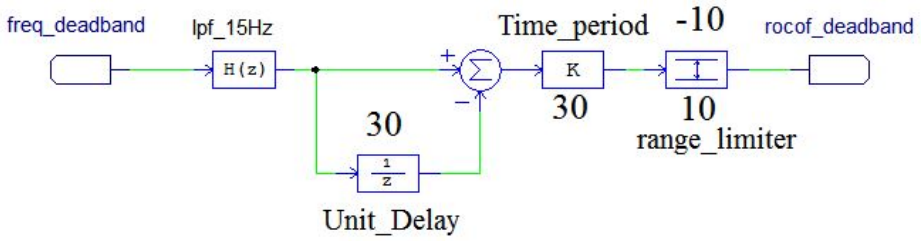

Figure 3.12. ROCOF calculation implemented in PSIM.

simplified C block in PSIM, as shown in Figure 3.13.

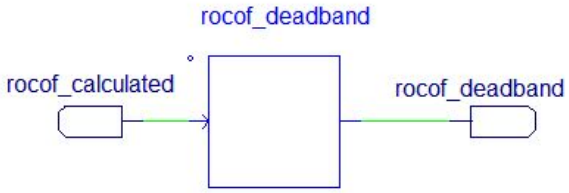

Figure 3.13. Simplified C block in PSIM for deadband implementation of ROCOF.

The ROCOF deadband of ±0.3 Hz/s was implemented, as shown in the code written in C block in IQ math format in Figure 3.14 [40].

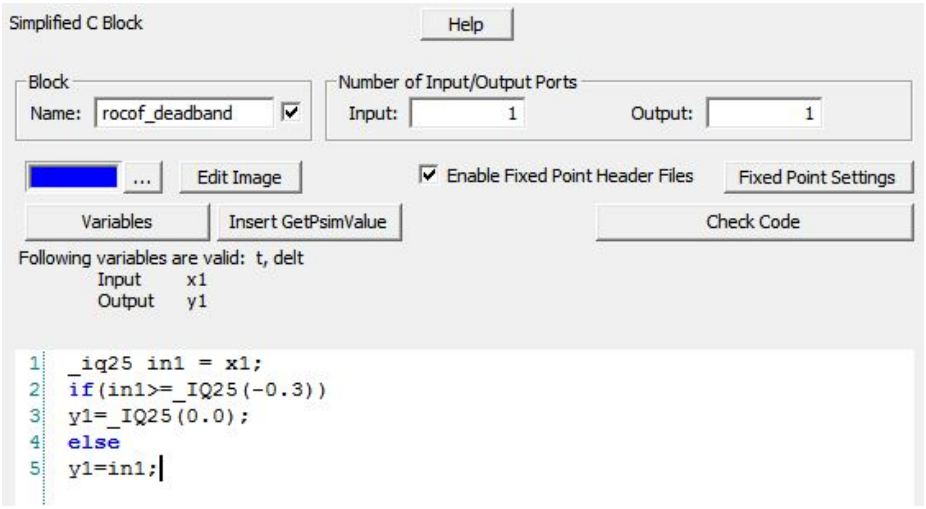

Figure 3.14. C code for deadband implementation of ROCOF.

The so calculated frequency and ROCOF with deadband were multiplied by the damping coefficient and inertia coefficient respectively and added to calculate the

reference VI power, as shown in Figure 3.15.

The so calculated reference VI power was converted into reference I_d current as shown in Figure 3.16.

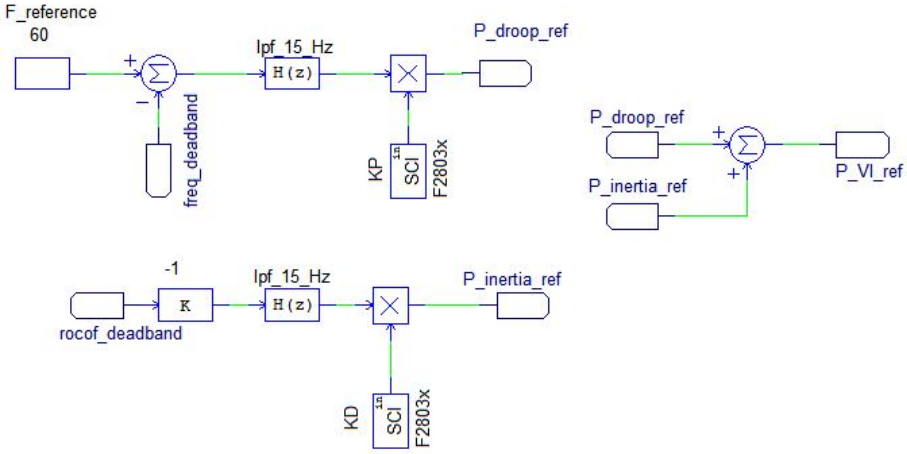

Figure 3.15. Reference VI power calculated in PSIM.

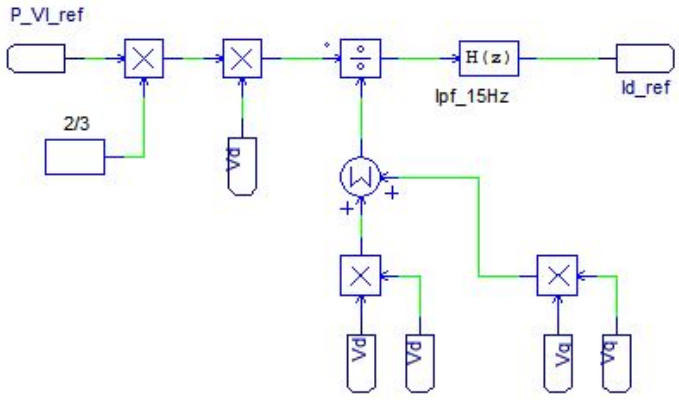

Figure 3.16. Reference I_d current calculated from reference VI power in PSIM.

3.3.2 Hardware implementation of virtual inertia

Figure 3.17 shows the experimental setup of VI. A DSP TI2803 was used as the main controller [41]. It was directly connected to the DSP scope of PSIM from a serial communication port. Using the current and voltage sensor circuit, the inverter current and

grid voltage of each phase were offset and scaled to fit them within the ADC range of 0 V-3 V of the DSP. The so obtained voltage and current were sent to the DSP. The frequency sensor circuit measured the frequency of the system using a frequency to DC voltage converter IC (i.e. LM2907). The values of frequency, inverter current and grid voltage were evaluated inside the DSP after removing the scaling and the offset. The z-domain PI controller, explained earlier was embedded inside the DSP to control the inverter current. The current controller generated the required three phase PWM for the inverter based upon the reference VI power and equivalent reference I_d current as explained earlier. The PWM signals were sent to the gate driver circuit which electrically isolates the low voltage DSP from the high voltage side of the IGBT switches inside the semikron switch. The gate driver circuit voltage required to drive the IGBT switches. A LC filter was connected in the output of the inverter to filter the high frequency noises= that appear due to the switching of the inverter. A DC power supply was used in the DC side voltage for the inverter.

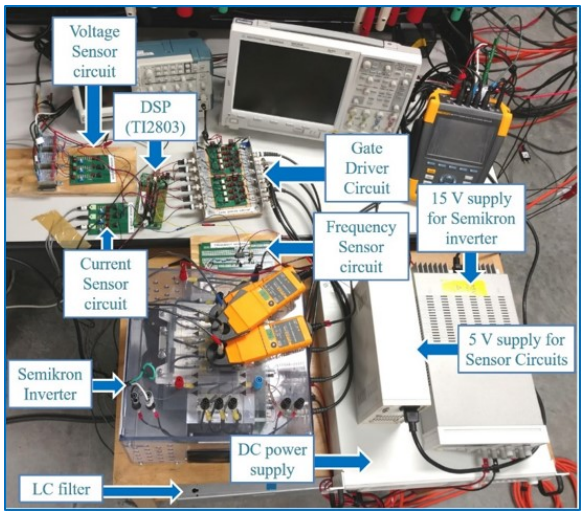

Figure 3.17. Hardware setup of VI.

3.4 Design of neural network structure of adaptive dynamic programming

In this thesis, the control algorithm of ADP has been adopted from [42]. In [42], ADP was designed to improve the dynamics of grid connected current controller. However, the ADP controller in this thesis, was used to improve the dynamics of outer control loop of VI. The reinforcement signal in this thesis, was designed to bring the frequency of the system to nominal frequency faster.

The neural network designed for ADP in this thesis was a multilayer perceptron. It has two network structures: the action network and the critic network. The neural network structure of the action network is 3-6-1 structure as shown in Figure 3.18. X_1, X_2 and X_3 are the difference in frequency from nominal frequency at current time step, at one time step delay and two time step delay respectively. There are 6 hidden nodes from N_1 to N_6 and one output node u. The output of the action network, u is the reference VI power, which is added to the reference VI power given by existing outer control loop of VI.

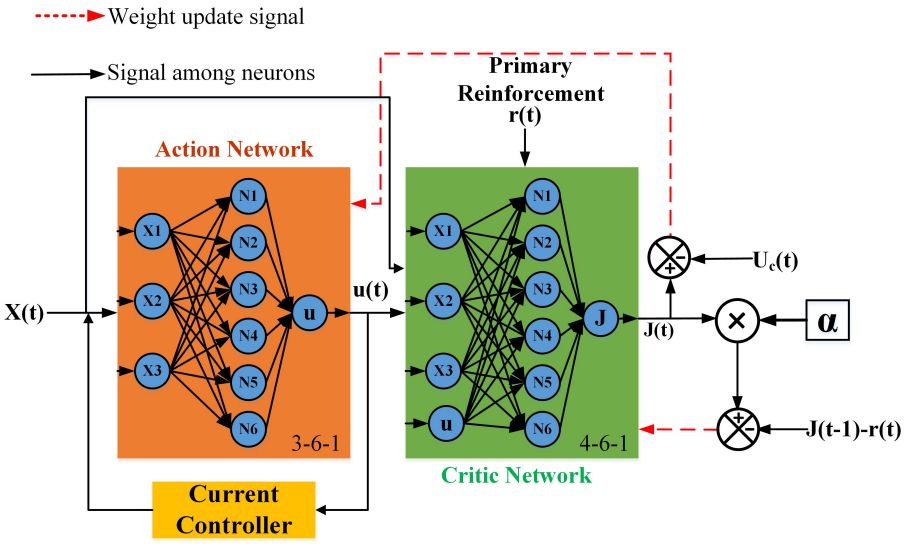

Figure 3.18. Architecture of ADP implemented for VI [33].

The neural network structure of the critic network is 4-6-1 structure, as shown in Figure 3.18. X_1, X_2 and X_3 are the difference in frequency from nominal frequency at current time step, at one time step delay and two time step delay respectively and u was the output of the action network. There are 6 hidden nodes from N_1 to N_6 and one output node u. The output of the critic network, J updated the weights of action network online and made it adaptive.

3.4.1 Development of objective function for for adaptive dynamic programming

For the objective function of reinforcement signal in (2.13), the value of $-c$ was taken as -1, so whenever there was difference in frequency and nominal frequency (X_1, X_2 and X_3), the value of reinforcement signal became highly negative. Therefore, gains of the action network were adjusted accordingly. On the other hand, when the frequency of the system was equal to nominal frequency, i.e. X_1, X_2 and X_3 are zero, then the reinforcement signals became zero and no adjustments were made to the weights fo action network. The values of a_1, a_2 and a_3 in (2.13) were taken as 0.4, 0.3 and 0.3 respectively.

3.5 Implementation of ADP based virtual inertia in MATLAB/Simulink

3-phase PLL block of MATLAB/Simulink was used to measure the frequency. The ROCOF of the system was measured by taking the derivative of frequency with a LPF of cut off frequency of 30 Hz. A frequency deadband of ± 0.2 Hz and ROCOF deadband of ± 0.2 Hz/s was taken. The deadband values in simulation was taken smaller than in PSIM because the generator system was ideal in MATLAB/Simulink in simulation.

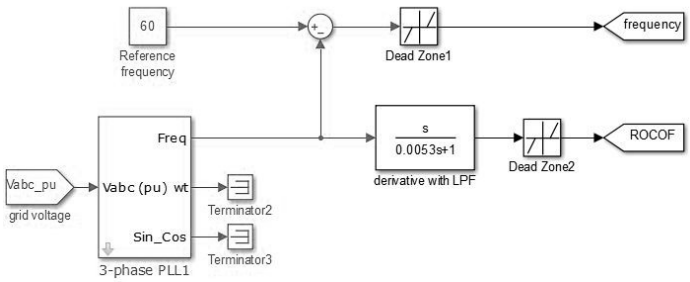

Figure 3.19. Frequency and ROCOF measurement in MATLAB/Simulink.

For the generation of reference VI power with ADP, the error in frequency at current time step, one time delayed feedback and two time delayed feedback were given to ADP as shown in Figure 3.20.

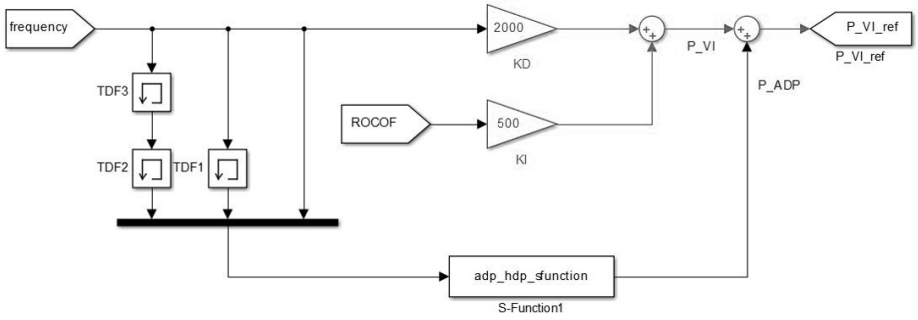

Figure 3.20. ADP based VI implementation in MATLAB/Simulink to generate reference VI power.

The simulation time step taken was 5 μs, so the time delay for one time and two time delayed feedback signal of frequency were 5 μs and 10 μs respectively. The code of ADP was written in s-function block of MATLAB/Simulink. The initial weights of critic and action network were randomly initialized in the range of $[-0.1,\ 0.1]$. At first, the inputs were normalized and outputs were amplified assuming the input frequency could vary in the range of 0 to 10 Hz. Then, the neural networks were trained offline with parameters set as in [42]. Simulations were repeated to train the neural network until the

outer loop of the VI was made faster and the frequency of the system returned to nominal frequency faster. The final trained weights were used for simulations.

3.6 Development of PV-diesel generator microgrid system

For dynamic stability analysis with existing VI in experiment, only the diesel generator with a load was taken. Besides for dynamic frequency stability of ADP based VI in simulation, PV-diesel generator microgrid test benchmark was used. A 13 kW diesel generator model was developed in MATLAB/Simulink for the simulation of the system. For the experiment, a 13 kW generator (Kohler 15REYG) available in the Microgrid Laboratory in South Dakota State University (SDSU) was used. A 6 kWp PV system was used for simulation of ADP based VI.

3.6.1 13 kW diesel generator system

Figure 3.21 shows the block diagram of a three phase generator implemented in MATLAB/Simulink. Figure 3.22 shows the model of 13 kW diesel generator implemented in MATLAB/Simulink. The inertia constant of the generator was taken as 2 s. The other parameters of the generator were taken from [37].

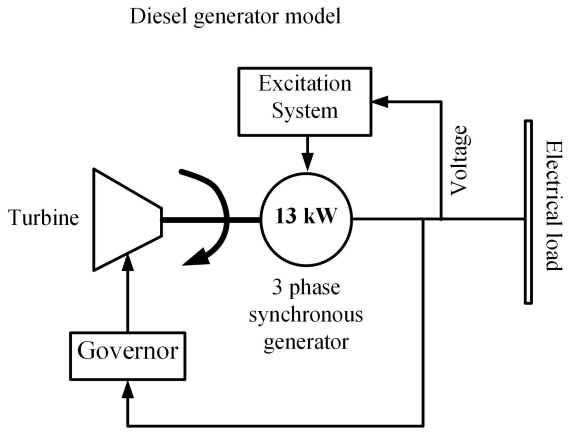

Figure 3.21. Block diagram of a diesel generator implemented in MATLAB/Simulink.

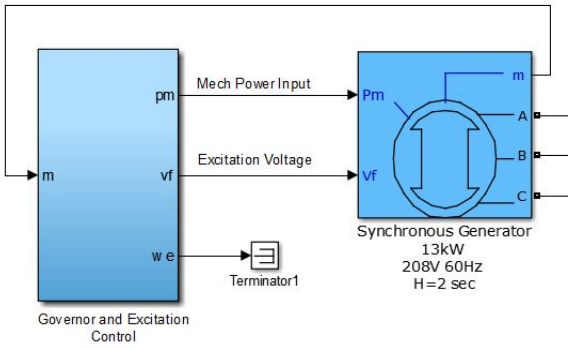

Figure 3.22. Model of 13 kW diesel generator implemented in MATLAB/Simulink.

3.6.2 6 kWp PV system

Figure 3.23 shows the block diagram of a three phase PV system implemented in MATLAB/Simulink. Figure 3.24 shows the model of of a three phase 6 kWp PV system implemented in MATLAB/Simulink. The percent irradiance data was the input for the PV system. PV system was assumed to be a sinusoidal current source whose current was synchronized with the grid voltage by using PLL. The detailed design of the PV system is given in [37].

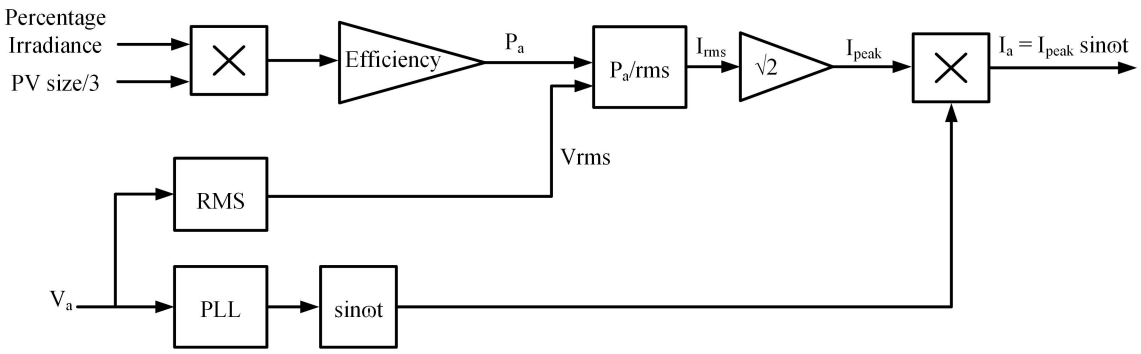

Figure 3.23. Block diagram of a PV system implemented in MATLAB/Simulink.

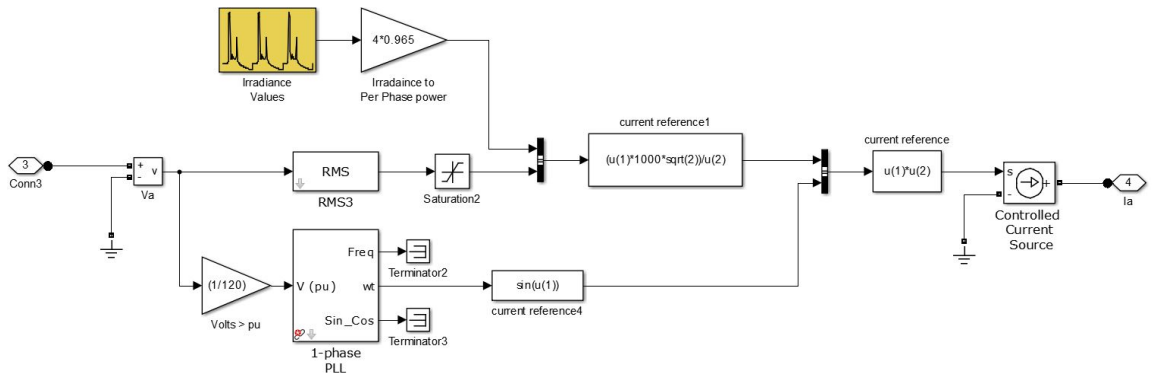

Figure 3.24. Model of 4 kWp PV system implemented in MATLAB/Simulink.

3.6.3 Sizing the battery capacity

The battery was supposed to be a part of the microgrid system, that has a wide range of applications as explained earlier. The average load considered in this system was 7.5 kW. The battery size was assumed to be capable to supply the average load for four hours similar to [19]. Taking the efficiency of 90% for the ESS, the size of the battery (Q) for this system was taken as 50 kWhr. By dividing the total kWhr size of the battery by the DC voltage of 400 V, the Ah rating of the battery was calculated as 125 Ah. According to [29], the total battery lifetime (effective lifetime) was $390 \times 125\ Ah$ (i.e. = $48750\ Ah$).

3.6.4 Experimental test setup of a microgrid with diesel generator and load for VI

Figure 3.17 shows the experimental setup of a microgrid with a 13 kW generator, virtual inertia hardware and a load. The generator, VI hardware and load were all connected to a common bus, termed as the point of common coupling (PCC) .

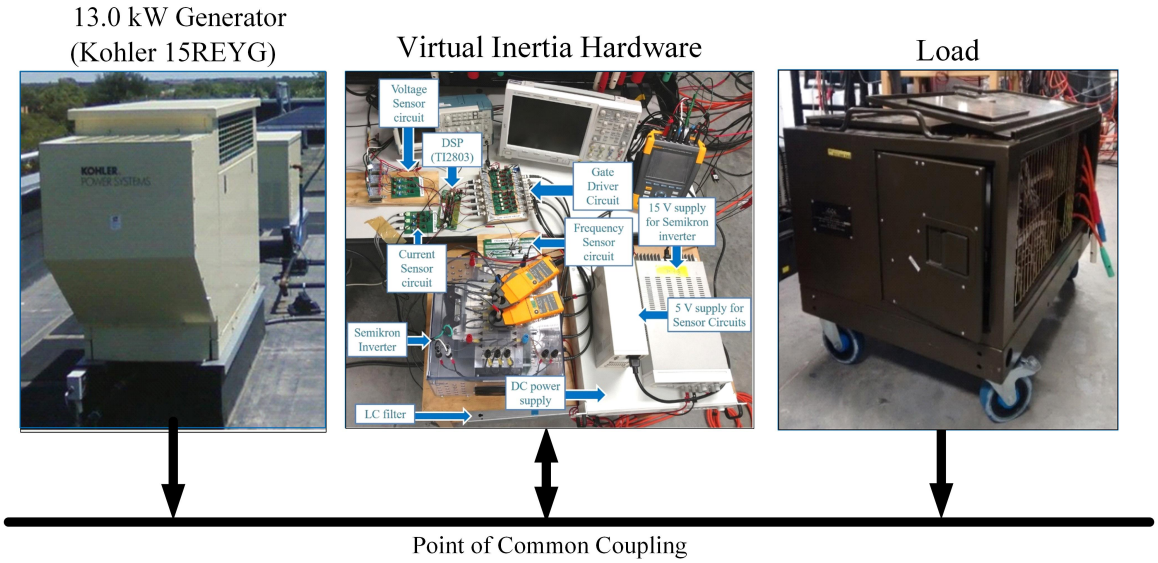

Figure 3.25. Experimental setup of microgrid with diesel generator, VI and load.

For the dynamic frequency stability analysis, the load was changed from 6 kW to 9 kW at 5 s. The frequency response of the system with and without VI was observed and logged using power quality meter (Fluke 435 series II).

3.6.5 Simulation test benchmark of a microgrid with diesel generator, PV system and load for ADP based VI

For the dynamic frequency stability analysis of ADP based VI, a microgrid system with 13 kW diesel generator, 4 kWp PV system and load was used, as shown in Figure 3.8. The PV system, ADP based VI, diesel generator and load were connected to the same bus. There were two test case studies conducted for the dynamic frequency stability analysis: a) step change in load with no PV system and b) PV system with real irradiance input.

(a) Case study I:

For case study I, the 3 phase load was changed from 6 kW to 9 kW at 5 s and again changed from 9 kW to 6 kW at 55 s, as shown in Figure 3.26. The frequency

response without VI, with VI and ADP based VI were observed and analyzed.

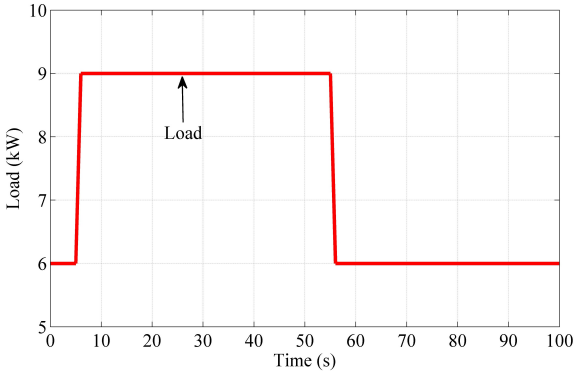

Figure 3.26. Step changes in load for case study I.

(b) Case study II:

For case study II, the load in the system was taken constant as 6 kW. 200 s snap shot of irradiance data taken for June 19, 2012 for Brookings, SD from the Microgrid laboratory in SDSU, as shown in Figure 3.27, was input to the PV system. The frequency response without VI, with VI and ADP based VI were observed and analyzed.

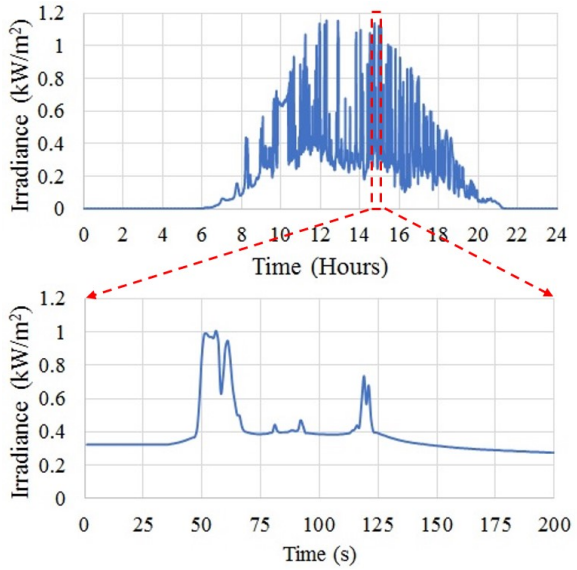

Figure 3.27. Snapshot of 200 s irradiance data of Brookings, SD of June 19, 2012 input to PV system for test case study II.

CHAPTER 4 RESULTS AND ANALYSIS

Chapter 4 presents both the simulation and hardware results and analysis from the z-domain current controller implemented in PSIM. The simulation results and analysis of the s-domain current controller in MATLAB/Simulink has been reported in [37]. The simulation results of MATLAB/Simulink and experimental results of frequency response of the microgrid with and without VI in the microgrid with a diesel generator and load is also presented. The simulation results and analysis of frequency response of the microgrid system without VI, with VI and ADP based VI is also presented. The speed response of the VI and ADP based VI along with the net energy exchanged were analyzed. The effect of discharging the battery in VI and ADP based VI on the lifetime of the lead acid battery has been compared and included.

4.1 Current controlled three phase voltage source inverter

The current controller designed in Chapter 3 was implemented in PSIM and in MATLAB/Simulink for VI. The current controller performance and stability was tested with step response in closed loop transfer function and step change in reference I_d current.

4.1.1 Step response of current controller in s-domain and z-domain

In order to evaluate the transient and steady state performance of the current controller developed in the s-domain and z-domain, the step response of the closed loop transfer function (controller and plant) in both the s-domain and z-domain was performed. Figure 4.1 shows the step response of the closed loop system in both the s-domain and z-domain.

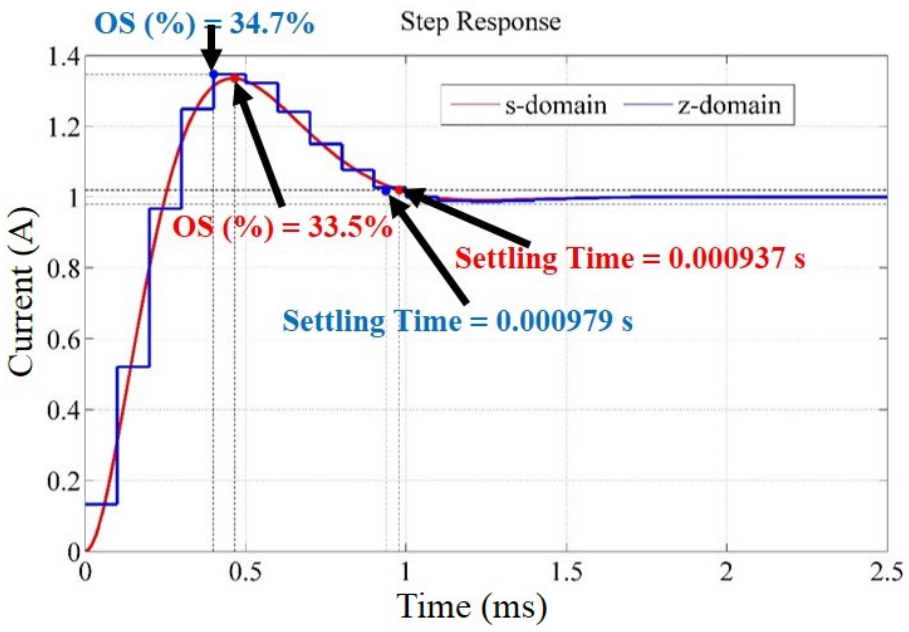

Figure 4.1. Step response of closed loop system in s-domain and z-domain.

The overshoot in s-domain and z-domain closed loop system were 33.5% and 34.7% respectively. Moreover, the settling time in s-domain and z-domain closed loop system were 937μs and 979 μs respectively. It can be seen that the stability of the current controller, while transforming from s-domain to z-domain was preserved.

4.1.2 PSIM simulation results of z-domain current controller for three phase inverter

In order to test the z-domain current controller performance, step change in reference I_d current was given from 2 A (i.e. 1.17 A rms) to 3 A (i.e. 1.73 A rms) at 0.5 s keeping the reference I_q current as zero. Figure 4.2 shows the three phase inverter current with step change in reference I_d current.

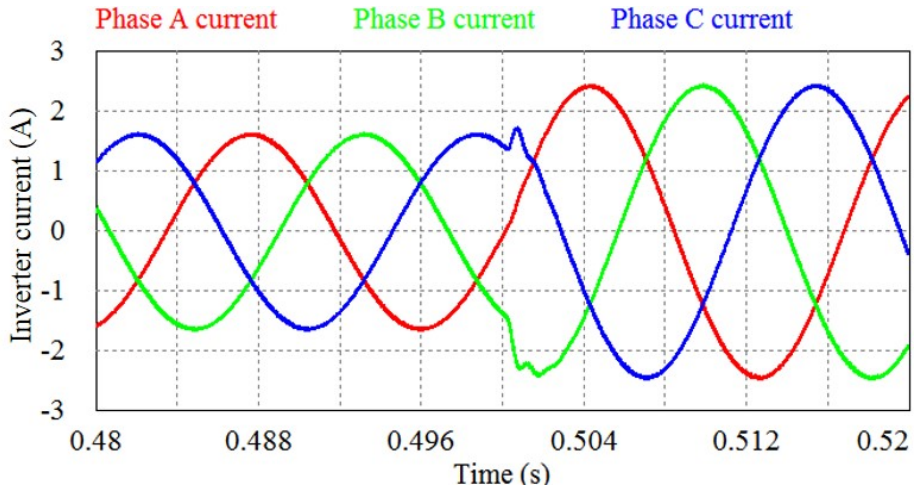

Figure 4.2. PSIM simulation result of three phase inverter current.

In PSIM, the relation between the reference I_d current and actual rms current of the inverter is given by

$$I_{reference}(rms) = \frac{I_{d\_reference}}{\sqrt{3}} \tag{4.1}$$

The inverter rms current with reference I_d equal to 2 and 3 were 1.2 A and 1.8 A, respectively, which is almost equal to the reference rms current given by (4.1).

Figure 4.3 shows the phase a inverter current and grid voltage. The grid voltage was scaled by a factor of 1/30. For VI, only the active power needs to be controlled, so the reference I_q current was set as zero. The inverter current was in phase with grid voltage. The power factor of the inverter current was 0.99. It can be observed that the inverter current was in phase with grid voltage even after a perturbation in reference I_d current. Therefore, it is verified that the z-domain current controller was working well in the PSIM simulation.

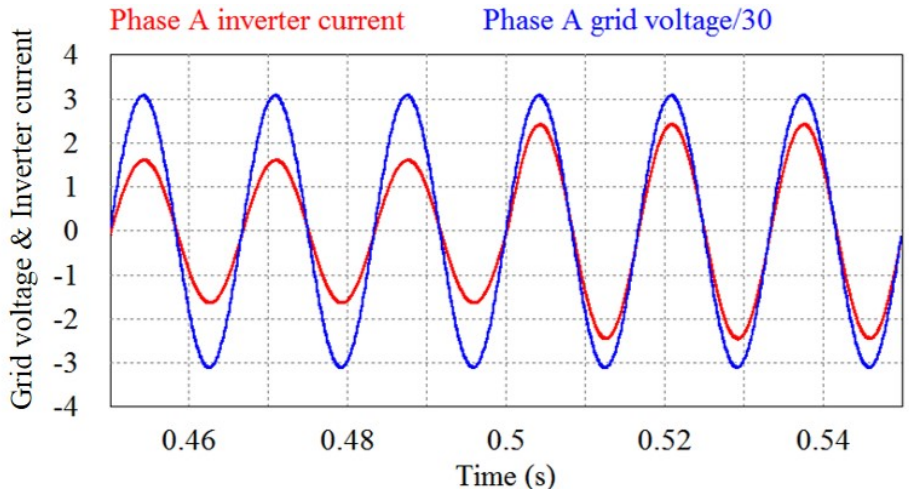

Figure 4.3. PSIM simulation result of phase a grid voltage and inverter current.

4.1.3 Experimental results of z-domain current controller for three phase inverter

The current controller connected to the inverter with a 1 kW load was tested in the experimental setup, which was explained earlier in chapter 3. The PLL for the current current was measured from the 13 kW generator. In order to test the current controller in experiment, the reference I_d current was changed from 2 A (i.e. 1.17 A rms) to 3 A (i.e. 1.73 A rms) at 2 s. Figure 4.4 shows the experimental result of the generator's phase a voltage and inverter's current observed in oscilloscope from Agilent technologies (MSO7034B). Red curve shows the inverter current measured from Agilent (1146A) current sensor. Green curve shows the generator's voltage. The generator voltage was not perfectly sinusoidal, and it had a THD about 5.1% of fundamental frequency. The inverter rms current was 1.17 A and 1.73 A when the reference I_d current was 2 A and 3 A respectively, which is almost equal to the reference current given by (4.1). The power factor of inverter current for both the references was about 0.99. Moreover, when the reference I_d current was 2 A and 3 A, the THD of the inverter current was 2.2% and 1.6%

of fundamental frequency respectively. The THD was lower at higher reference current compared to lower reference current, because at higher reference current, the current controller generates higher modulating signal of higher amplitude modulation and vice versa. There is negative correlation between the amplitude modulation and the THD. Moreover, due to more power flowing from the inverter, the LC filter would have more filtering, too, compared to low power flowing from it.

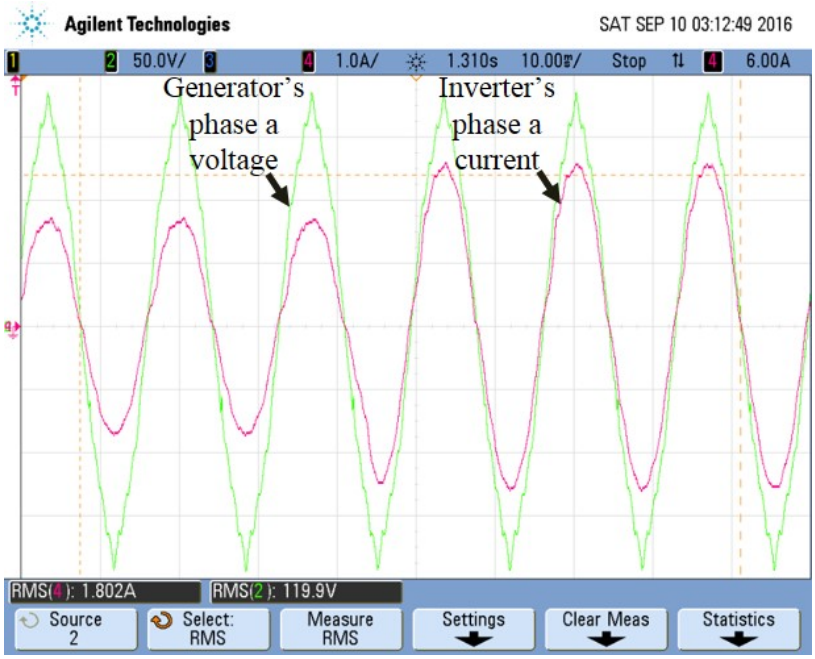

Figure 4.4. Experimental result of phase a generator voltage and inverter current.

4.2 MATLAB/Simulink simulation results of frequency response of microgrid with and without VI

For the performance analysis of VI, the frequency response of a microgrid system with and without VI, as simulated in MATLAB/Simulink. Figure 4.5 shows the frequency response of the microgrid system with a generator and a load with step change in load, as explained earlier in Chapter 3. The minimum and maximum frequency of the system

without VI (blue curve) were 56.02 Hz and 63.54 Hz respectively, which are out of the ISO 8528-5 standard limits. After the addition of VI, the minimum and maximum frequency of the system (red curve) were 58.81 Hz and 61.23 Hz respectively.

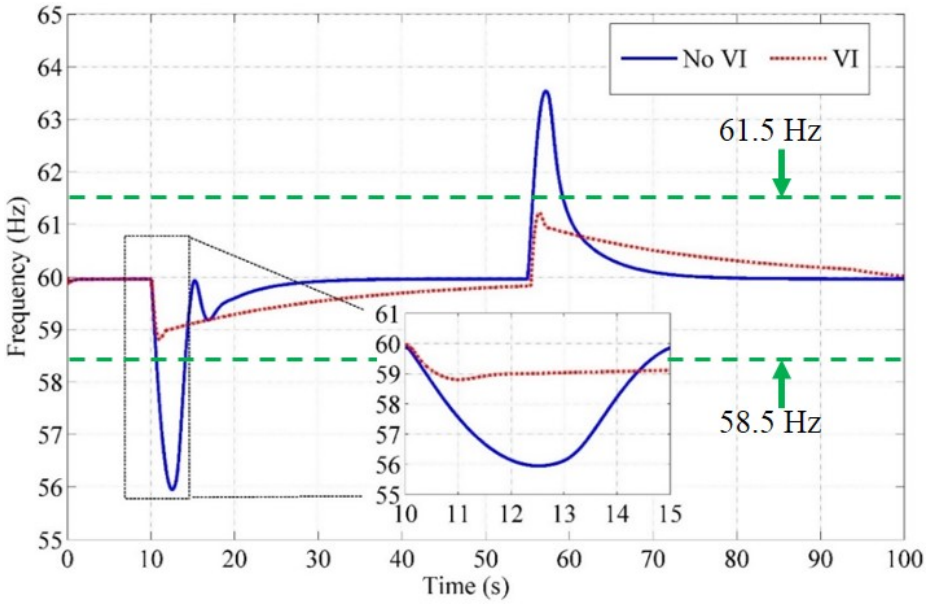

Figure 4.5. Simulation result of frequency with and without VI.

Figure 4.6 shows the power delivered by VI during the transients to improve dynamic stability. The maximum and minimum power delivered by the inverter were 2184 W and -2235 W respectively. The net energy exchanged was 1.6 Wh.

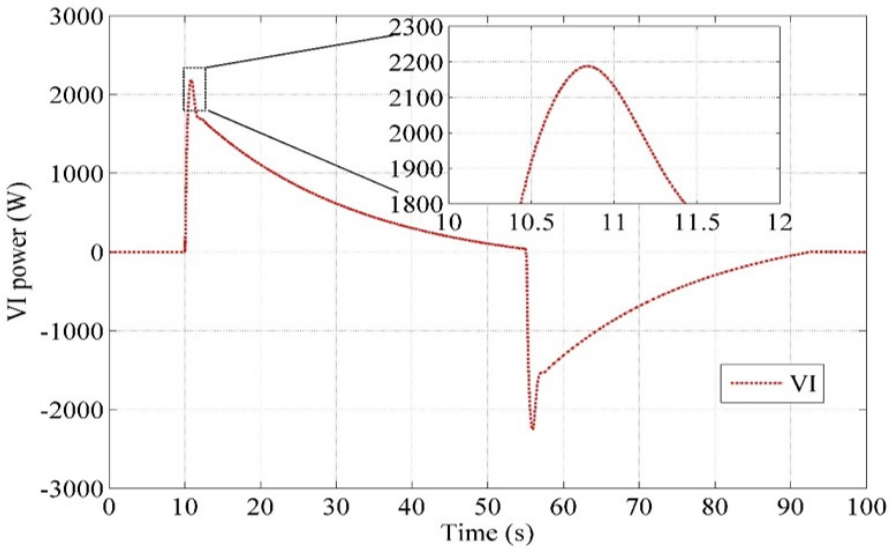

Figure 4.6. Simulation result of power delivered by inverter of VI.

Table 4.1 shows the summary of the main results power and energy delivered from the inverter.

Table 4.1. Performance comparison of the system with and without VI

Parameter	No VI	VI
$Power_{max}$ (W)	0	2184
Settling time (s)	12.61	35.16
Peak time (s)	2.51	1.1
$Power_{min}$ (W)	0	-2235
Settling time (s)	11.12 s	29.19 s
Peak time (s)	2.14	1.26
Net energy Exchanged (Wh)	0	1.6

4.3 Experimental results of frequency response of microgrid with and without VI

The frequency response of the microgrid system with a 13 kW generator and a load as explained earlier in Section 3.6.3 in Chapter was implemented to evaluate the performance of VI. The load was changed form 6 kW to 9 kW. Figure 4.7 shows the frequency response of the system with and without VI. The frequency response was

logged and observed from power quality meter (Fluke 435 series II) with a data logging resolution of 0.25 s. The red curve shows the frequency of the system without VI and blue curve shows the frequency response of the system with VI added to it.

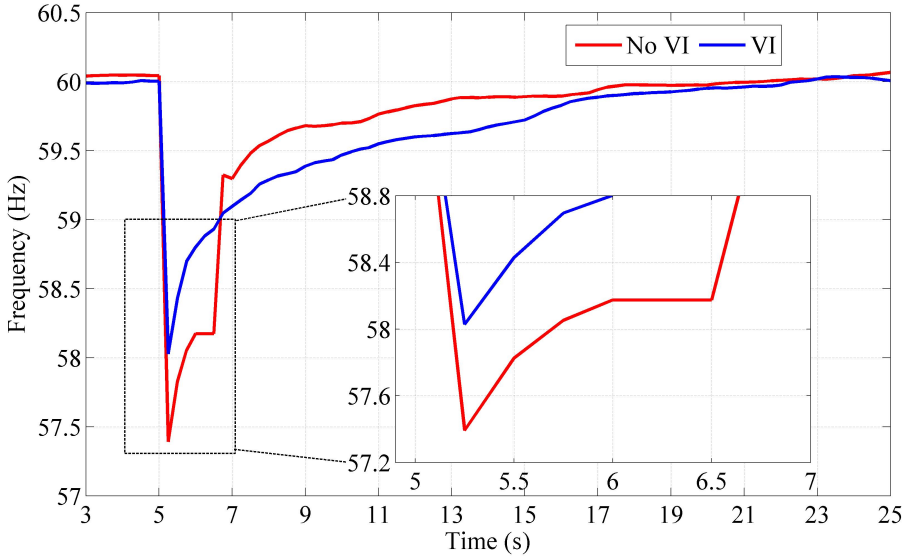

Figure 4.7. Experimental result of frequency response of system with and without VI.

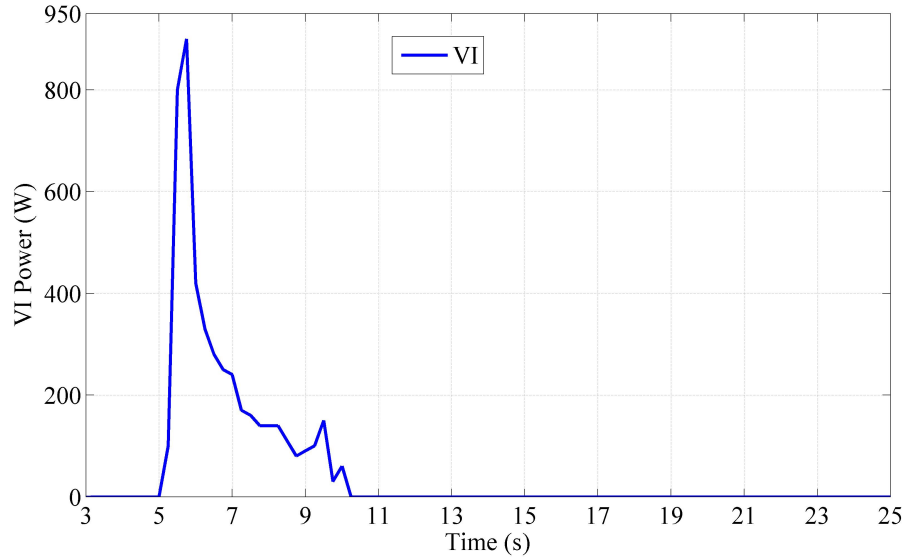

Figure 4.8. Experimental result of active power delivered by VI.

Figure 4.8 shows the active power delivered by VI. The maximum power delivered

was 900 W. The power was delivered only during the transient and once the transient damped, power injected by VI became zero.

The minimum frequency without VI was 57.39 Hz whereas the minimum frequency with VI was 58.03 Hz. The frequency response improved by 0.64 Hz. The frequency of the system with VI was not within ISO 85238-5 standard limits with compared to the simulation results because the maximum power that was delivered by inverter in experiment was 900 W as shown in Figure 4.8. But in simulation, the maximum power delivered by VI was more than 2 kW as shown in Figure 4.6. This is because the inverter in hardware was designed for 1 kW power rating. If the inverter could have injected more power then the frequency response of the system could have come within the ISO 85238-5 standard limits. The experimental results proves the concept of VI and its effect in improving the frequency response of the system.

4.4 MATLAB/Simulink simulation results of frequency response of microgrid without VI, with VI and ADP based VI

For performance evalutaion of VI and ADP based VI, simulation was done with two test case studies. For first test case study (i.e. case study I), a three phase resistive load was connected to the microgrid. For performance evaluation, a step change in load from 6 kW to 9 kW at 5 s and again step change in load from 9 kW to 6 kW at 55 s was used. For second test case study (i.e. case study II), a 4 kWp PV system was connected to the microgrid with load of 6 kW and 13 kW generator. 200 s irradiance data (with sampling period of 1 s) obtained from SDSU microgrids laboratory from June 19, 2012 was used for the PV system.

4.5 Simulation results of case study I

Figure 4.9 shows the frequency response of the system with VI, ADP based VI, and no VI for case study I. Without VI, the minimum frequency of the system during increment of 3 kW step load was 56.02 Hz which is below the ISO 8528-5 standard limits. With VI, the minimum frequency of the system was about 58.81 Hz. With ADP based VI, the minimum frequency of the system was about 58.52 Hz. Without VI, the maximum frequency of the system during decrement of 3 kW step load was 63.54 Hz which is above the ISO 8528-5 standard limits. With VI, the maximum frequency of the system was 61.23 Hz. With ADP based VI, the maximum frequency of the system was 61.5 Hz. Although the maximum frequency is higher in ADP based VI than VI, it is still within the ISO 8528-5 standard limits. The settling time for increased load without VI, with VI and with ADP based VI were 12.61 s, 35.16 s and 31.38 s respectively. With VI in the system, the frequency of system returned to nominal frequency slower compared to the system without VI. Similarly, the settling time for decreased load without VI, with VI and with ADP based VI were 11.12 s, 29.19 s and 26.58 s respectively. With VI in the system, the frequency of system returned to nominal frequency slower compared to the system without VI. This is due to the addition of inertia from VI in the system. With ADP based VI, the settling time reduced compared to VI, which proves that the ADP controller improved the dynamics of outer controller of VI and bring the system frequency to nominal frequency faster.

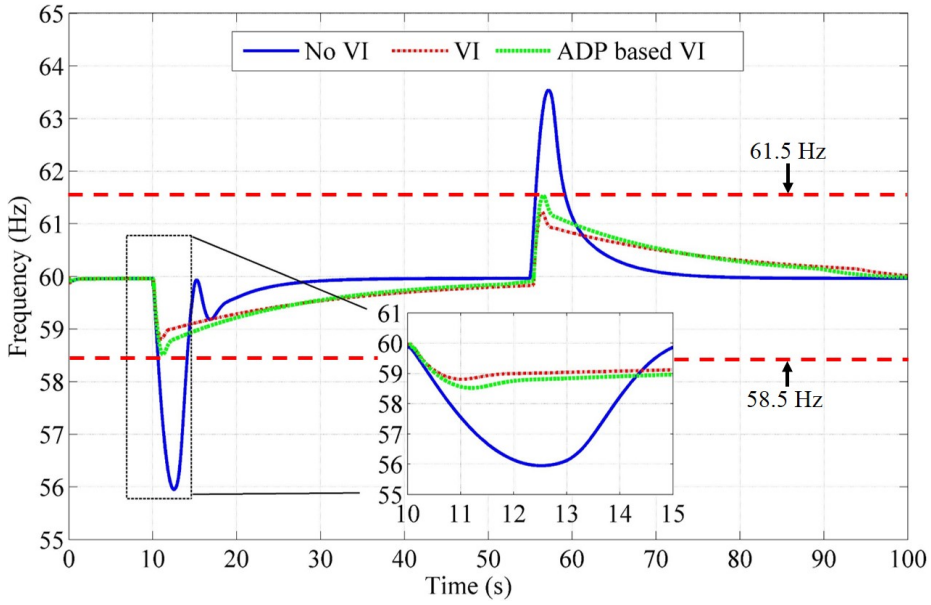

Figure 4.9. Simulation result of system frequency without VI, with VI and with ADP based VI.

Figure 4.10 shows the ROCOF of the system. Without VI the maximum and minimum ROCOF of the system were 2.536 Hz/s and -2.49 Hz/s respectively. With VI, the maximum and minimum ROCOF of the system were 2.1 Hz/s and -1.80 Hz/s. With ADP based VI, the maximum and minimum ROCOF of the system were 2.08 Hz/s and -1.92 Hz/s respectively. The ROCOF of the system was improved with VI and ADP based VI but were not within ISO 8528-5 standard limits. This is because the maximum power deliverable by VI was limited. If the power ratings of inverter were increased or multiple units of VI were connected to provide more inertial power then ROCOF could also be within the standard. This kind of step load change of huge amount do not occur in real life scenario and the improvement in frequency response and ROCOF gives the proof of concept of VI and ADP based VI.

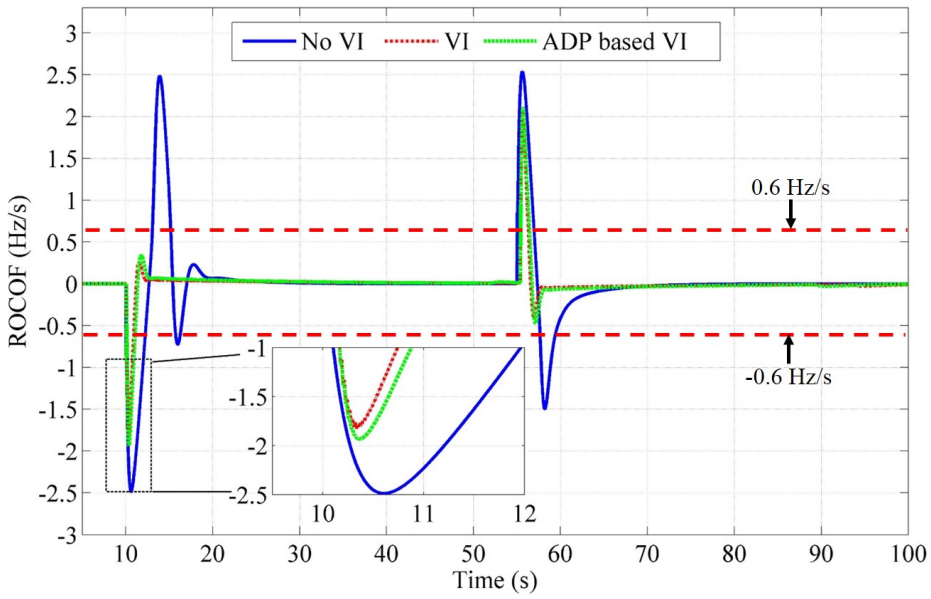

Figure 4.10. Simulation result of ROCOF of the system without VI, with VI and with ADP based VI.

Figure 4.11 shows the total active power exchanged by VI and ADP based VI for case study I. The maximum power delivered by VI during increased load was 2184 W and the maximum power delivered by the ADP based VI was 1979 W. The maximum power delivered by the ADP based VI was 90.61% of the peak power delivered by VI. Similarly, the maximum power absorbed during decreased load by the VI was -2235 W and the maximum power absorbed by the ADP based VI was -2029 W. This shows that the maximum power absorbed by the ADP based VI was 90.78% of the maximum power absorbed by VI. Reduction in maximum power exchanged by the ADP based VI compared to VI can reduce the maximum power rating of power electronics converter of VI.

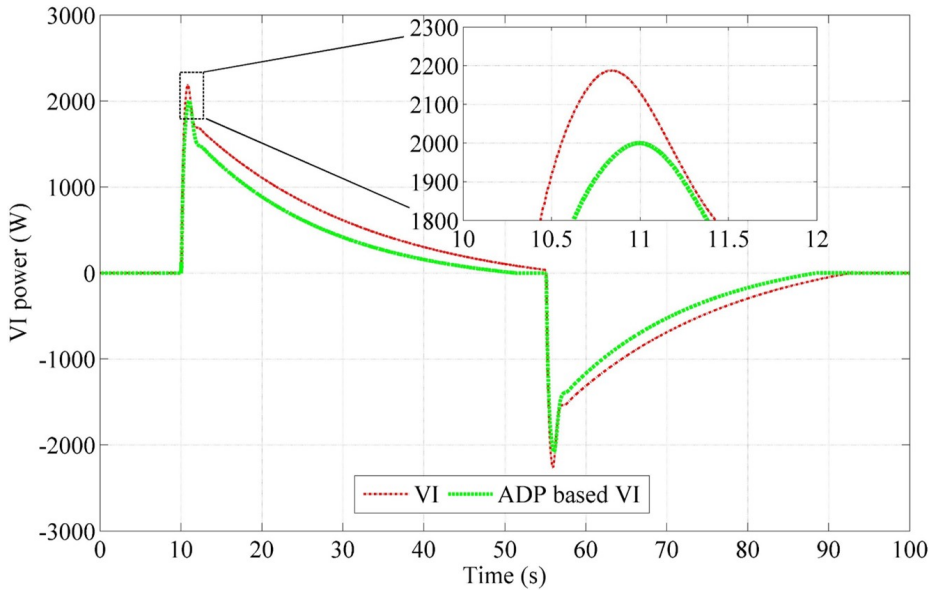

Figure 4.11. Simulation result of active power exchanged by VI and ADP based VI.

Figure 4.12 shows the net energy exchanged by VI and ADP based VI. The net energy exchanged by VI and ADP based VI were 1.6 Wh and 0.9 Wh respectively. 0.7 Wh energy was saved by ADP based VI compared to VI for case study I. The net energy delivered by ADP based VI was 56.25% of net energy delivered by VI.

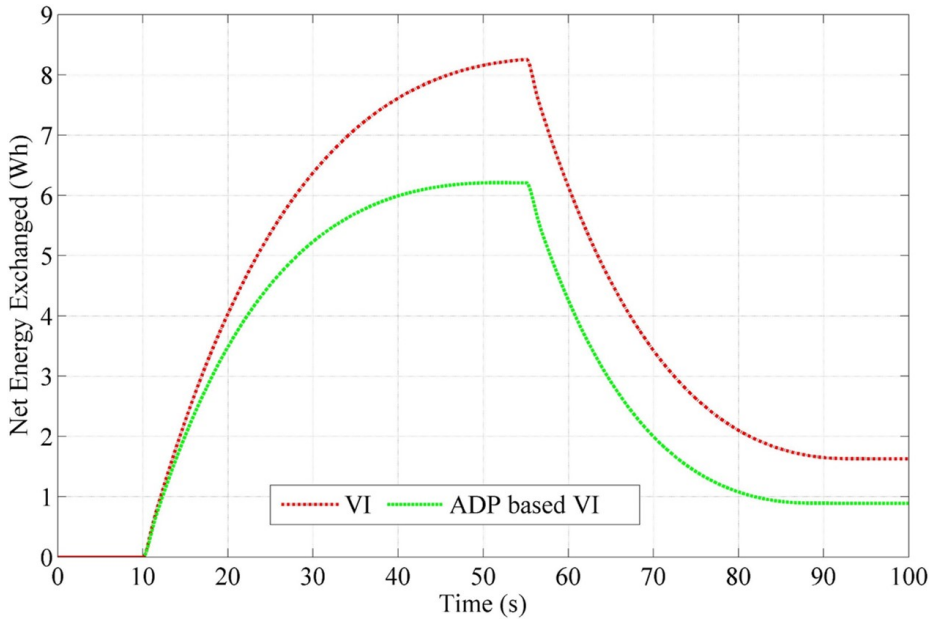

Figure 4.12. Simulation result of net energy exchanged by VI and ADP based VI.

Table 4.2 shows the summary of results without VI, with VI and ADP based VI for case study I.

Table 4.2. Performance comparison of the system without VI, with VI and ADP based VI for case study I

Parameter	No VI	VI	ADP based VI
$\text{Power}_{\text{max}}$ (W)	0	2184	1979
Settling time for load increased (s)	12.61	35.16	31.38
$\text{Power}_{\text{min}}$ (W)	0	-2235	-2029
Settling time for load decreased (s)	11.12 s	29.19 s	26.58 s
Energy delivered (Wh)	0	8.254	6.21
Net energy Exchanged (Wh)	0	1.6	0.9

4.6 Simulation results of case study II

Figure 4.13 shows the frequency response of the system without VI, with VI and with ADP based VI for case study II. The minimum frequency of the system without VI, with VI and with ADP based VI were 58.53 Hz, 59.58 Hz and 59.58 Hz respectively. The maximum frequency of the system without VI, with VI and with ADP based VI were 62.34 Hz, 60.90 Hz and 61.31 Hz respectively. Although the minimum and maximum frequency were lower and higher with ADP based VI than with VI, they are still within the ISO 8528-5 standard limits.

Figure 4.14 shows the ROCOF of the system without VI, with VI and with ADP based VI. The minimum ROCOF of the system without VI, with VI and with ADP based VI were -1.15 Hz/s, -0.42 Hz/s and -0.62 Hz/s respectively. The maximum ROCOF of the system without VI, with VI and with ADP based VI were 0.88 Hz/s, 0.31 Hz/s and 0.48 Hz/s respectively. Although the minimum and maximum ROCOF were lower and higher with ADP based VI than with VI, they were still within the ISO 8528-5 standard limits.

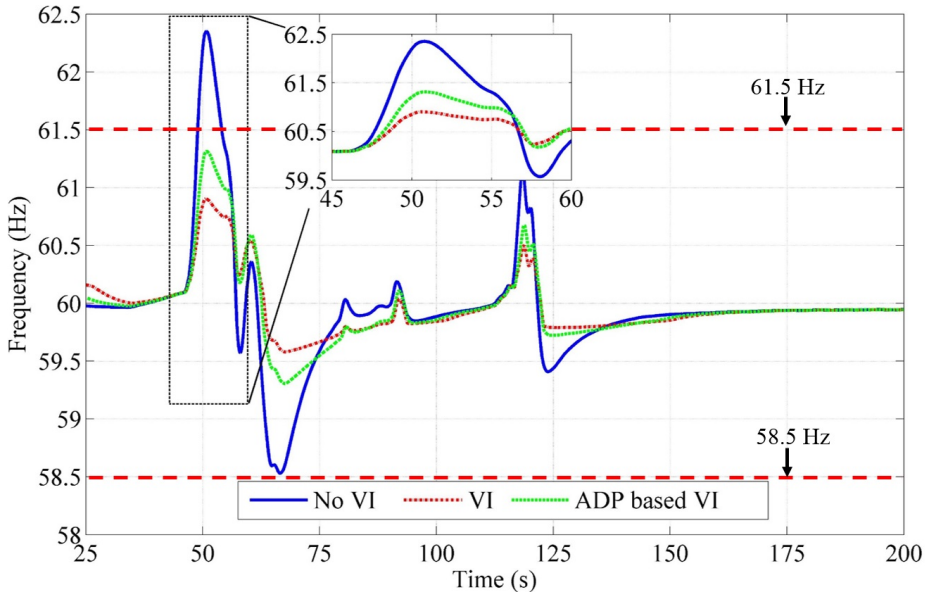

Figure 4.13. Simulation result of frequency of the system.

Figure 4.15 shows the comparison of total active power exchanged by VI and ADP based VI for case study II. The maximum power delivered by the VI and ADP based VI were 542 W and 507 W respectively. The maximum power delivered by ADP based VI was 93.54% of peak power delivered by VI. On the other hand, the peak power absorbed by VI and ADP based VI were -1507 W and -1077 W respectively. The maximum power absorbed by the ADP based VI was 71.46% of VI. This reduction in maximum power delivered and absorbed by the VI can reduce the maximum power rating of power electronics converter of VI.

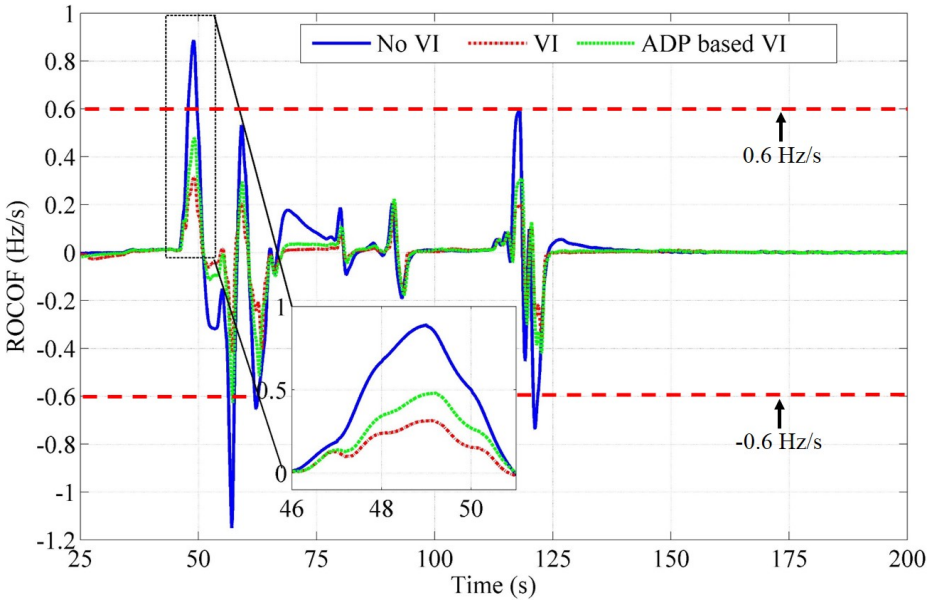

Figure 4.14. Simulation result of ROCOF of the system.

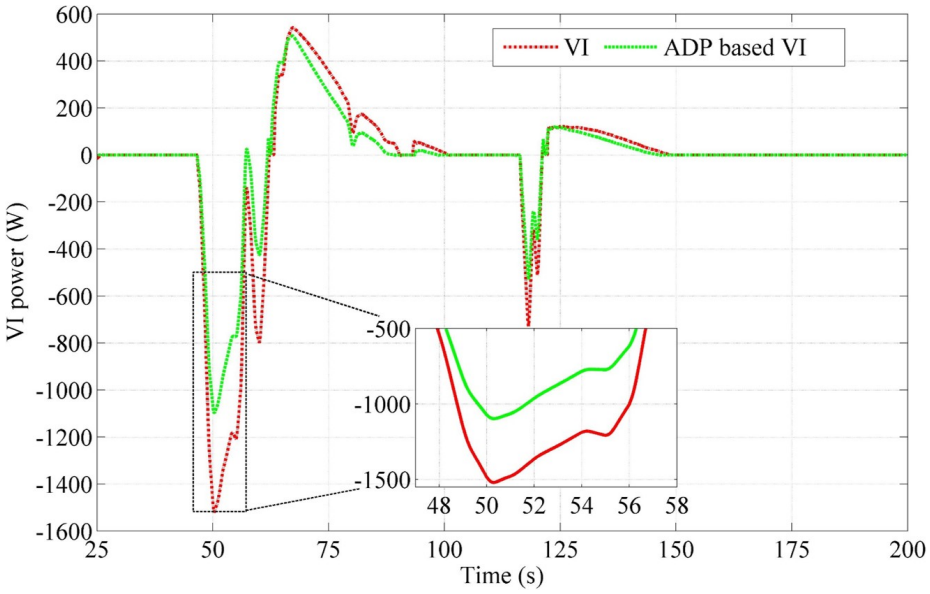

Figure 4.15. Simulation result of active power exchanged by VI and ADP based VI.

Figure 4.16 shows the net energy delivered by the VI and the ADP based VI. The net energy delivered by VI and ADP based VI were 5.05 Wh and 2.33 Wh respectively. For case study II, 2.72 kWh net energy delivered was saved by the ADP based VI compared to the VI. The net energy delivered by the ADP based VI was 46.14% of net

energy exchanged by the VI.

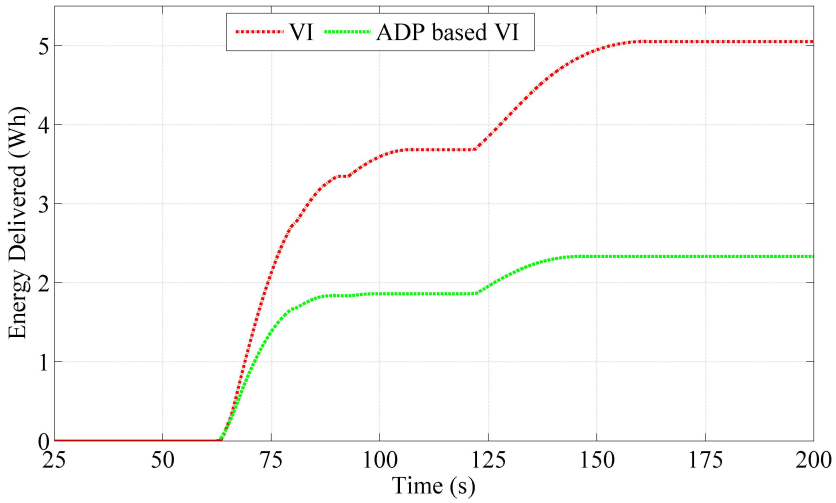

Figure 4.16. Simulation result of net energy delivered by VI and ADP based VI.

Figure 4.17 shows the net energy exchanged by the VI and the ADP based VI. The net energy exchanged by VI and ADP based VI were -1.91 Wh and -0.73 Wh respectively. For case study II, 1.18 kWh net energy exchanged was saved by ADP based VI compared to VI. The net energy exchanged by the ADP based VI was 38.22% of net energy exchanged by the VI.

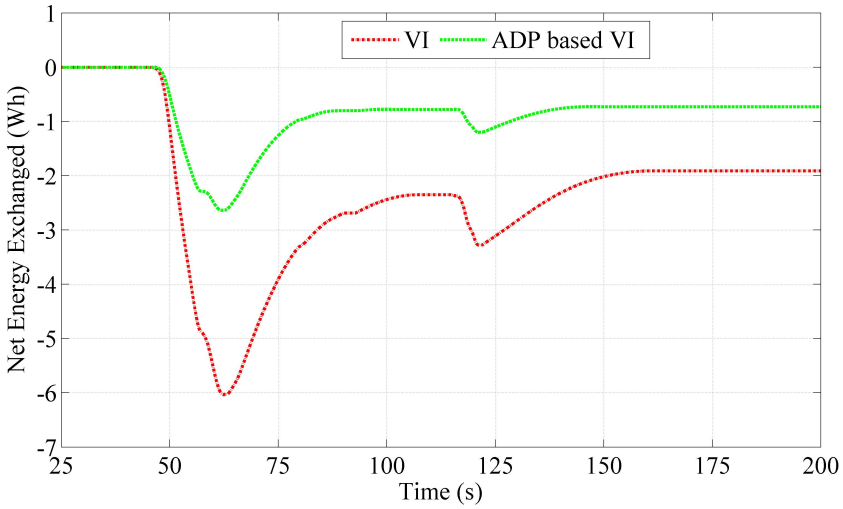

Figure 4.17. Simulation result of net energy exchanged by VI and ADP based VI.

Table 4.3 shows the summary of the results without VI, with VI and with ADP based VI for case study II.

Table 4.3. Performance comparison of the system with VI and ADP based VI for case study II

Parameter	No VI	VI	ADP based VI
$\text{Power}_{\text{min}}$ (W)	0	-1507	-1077
$\text{Power}_{\text{max}}$ (W)	0	542	507
Energy delivered (Wh)	0	5.05	2.33
Net energy exchanged (Wh)	0	-1.91	-0.73

4.6.1 Effect on lifetime of the battery for case study II

The total energy (effective Ah) delivered by VI for case study II was

$$Total\ effective\ Ah\ energy\ delivered\ by\ VI = \frac{5.05\ Wh}{400\ V} = 0.0126\ Ah \tag{4.2}$$

Similarly, the total energy (effective Ah) delivered by ADP based VI for case study II was

$$Total\ effective\ Ah\ energy\ delivered\ by\ ADP\ based\ VI = \frac{2.33\ Wh}{400\ V} = 0.0058\ Ah \tag{4.3}$$

Considering the total effective lifetime of battery as 48750 Ah, the total number of battery discharge cycles for VI for case study II can be calculated as follows

$$Total\ no.\ of\ battery\ discharge\ cycles\ possible\ for\ VI = \frac{48750\ Ah}{0.0126\ Ah} \tag{4.4}$$

$$= 3,869,047.619 cycles \approx 3,869,000\ cycles \tag{4.5}$$

Similarly, the total number of battery discharge cycles possible for ADP based VI can be obtained as follows

$$Total\ no.\ of\ battery\ discharge\ cycles\ possible\ for\ ADP\ based\ VI = \frac{48750\,Ah}{0.0058\,Ah} \quad (4.6)$$

$$= 8,405,172.41 cycles \approx 8,405,000\ cycles \quad (4.7)$$

Therefore, the approximate total number of battery discharge cycles possible for VI and ADP based VI are 3,869,000 cycles and 8,405,000 cycles respectively. So, using ADP based VI, the total number of discharge cycles possible is 2.17 times the total discharge cycles possible with VI. The ADP base VI enables the use of the same size of battery for a longer time duration compared to VI. The total discharge cycles may look like a huge quantity but the analysis is just based upon the 200 s snapshot of real output power from PV systems. In a real system, the number of charging and discharging of battery for VI can be high.

CHAPTER 5 CONCLUSIONS

Chapter 5 presents the summary, conclusions and future work of this work.

5.1 Summary

Photovoltiac diesel generator microgrid system can be an economical and technically sound way to provide electricity to the people in remote area where the extension of the national grid is difficult. But the PV systems have less inertial response in comparison to synchronous generators. Due to this, dynamic frequency stability issues might occur due to continuous changing load or indeterminacy nature of PV systems. So dynamic frequency controller needs to be added in the system to make it stable. Virtual inertia can be emulated in the system from ESS to improve the dynamic frequency stability. Virtual inertia can be defined as the combination of energy storage system, power electronics converter and proper control algorithm. Dynamic frequency stability of a power system is the ability of the power system to maintain synchronism when there is small but continuous changes in the generation like output power from photovoltaic system or changes in load. Changes in output power from photovoltaic systems for load may lead to higher deviation of frequency from nominal frequency.

According to simulation results, only 45% of the total capacity of photovoltaic-hydro microgrids systems with system inertia of 5 s can be supplied by photovoltaic systems while keeping the frequency of the system within normal operating range of ±2% of nominal frequency. This shows that the maximum penetration level of photovoltaic systems in the microgrid is limited due to frequency stability issues. Virtual inertia has been implemented in the system to improve the dynamic frequency stability

using different control architectures. The hardware prototype of proportional derivative controller based virtual implemented in a microgrid with a real diesel generator has not been found. Addition of virtual inertia brings the system frequency to nominal frequency slower. As a result, relatively more energy is exchanged between the ESS and the microgrid system. The literature also lacks improvement in the dynamics of the controller of VI using an ADP based online controller that brings the system frequency to nominal frequency faster.

Dynamic frequency controller is required to allow higher penetration of photovoltaic system. The dynamic frequency controller also needs to be adaptive to stabilize the frequency of the system faster. The main motivation of this research is to improve dynamic frequency stability of the photovoltaic diesel generator microgrid system to allow higher penetration of photovoltaic system. The main objectives of this research was to develop a hardware prototype of virtual inertia and test it in a microgrid with a real generator. Besides, the other objective was to make the controller of virtual inertia adaptive and learn online. The main tasks of this research were to 1) develop the hardware prototype of current controlled voltage source inverter, 2) implement the concept of virtual inertia in developed inverter to improve dynamic frequency stability of a microgrid with a real generator, and 3) develop simulation model of an online learning control using adaptive dynamic programming for virtual inertia.

The z-domain current controller was modeled for a three phase current controlled voltage source inverter in PSIM software. A hardware prototype of 1 kW current controlled voltage source inverter was developed. A microgrid with a 13 kW diesel generator, three phase resistive load and virtual inertia was developed. The controller

gains of a virtual inertia were tuned based upon the frequency response of the 13 kW diesel generator. The virtual inertia injected the active power during the transient while step change in load to improve the dynamic frequency stability of the system. Increasing the size of the inverter can further improve the frequency response of the system.

An online learning controller was implemented in virtual inertia using adaptive dynamic programming in MATLAB/Simulink. An adaptive dynamic programming controller was added as supplementary controller to proportional derivative controller of existing virtual inertia. The neural network structure of the adaptive dynamic programming controller was trained to improve the dynamics of controller of virtual inertia so that the frequency of the system was stabilized faster. Due to the faster dynamics, the net energy delivered by the virtual inertia with the proposed controller was 46.14% of the net energy delivered by the existing virtual inertia. Besides, considering the effective lifetime of the lead acid battery, the total number of battery discharge cycles possible with ADP based VI was 2.17 times the total number of battery discharge cycles possible with VI.

5.2 Conclusions

The main contribution of this thesis is the development of a hardware prototype of a proportional derivative based virtual inertia and its implementation in a microgrid with a real generator and a load. The frequency response of the microgrid was improved by virtual inertia and the proof of concept of virtual inertia was verified experimentally. The frequency response would improve even more if the size of the inverter used for virtual inertia is of higher power rating. But this can increase the cost of power electronics

converter. On the other hand, an online learning controller using adaptive dynamic programming was implemented to improve the dynamics of the virtual inertia. Due to faster dynamics of the controller, the frequency of the system stabilized faster. Moreover, the net energy delivered decrease and the net energy delivered by the ADP based VI was 46.14% of the net energy delivered by the existing VI. Considering the total effective lifetime of a lead acid battery, the total number of discharge cycles possible with ADP based VI was 2.17 times the total number of discharge cycles possible with VI.

5.3 Future Work

Future work should include the addition of PV systems into the microgrid system in experiment and analyze the frequency response of the system with and without virtual inertia. A single PCB of inverter with the virtual inertia algorithm needs to be developed. A hardware prototype of ADP based virtual inertia also needs to be developed using high performance microcontroller like FPGA. The size of the energy storage required for virtual inertia emulation needs to be calculated. Cost analysis needs to be done to compare the cost of implementation of both virtual inertia and ADP based virtual inertia.

REFERENCES

[1] International Energy Agency. (2015). Modern Energy for All. Accessed: September 14, 2016, [Online]. Available: http://www.worldenergyoutlook.org/resources/energydevelopment/.

[2] Navigant Research. (2012). Remote Microgrids. Accessed: September 14, 2016, [Online]. Available: https://www.navigantresearch.com/webinar/remote-microgrids-2.

[3] International Energy Agency, "2014 Snapshot of Global PV Market," Photovoltaic Power Systems Programme, Tech. Rep., 2015.

[4] National Energy Technology Laboratory, "Frequency Instability Problems in North American Interconnections," Department of Energy, Tech. Rep., 2011.

[5] A. Gururng, D. Galipeau, R. Tonkoski, and I. Tamrakar, "Feasibility Study of Photovoltaic-hydropower microgrids," in *5th International Conference on Power and Energy Systems(ICPS)*, 2014.

[6] *Reciprocating internal combustion engine driven alternating current generating sets- Part 5: Generating sets*, ISO, 2005.

[7] C. Rahmann and A. Castillo, "Fast Frequency Response Capability of Photovoltaic Power Plants: The Necessity of New Grid Requirements and Definitions [On the electrodynamics of moving bodies]," *Energies*, vol. 7, no. 10, pp. 6306–6322, 2014.

[8] X. Wang, M. Yue, and E. Muljadi, "PV generation enhancement with a virtual inertia emulator to provide inertial response to the grid," in *2014 IEEE Energy Conversion Congress and Exposition (ECCE)*, 2014, pp. 17–23.

[9] M. P. N. van Wesenbeeck, S. W. H. de Haan, P. Varela, and K. Visscher, "Grid tied converter with virtual kinetic storage," in *PowerTech, 2009 IEEE Bucharest*, 2009, pp. 1–7.

[10] Q. C. Zhong and T. Hornik, "Synchronverters: Grid-Friendly Inverters That Mimic Synchronous Generators," in *Control of Power Inverters in Renewable Energy and Smart Grid Integration*. Wiley-IEEE Press, 2012, pp. 277–296, ISBN: 9781118481806.

[11] M. A. Torres, L. A. C. Lopes, L. A. Moran, and J. R. Espinoza, "Self-Tuning Virtual Synchronous Machine: A Control Strategy forEnergy Storage Systems to Support Dynamic Frequency Control," *IEEE Transactions on Energy Conversion*, vol. 29, no. 4, pp. 833–840, 2014, ISSN: 0885-8969.

[12] K. Sakimoto, Y. Miura, and T. Ise, "Stabilization of a power system with a distributed generator by a Virtual Synchronous Generator function," in *Power Electronics and ECCE Asia (ICPE ECCE), 2011 IEEE 8th International Conference on*, 2011, pp. 1498–1505.

[13] B. B. Johnson, M. Sinha, N. G. Ainsworth, F. Dörfler, and S. V. Dhople, "Synthesizing Virtual Oscillators toControl Islanded Inverters," *IEEE Transactions on Power Electronics*, vol. 31, no. 8, pp. 6002–6015, 2016.

[14] A. Ellis, D. Schoenwald, J. Hawkins, S. Willard, and B. Arellano, "PV output smoothing with energy storage," in *Photovoltaic Specialists Conference (PVSC)*, 2012, pp. 001 523–001 528.

[15] U. Tamrakar, D. Galipeau, R. Tonkoski, and I. Tamrakar, "Improving transient stability of photovoltaic-hydro microgrids using virtual synchronous machines," in *PowerTech, 2015 IEEE Eindhoven*, 2015, pp. 1–6.

[16] W. Guo, F. Liu, J. Si, and S. Mei, "Incorporating approximate dynamic programming-based parameter tuning into PD-type virtual inertia control of DFIGs," in *Neural Networks (IJCNN), The 2013 International Joint Conference on*, 2013, pp. 1–8.

[17] R. E. Bellman, *Dynamic Programming*. Princeton University Press, 1957.

[18] A. D. Paquette, M. J. Reno, R. G. Harley, and D. M. Divan, "Sharing Transient Loads : Causes of Unequal Transient Load Sharing in Islanded Microgrid Operation," *IEEE Industry Applications Magazine*, vol. 20, no. 2, pp. 23–34, 2014, ISSN: 1077-2618.

[19] S. Chalise and R. Tonkoski, "Day ahead schedule of remote microgrids with renewable energy sources considering battery lifetime," in *Industry Applications (INDUSCON), 2014 11th IEEE/IAS International Conference on*, 2014, pp. 1–5.

[20] T. Basso, *IEEE 1547 and 2030 Standards for Distributed Energy Resources Interconnection and Interoperability with the Electricity Grid*, IEEE, 2014.

[21] R. A. Messenger and J. Ventre, *Photovoltaic System Engineering, 3rd Edition*. 2010.

[22] Renesola. (2013). ReneSola 255 Watt Poly Solar Panel. Accessed: October 7, 2016, [Online]. Available: http://www.savanasolar.com/branded-solar-product/renesola/renesola-255-watt-poly-solar-panel.html.

[23] A. E. Tutorials. (2016). Solar Cell I-V Characteristic. Accessed: October 7, 2016, [Online]. Available: http://www.alternative-energy-tutorials.com/energy-articles/solar-cell-i-v-characteristic.html.

[24] V. Ou. (2016). How Does a Generator Create Electricity? Linkedin.com, Ed. [Online; posted 18 Feburary, 2016], [Online]. Available: {https://www.linkedin.com/pulse/how-does-generator-create-electricity-adam-ou}.

[25] P. Kundur, "Control of Active Power and Reactive Power," in *Power System Stability and Control*, N. J. Balu and M. G. Lauby, Eds., New Delhi: Tata McGraw Hill Education Private Limited, 2010, ch. 11, pp. 581–691.

[26] A. Akhil, G. Huff, A. B. Currier, B. C. Kaun, D. M. Rastler, S. B. Chen, A. L. Cotter, D. T. Bradshar, and W. D. Gauntlett, "DOE/EPRI Electricity Storage Handbook in Collaboration with NRECA," Sandia National Laboratories, 2015.

[27] D. R. Conover, A. J. Crawford, J. Fuller, S. N. Gourisetti, V. Viswanathan, S. R. Ferreira, D. A. Schoenwald, and D. M. Rosewater, "Protocol for Uniformly Measuring and Expressing the Performance of Energy Storage Systems," Pacific Northwest National Laboratories and Sandia National Laboratories, 2016.

[28] J. Schiffer, D. U. Sauer, H. Bindner, T. Cronin, P. Lundsager, and R. Kaiser, "Model prediction for ranking lead-acid batteries according to expected lifetime in renewable energy systems and autonomous power-supply systems," in *Journal of Power Sources*, 2007, pp. 66–78.

[29] D. P. Jenkins, J. Fletcher, and D. Kane, "Lifetime prediction and sizing of lead-acid batteries for microgeneration storage applications," in *IET Renewable Power Generations*, 2008, pp. 191–200.

[30] "Balancing and frequency control," North American Electric Reliability Corporation, 2011.

[31] N. Mohan, T. M. Undeland, and W. P. Robbins, *Power Electronics: Converters, Applications and Design*. Wiley, 2010.

[32] V. Karapanos, S. de Haan, and K. Zwetsloot, "Real time simulation of a power system with VSG hardware in the loop," in *IECON 2011 - 37th Annual Conference on IEEE Industrial Electronics Society*, 2011, pp. 3748–3754.

[33] D. Shrestha, U. Tamrakar, N. Malla, Z. Ni, and R. Tonkoski, "Reduction of energy consumption of virtual synchronous machine using supplementary adaptive dynamic programming," in *2016 IEEE International Conference on Electro Information Technology (EIT)*, 2016, pp. 0690–0694.

[34] H. G. Zhang, X. Zhang, Y. H. Luo, and J. Yang., "An Overview of Research on Adaptive Dynamic Programming," *Science Direct*, vol. 39, no. 4, 2013.

[35] T. M. Mitchell, *Machine Learning*. McGraw-Hill, 1997.

[36] J. Si and Y.-T. Wang, "Online learning control by association and reinforcement," *IEEE Transactions on Neural Networks*, vol. 12, no. 2, pp. 264–276, 2001, ISSN: 1045-9227.

[37] U. Tamrakar, "Improvement of transient stability of photovoltaic-hydro microgrids using virtual synchronous machines," Master's thesis, South Dakota State University, Brookings, SD, USA, 2015.

[38] K. Ogata, *Discrete-Time Control Systems*. PHI, 2013.

[39] Texas Instruments, *LM2907/LM2917 Frequency to Voltage Converter*. Texas Instruments, 2013.

[40] Texas Instruments, *C28X IQmath Library*. Texas Instruments, 2010.

[41] Texas Instruments, *TMS320F2803X Piccolo Microcontrollers*. Texas Instruments, 2016.

[42] N. Malla, D. Shrestha, Z. Ni, and R. Tonkoski, "Supplementary control for virtual synchronous machine based on adaptive dynamic programming," 2016, pp. 1998–2005.